Forschungszentrum Karlsruhe
Technik und Umwelt

Wissenschaftliche Berichte
FZKA 6083

Investigation of the Phebus FPT0 bundle degradation with SCDAP/RELAP5

S.-O. Smit, W. Sengpiel, W. Hering

Institut für Reaktorsicherheit
Projekt Nukleare Sicherheitsforschung

April 1998

Forschungszentrum Karlsruhe
Technik und Umwelt

Wissenschaftliche Berichte

FZKA 6083

Investigation of the Phebus FPT0 bundle degradation with SCDAP/RELAP5

S.-O. Smit, W. Sengpiel, W. Hering

Institut für Reaktorsicherheit
Projekt Nukleare Sicherheitsforschung

Forschungszentrum Karlsruhe GmbH, Karlsruhe
1998

Als Manuskript gedruckt

Forschungszentrum Karlsruhe GmbH
Postfach 3640, 76021 Karlsruhe

Mitglied der Hermann von Helmholtz-Gemeinschaft
Deutscher Forschungszentren (HGF)

ISSN 0947-8620

Abstract

In the Institute of Reactor Safety (IRS) at the Forschungszentrum Karlsruhe (FZK), light water reactor (LWR) studies are performed in the frame of the Nuclear Safety Reseach Project to investigate the in-vessel behaviour under severe accident conditions. The internationally acknowledged computer code SCDAP/RELAP5 is used for whole plant analyses including core degradation sequences. In order to validate the code, severe core damage experiments such as CORA and Phebus FP have been selected for test analyses.

The in-pile experiment Phebus FPT0 provides an excellent data base reflecting the course and the consequences of a severe core melt accident starting from the core uncovery up to bundle degradation and molten pool formation.

In the IRS post-test calculations of the Phebus FPT0 have been performed with SCDAP/RELAP5. A detailed parameter study has shown that some models used in the code still have to be improved and that some parametric models need to be substituted by more physical models. In the context of this parameter study, the heat transfer through the Phebus FPT0 shroud has been identified to be one of the most influencial physical processes on the course of bundle degradation. Especially the gap behaviour and the heat transport through the gaps of the FPT0 shroud have shown to be insufficiently modeled by the original code version. Therefore, the shroud heat transfer model has been improved to consider dynamic gap closure by thermal expansion of the shroud materials and to take into account radiation heat transfer through open gaps.

In this report, the results of the parameter study for FPT0 obtained with the original code are compared to the results of a reference calculation which includes the improved shroud model. It is shown that SCDAP/RELAP5 is now able to calculate the heat losses through a shroud containing gas-filled gaps like that of Phebus FPT0 quite accurrately. Thus, SCDAP/RELAP5 now can also be used more successfully for test analyses of experiments like Phebus FPT1 and FPT2, and of the QUENCH test series.

Kurzfassung

Untersuchung der Phebus FPT0 Bündelzerstörung mit SCDAP/RELAP5

Im Institut für Reaktorsicherheit (IRS) am Forschungszentrum Karlsruhe (FZK) werden Leichtwasserreaktor (LWR)-Studien im Rahmen des Projektes „Nukleare Sicherheitsforschung" durchgeführt, um das Unfallverhalten im Reaktordruckbehälter während eines schweren Störfalls zu untersuchen. Der international anerkannte Computercode SCDAP/RELAP5 wird zur Analyse von ganzen Kraftwerken einschließlich der Kernzerstörungsphasen eingesetzt. Um diesen Code zu validieren, sind Experimente zur schweren Kernzerstörung wie CORA und Phebus FP für Testauswertungen ausgewählt worden.

Das In-Pile-Experiment Phebus FPT0 liefert hier eine exzellente Datenbasis bezüglich des Ablaufes und der Konsequenzen eines schweren Kernschmelzunfalls angefangen von der Kernfreilegung bis zur Bündelzerstörung und der Bildung eines Schmelzepools.

Im IRS sind Nachrechnungen von Phebus FPT0 mit SCDAP/RELAP5 durchgeführt worden. Eine detailierte Parameterstudie hat gezeigt, daß einige Modelle des Codes noch verbessert werden müssen und einige parametrische Modelle durch physikalischere Modelle zu ersetzen sind. Im Zusammenhang mit dieser Parameterstudie wurde der Wärmetransport durch die Ummantelung des FPT0 Bündels als einer der physikalischen Prozesse identifiziert, der den Verlauf der Bündelzerstörung stark beeinflußt. Insbesondere das Verhalten der Spalte und der Wärmetransport über die Spalte der Ummantelung haben sich als vom Originalcode nicht zufriedenstellend modelliert herausgestellt. Daher ist das Wärmetransportmodell für die Ummantelung insofern verbessert worden, daß nun auch das dynamische Schließen der Spalte aufgrund der thermischen Ausdehnung der Materialien der Ummantelung und der Strahlungswärmetransport über die offenen Spalte berücksichtigt wird.

In diesem Bericht werden die Ergebnisse der Parameterstudie für FPT0, die mit dem Originalcode erzielt wurden, mit denen einer Referenzrechnung mit dem verbesserten Wärmetransportmodell für die Ummantelung verglichen. Dabei wird gezeigt, daß SCDAP/RELAP5 nun in der Lage ist, die Wärmeverluste durch eine Ummantelung mit gasgefüllten Spalten, wie diejenigen in Phebus FPT0, recht gut zu rechnen. Daher kann SCDAP/RELAP5 auch für Auswertungen von Experimenten wie Phebus FPT1 und FPT2 sowie für die QUENCH-Testserie noch erfolgreicher eingesetzt werden.

1 INTRODUCTION 1

2 THE PHEBUS FPT0 EXPERIMENT 2

2.1 DESCRIPTION OF THE FPT0 BUNDLE 2
2.1.1 Geometry 2
2.1.2 Axial and radial power profiles 5
2.1.3 Time dependent conditions 5
2.1.4 Location of the bundle thermocouples 7
2.2 BUNDLE BEHAVIOUR DURING THE EXPERIMENT 8
2.2.1 Pre-transient Phase 9
2.2.2 Heat-up Phase 9

3 SCDAP/RELAP5 CAPABILITIES ESSENTIAL FOR PHEBUS FP 19

3.1 MODELING OF IN-VESSEL PHENOMENA 19
3.1.1 Core heat-up 19
3.1.1.1 Power source and distribution 19
3.1.1.2 Radial heat losses 19
3.1.1.3 Convective heat losses 20
3.1.2 Zircaloy cladding rupture 20
3.1.3 Oxidation 21
3.1.4 UO_2 Dissolution 21
3.1.5 Oxide shell failure 22
3.1.6 Melt release, relocation, and blockage formation 22
3.1.7 Behavior of a molten pool 22
3.1.7.1 Molten pool formation 22
3.1.7.2 Pool spreading 23
3.1.7.3 Crust failure 23
3.2 CODE IMPROVEMENTS 23
3.2.1 Restart capability 23
3.2.2 Improvements for 2-D heat conduction heatc2 24
3.2.3 Phebus specific shroud model 24
3.3 TEST SPECIFIC PROPERTIES FOR FPT0 25

4 COMPARISON OF EXPERIMENTAL AND CALCULATIONAL RESULTS 28

4.1 GOALS OF THE STUDY 28
4.2 INVESTIGATED PARAMETERS OF THE SENSITIVITY STUDY 29
4.3 EXPERIMENTAL PHASES OF FPT0 35
4.3.1 Pre-transient (calibration) phase 35
4.3.1.1 Starting conditions at 5000 s 35
4.3.1.2 Cladding ballooning and rupture 36
4.3.2 Transient heat-up phase 38
4.3.2.1 Oxidation 38
4.3.2.2 Melt relocation 39
4.3.2.3 Molten pool formation 40
4.3.2.4 Control rod behaviour 41
4.4 FZK/IRS CALCULATIONAL ROUTE 41

5 SUMMARY AND CONCLUSION 64

6 REFERENCES 66

7 APPENDIX 68
7.1 FPT0 TEST CONDUCT AND CHARACTERISTIC EVENTS 68
7.2 A NEW SHROUD GAP MODEL FOR SCDAP/RELAP5 70
7.2.1 Theory 70
7.2.2 Symbols 74

List of Figures

FIGURE 2.1 CROSS SECTION OF THE PHEBUS FPT0 BUNDLE [14] 2
FIGURE 2.2 CROSS SECTION OF THE SHROUD, THE GIVEN RADIAL POSITIONS ARE THE OUTER AND INNER THERMOCOUPLE POSITIONS, RESPECTIVELY (A); CROSS SECTION OF A STIFFENER, MEASUREMENTS IN MM (B) [14] 3
FIGURE 2.3 AXIAL POWER PROFILE IN TERMS OF NORMALIZED POWER FACTORS [14] 5
FIGURE 2.4 NORMALIZED RADIAL POWER FACTORS WITH INTACT CONTROL ROD (LEFT) AND AFTER LOSS OF ABSORBER MATERIAL (RIGHT) [14] 5
FIGURE 2.5 PHEBUS FPT0 BUNDLE POWER AND INLET STEAM FLOW RATE VS. TIME 6
FIGURE 2.6 SCHEME OF THE RADIAL AND AXIAL POSITIONS OF THERMOCOUPLES FOR TEMPERATURE MEASUREMENTS IN THE BUNDLE AND IN THE SHROUD [2] 7
FIGURE 2.7 PHEBUS FPT0 TEST SCENARIO WITH MEASURED FUEL ROD TEMPERATURES AT 700 MM AND SIGNIFICANT EVENTS OF THE BUNDLE DEGRADATION [2] 11
FIGURE 2.8 AXIAL TEMPERATURE DISTRIBUTIONS MEASURED DURING THE CALIBRATION PHASE AT 6485 S AND 10140 S 12
FIGURE 2.9 EVOLUTION OF FUEL ROD TEMPERATURES DURING THE FPT0 12
FIGURE 2.10 EVOLUTION OF AXIAL TEMPERATURE PROFILES DURING THE OXIDATION PHASE 13
FIGURE 2.11 HYDROGEN GENERATION RATE AND CUMULATIVE HYDROGEN MASS FOR PHEBUS FPT0 [11] 13
FIGURE 2.12 FUEL ROD TEMPERATURES MEASURED DURING THE BUNDLE DEGRADATION PHASE INDICATING MELT RELOCATION AND BUNDLE COLLAPSE 14
FIGURE 2.13 SHROUD TEMPERATURES MEASURED DURING THE BUNDLE DEGRADATION PHASE INDICATING POOL FORMATION 15
FIGURE 2.14 EVOLUTION OF AXIAL TEMPERATURE PROFILES IN THE SHROUD INDICATING STRONG HEAT-UP IN THE LOWER BUNDLE REGION DURING THE POOL FORMATION PHASE 15
FIGURE 2.15 SCHEME OF EVOLUTION OF THE AXIAL TEMPERATURE PROFILES AS MEASURED IN THE BUNDLE 16
FIGURE 2.16 FINAL BUNDLE STATE WITH MASS DISTRIBUTIONS DEDUCED FROM RADIOGRAPHY AND TOMOGRAPHY [17] 17
FIGURE 2.17 FINAL AXIAL DISTRIBUTION OF INTACT UO_2 18
FIGURE 3.1 AXIAL AND RADIAL DISCRETIZATION OF THE PHEBUS TEST SECTION INCLUDING THREE PARALLEL CHANNELS WITH CROSS FLOW JUNCTIONS AND A WATER CHANNEL AROUND THE SHROUD 26
FIGURE 3.2 SIMPLIFIED FAST RUNNING SCDAP/RELAP5 MODEL OF THE PHEBUS TEST SECTION .. 27
FIGURE 4.1 FUEL ROD TEMPERATURES CALCULATED AT DIFFERENT ELEVATIONS COMPARED WITH CORRESPONDING EXPERIMENTAL DATA 43
FIGURE 4.2 SHROUD TEMPERATURES CALCULATED AT DIFFERENT ELEVATIONS COMPARED WITH THE CORRESPONDING EXPERIMENTAL DATA AT THE INNER (0.4M TO 0.8 M) AND OUTER (0.3 M) SHROUD MEASURING POSITIONS 44
FIGURE 4.3 COMPARISON OF MEASURED AND CALCULATED FUEL ROD TEMPERATURES IN THE CALIBRATION PHASE OF THE EXPERIMENT UP TO 10000 S 45
FIGURE 4.4 AXIAL TEMPERATURE PROFILES IN THE BUNDLE AT 6485 S AND 10140 S FOR CASES (1) TO (11) (4.4A) AND CASES (12) TO (15) (4.4B) 46
FIGURE 4.5 COMPARISON OF MEASURED AND CALCULATED SHROUD TEMPERATURES IN THE CALIBRATION PHASE UP TO 10000 S 47
FIGURE 4.6 CHANGE OF CLADDING RADII CALCULATED IN THE BUNDLE MID-PLANE UP TO CLADDING FAILURE BY OVERSTRAIN 48

FIGURE 4.7 AXIAL PROFILES OF CLADDING DEFORMATIONS CALCULATED AT THE END OF THE CALIBRATION PHASE 48
FIGURE 4.8 COMPARISON OF MEASURED AND CALCULATED FUEL ROD TEMPERATURES IN THE TRANSIENT HEAT-UP PHASE 49
FIGURE 4.9 COMPARISON OF MEASURED AND CALCULATED AXIAL TEMPERATURE PROFILES OF THE FUEL RODS IN THE HEAT-UP PHASE (EXPERIMENTAL DATA ARE EXTENDED BY GUIDE TUBE TEMPERATURES) 50
FIGURE 4.10 COMPARISON OF MEASURED AND CALCULATED SHROUD TEMPERATURES IN THE TRANSIENT HEAT-UP PHASE 52
FIGURE 4.11 HYDROGEN PRODUCTION RATE (A) AND CUMULATIVE HYDROGEN MASS GENERATED BY ZIRCALOY OXIDATION (B) 53
FIGURE 4.12 FRACTION OF THE ZIRCALOY OXIDIZED IN THE COURSE OF THE EXPERIMENT (A) AND AXIAL PROFILES OF THE ZIRCALOY OXIDATION STATUS IN THE BUNDLE AT 15000S CALCULATED FOR THE CASE (13) 54
FIGURE 4.13 EVOLUTION OF FUEL ROD DEGRADATION PROCESS IN TERMS OF MASSES OF LIQUEFIED AND REMOVED UO2 AS THE RESULT OF ZIRCALOY-UO2 CHEMICAL INTERACTION (A) AND IN TERMS OF LIQUID ZIRCALOY MASSES (B) 55
FIGURE 4.14 CALCULATED BEGIN OF MOLTEN POOL FORMATION IN TERMS OF THE EVOLUTION OF THE EQUIVALENT MOLTEN POOL RADIUS (RADIUS OF AN EQUIVALENT HEMISPHERE CONTAINING THE MELT MASS) 56
FIGURE 4.15 EVOLUTION OF THE ABSORBER ROD DEGRADATION IN TERMS OF THE RESIDUAL (NOT YET REMOVED) AG-IN-CD MASS 57
FIGURE 4.16 EVOLUTION OF THE AXIAL FUEL ROD TEMPERATURES VS. TIME FOR THE EXPERIMENT (A) AND FOR CASE (13) (B) 58
FIGURE 4.17 EVOLUTION OF RADIAL TEMPERATURE DISTRIBUTION ACROSS THE FPT0 BUNDLE AND SHROUD FOR CASE (13) 60
FIGURE 4.18 SEQUENCE OF BUNDLE DEGRADATION EVENTS AS MEASURED COMPARED WITH THE CORRESPONDING EVENTS CALCULATED FOR CASE (13) 63
FIGURE 7.1 MODELING OF A SHROUD CONSISTING OF TWO GAPS AND NODALIZATION POINTS USED IN SCDAP/RELAP5 73
FIGURE 7.2 COMPARISON OF REALITY AND MODEL OF A SHROUD GAP 73

List of Tables

TABLE 2.1 GEOMETRICAL DATA AND MATERIALS OF PHEBUS FPT0 BUNDLE COMPONENTS [14] 4
TABLE 2.2 BUNDLE POWER AND STEAM FLOW RATE AT BUNDLE INLET 6
TABLE 2.3 OVERVIEW OF FPT0 TEST CONDUCT AND KEY-EVENTS 8
TABLE 3.1 SCDAP VIEWFACTORS (A) AND PATH LENGTHS (B) USED IN PHEBUS FPT0 CALCULATIONS 20
TABLE 4.1: AXIAL POWER PROFILE USED IN THE PHEBUS FPT0 CALCULATIONS 30
TABLE 4.2 SCDAP/RELAP5 INPUT DATA FOR THE STANDARD THREE-CHANNEL AND TWO-CHANNEL MODELS 31
TABLE 4.3 MODEL AND PARAMETER VARIATIONS FOR THE FPT0 SENSITIVITY STUDY WITH SCDAP/RELAP5 MOD.3.1 REL.D 32
TABLE 4.4 FPT0 SHROUD INNER AND OUTER GAP HEAT CONDUCTIVITIES TAKEN INTO ACCOUNT FOR THE STUDIES SUMMARIZED IN TABLE 4.3 33
TABLE 4.5 FPT0 SHROUD MATERIAL PROPERTIES USED FOR SCDAP/RELAP5 CALCULATIONS 34
TABLE 4.6 SEQUENCE OF EVENTS CALCULATED WITH SCDAP/RELAP5 37
TABLE 7.1 SUMMARY OF THE FPT0 TEST CONDUCT AND CHARACTERISTIC EVENTS OF BUNDLE DEGRADATION OBSERVED 68

1 INTRODUCTION

The Phebus FP experimental test series aims primarily at the investigation of the fission product behaviour under severe accident conditions in a light water reactor (LWR) [1]. However, as far as the tests starting from intact bundle geometry are concerned, an important additional objective is the investigation of all basic phenomena of core degradation and their interactions during the course of a severe core damage accident.

The first experiment, Phebus FPT0, was performed in 1993 [2,3] and simulates a large break LOCA without supply of any emergency core cooling using real reactor materials. In comparison to other bundle tests like CORA [4,5], PBF SFD1.4 [6], LOFT-LP-FP2 [7], in FPT0 higher temperatures were reached for a longer time, resulting in a larger amount of molten fuel. So, nearly all physico-chemical phenomena of core degradation [8,9,10] occurred up to the formation of a molten pool.

Thus, Phebus FPT0 supplies an excellent database for test analyses to assess the capabilities of computer codes like SCDAP/RELAP5 to predict core degradation. Under this aspect this report describes the application of SCDAP/RELAP5 for post-test analyses of Phebus FPT0. In this work a study has been performed to investigate the influence of varied parameters on the core degradation behaviour. This analytical effort shows the necessity of detailed modeling of the experimental peculiarities like heat transfer through the bundle shroud as well as the necessity to improve some models. Therefore, in this report an improved shroud model for SCDAP/RELAP5 is also presented and its influence on the post-test calculations is assessed.

In section 2 of this report, the experimental set-up as well as the course of the experiment with the characteristic experimental observations are presented. In section 3, the state-of-the-art of the Severe Core Damage Analysis Package (SCDAP) of SCDAP/RELAP5 [12] is discussed briefly. In section 4, the experimental results and the post-test calculations with SCDAP/RELAP5 will be compared to each other. Finally, a best-estimate calculation is defined out of this comparison and discussed.

These post-test calculations of Phebus FPT0 with the SCDAP/RELAP5 computer code had been taken up as part of an international benchmark exercise organized in the frame of the Phebus FP project [11]. This benchmark will go on with FPT1 experiment in which the influence of irradiated fuel is investigated. Because no modeling of burn-up is available in the code, the work of code improvement and assessment has to continue.

2 THE PHEBUS FPT0 EXPERIMENT

This section is subdivided into two parts: We start with the description of the FPT0 bundle, i.e. the bundle geometry and related bundle component data, the axial and radial power profiles and the boundary conditions in terms of the transient bundle power and steam mass flow rates during the test (section 2.1). These data have been obtained from the Phebus-Databook [13,14,15]. Then we give some brief outlines of the test conduct and the respective experimental observations during and after the test concerning the bundle behaviour (section 2.2).

2.1 Description of the FPT0 bundle

2.1.1 Geometry

The dimensions are representative to those of a French N4 nuclear power-plant except for limited length. Figure 2.1 shows a cross-section of the bundle which is 1.1 m long and is heated on a length of 1 m. The test bundle consists of a central Ag-In-Cd control rod with SS cladding and Zircaloy guide tube, an inner ring of eight and an outer ring of twelve fuel rods. Four internal Zircaloy stiffeners support the bundle arrangement (Figure 2.2b). There are two Zircaloy spacer grids located at axial elevations of 0.247 m and 0.767 m, respectively, from the bottom of the fuel stack. The test bundle is surrounded by a shroud consisting of different material layers separated by two gaps (Figure 2.2a). On the outer surface of the Inconel pressure tube the bundle is cooled by water. Table 2.1 summarizes the data concerning bundle components, geometry and material compositions. The material properties taken into account for the calculations are given in section 4.

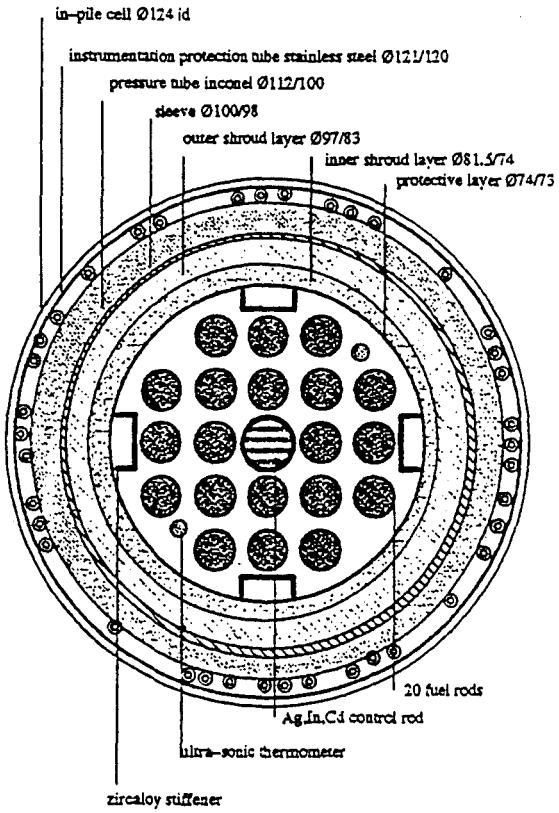

Figure 2.1 Cross section of the Phebus FPT0 bundle [14]

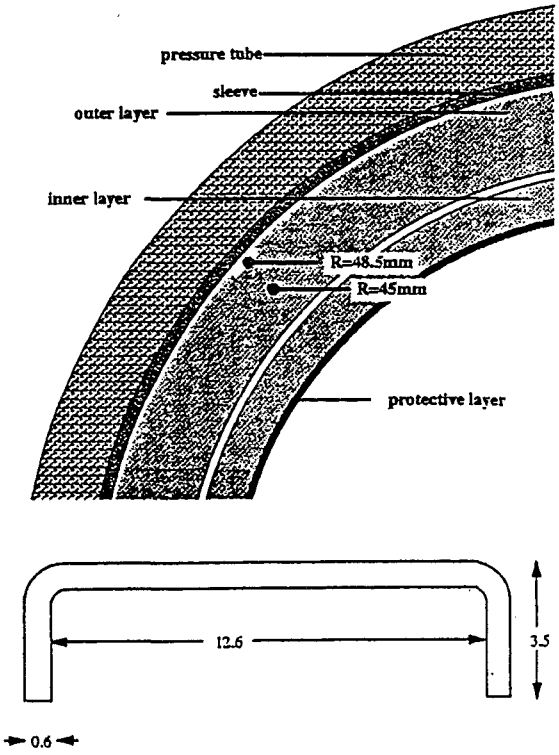

Figure 2.2 Cross section of the shroud, the given radial positions are the outer and inner thermocouple positions, respectively (a); cross section of a stiffener, measurements in mm (b) [14]

Fuel Rods					
	Material	Length	Inside Diameter	Outside Diameter	Thickness
fuel	UO_2	1 m	-	8.19e-3 m	4.095e-3 m
cladding	Zircaloy	1.1125 m	8.36e-3 m	9.50e-3 m	0.570e-3 m
length of cladding above absorber stack			0.0825 m		
length of cladding below fuel stack			0.0300 m		
pitch			12.6e-3 m		
fuel density			10.48 g/cm^3 at 4.14% porosity		
burnup			0 GWd/$t_{Uranium}$ (9 days in-situ irradiation)		
volume upper plenum			2.335 e-6 m^3		
volume lower plenum			0 m^3		
filling gas			Helium, 2.8 MPa at 293 K		

Absorber Rod					
	Material	Length	Inside Diameter	Outside Diameter	Thickness
absorber	Ag-In-Cd	1 m		8.66e-3 m	4.33e-3 m
cladding	steel (304)	1.1015 m	8.75e-3 m	9.70e-3 m	0.470e-3 m
guide tube	Zircaloy	1.1100 m	11.30e-3 m	12.10e-3 m	0.400e-3 m
length of cladding above absorber stack			0.0825 m		
length of cladding below absorber stack			0.0190 m		
length of guide tube above absorber stack			0.0825 m		
length of guide tube below absorber stack			0.0275 m		
filling gas			air, 0.1 MPa at 293 K		

Shroud				
	Material	Inside Diameter	Outside Diameter	Thickness
inner protective layer	Zirconia	73e-3 m	74 e-3 m	0.50 e-3 m
inner layer	Zirconia	74e-3 m	81.5e-3 m	3.75e-3 m
gap	Steam	81.5e-3 m	83e-3 m	0.75e-3 m
outer layer	Zirconia	83e-3 m	97e-3 m	7.00e-3 m
gap	Steam	97e-3 m	98e-3 m	0.50e-3 m
sleeve	Zirconia	98e-3 m	100e-3 m	1.00e-3 m
pressure tube	Inconel 625	100e-3 m	112e-3 m	6.00e-3 m

Stiffeners			
Material	Mass per stiff.	Length	Surface
Zircaloy	0.073 kg	0.945 m	0.037 m^2

Spacer Grids			
Material	Mass per sp. Gr.	Height	Thickness
Zircaloy	0.0782 kg	43 mm	0.4 mm

Table 2.1 Geometrical data and materials of Phebus FPT0 bundle components [14]

2.1.2 Axial and radial power profiles

The axial power profile for a non-degraded fuel rod is plotted in Figure 2.3 together with the list of normalized axial power factors. For an analyst the data is given in detail in a table beside.

Height from bottom of fuel (m)	Axial power factor (m)
0.05	0.28
0.15	0.77
0.25	1.25
0.35	1.53
0.45	1.59
0.55	1.48
0.65	1.30
0.75	0.99
0.85	0.60
0.95	0.21

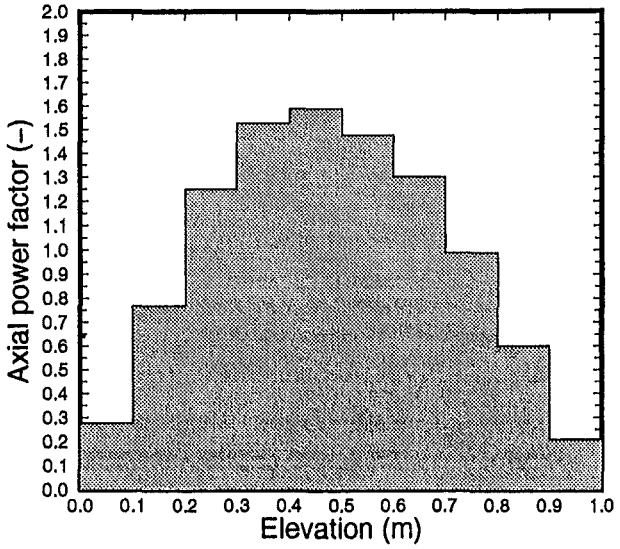

Figure 2.3 Axial power profile in terms of normalized power factors [14]

The radial power profiles for the non-degraded bundle with intact control rod and for the degraded bundle after the complete loss of the control rod are given in Figure 2.4.

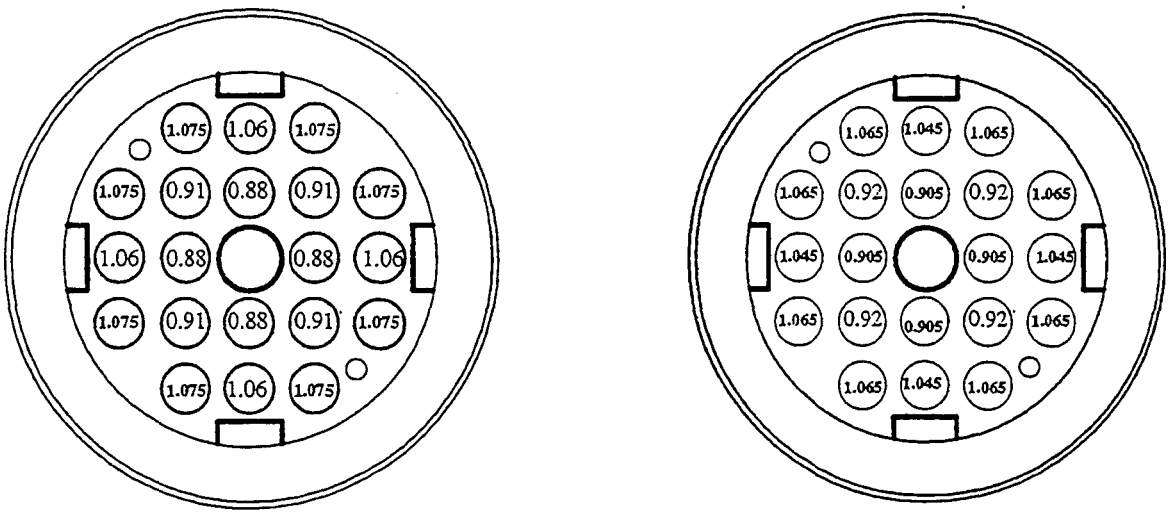

Figure 2.4 Normalized radial power factors with intact control rod (left) and after loss of absorber material (right) [14]

2.1.3 Time dependent conditions

The power history during the test deduced from the Phebus reactor power taking into account the neutronic coupling factors, is shown in Figure 2.5 together with the steam flow rate at bundle inlet. Table 2.2 summarizes the power and inlet steam flow rate data vs. time. The relatively high steam flow rate at the beginning provided a thin oxide shell due to pre-oxidation which usually

occurs also in real reactors. Rising up the power during the first 10140 s step by step with a low steam flow rate caused temperature plateaus with different values that were used to calibrate the measurement instrumentation. The subsequent linear steep power and steam flow rate increase after 10140 s defines the actual beginning of the test. Moreover, the steam inlet temperature is 483 K for the whole test. The temperature of the water flow along the outer surface of the Inconel pressure tube is constant at 438 K.

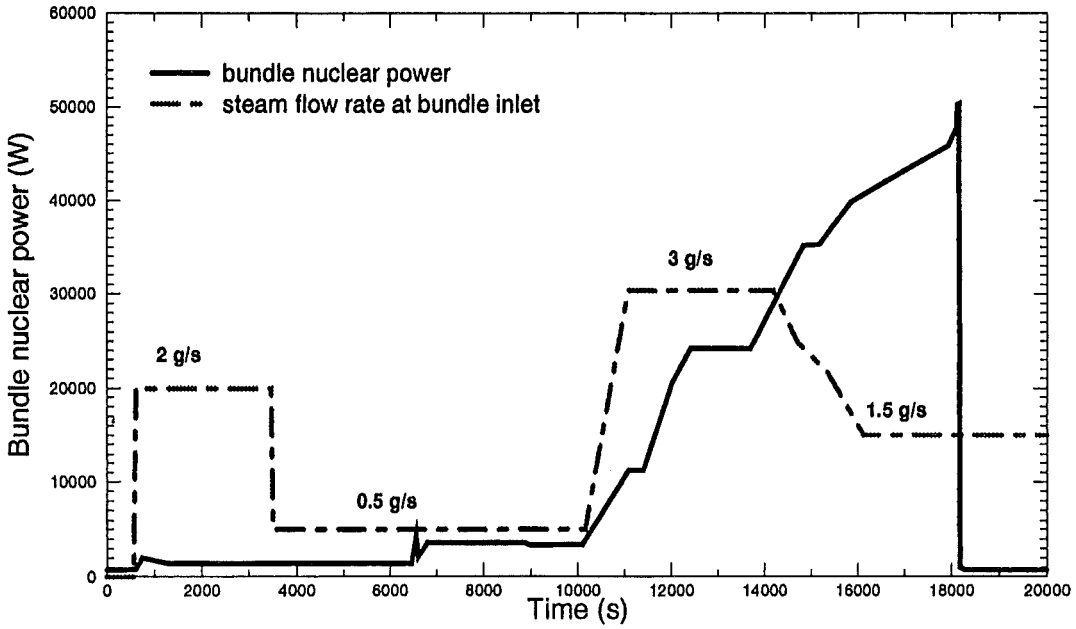

Figure 2.5 Phebus FPT0 bundle power and inlet steam flow rate vs. time

Time (s)	0	600	745	1275	6485	6560	6600	6800	8850
Power (W)	750	850	2050	1440	1440	1980	2270	3700	3700
Time (s)	9000	10140	11090	11400	12020	12410	13680	14830	15170
Power (W)	3420	3500	11230	11230	20600	24220	24220	35250	32250
Time (s)	15850	17925	18100	18120	18140	18190	18300	20000	
Power (W)	39500	45900	47850	49130	50400	1000	750	750	

Time (s)	0	560	600	3445	3500	10140	11080	14180	14720
Steam (g/s)	0	0	2	2	0.5	0.5	3.0	3.0	2.5
Time (s)	15350	16120	20000	20360					
Steam (g/s)	2.2	1.5	1.5	0					

Table 2.2 Bundle power and steam flow rate at bundle inlet

2.1.4 Location of the bundle thermocouples

The axial and radial positions of the thermocouples referred to in this report are given in Figure 2.6. Because only one fuel rod could be instrumented with one thermocouple the thermocouples at different axial and radial positions were distributed to different fuel rods in azimuthal direction [14]. This supposes an equal temperature distribution in azimuthal direction which of course could not be guaranteed for the whole test. The measurements of some shroud thermocouples at 0.4 m deviate from each other by ca. 150 K [11]. The ultrasonic thermocouples (TUS) (see Figure 2.1) have failed very early in the test and will be not considered in the following.

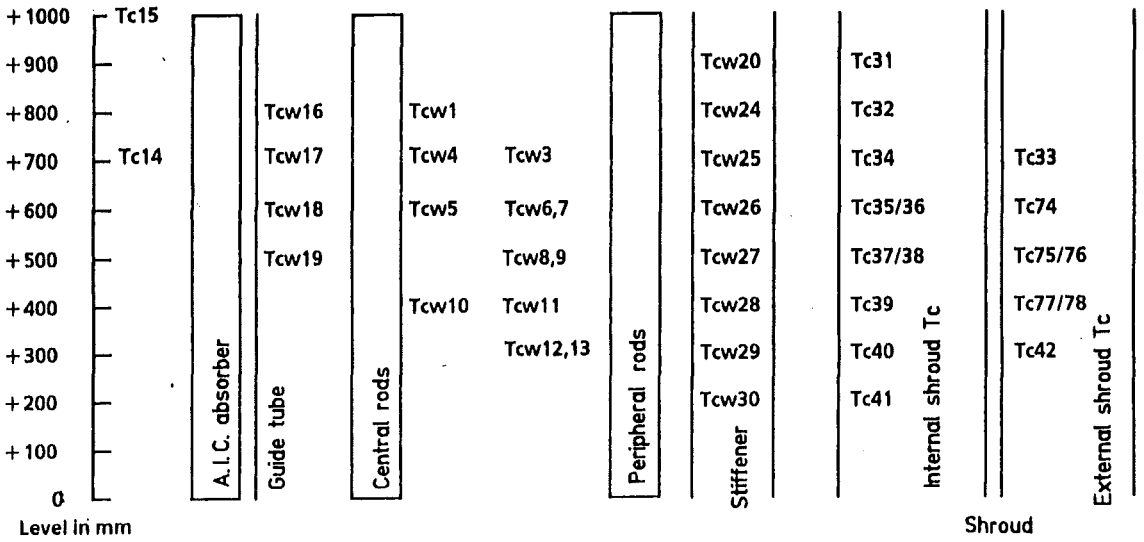

Figure 2.6 Scheme of the radial and axial positions of thermocouples for temperature measurements in the bundle and in the shroud [2]

The fuel rod thermocouples (TCW) were located inside the fuel pellet [14]. Due to the thin cladding, the good heat conduction and the low power density of UO_2 the radial temperature profile of the fuel rod is rather flat. The shroud thermocouples (TC) were leaded through afterwards refilled small holes in the outer shroud layers.

The high-temperature thermocouples for temperature measurements inside the bundle use W/Re thermal elements with ceramic sheath and isolations. Generally, the uncertainty band around the thermocouple readings below 2000 K can be assumed to be ±1...3 %. In the high-temperature region above 2000 K, two additional factors must be taken into account which may also results in measuring errors [16]:

1. The ceramic thermocouple isolation may become semi-conductive at high temperatures which causes a skip down of the emf-voltage (problem of shunting errors),
2. In the course of the degradation process of bundle components, liquefied material may attack the thermocouple and form a new junction.

Both phenomena tend to indicate lower temperatures (by up to 200 K) than in the reality.

2.2 Bundle behaviour during the experiment

Based on the test scenario we distinguish two pronounced test phases:

(start)
|
(1) pre-transient (calibration) phase 0 . . . 10140 s
(2) transient heat-up phase 10140 . . . 18140 s
|
(reactor scram)

In the following the test conduct is described considering the different test phases and their corresponding experimental observations concerning the bundle behaviour. Experimental data reflecting the bundle behaviour are:

- temperature measurements in the bundle itself and the shroud,
- hydrogen production rates deduced from measurements outside the bundle,
- on-line aerosol measurements (OLAM) outside the bundle indicating indirectly the course of bundle degradation,
- post-irradiation examination (PIE), a detailed microscopic investigation (including all destroying and non-destroying examinations) of the test fuel with some cuts across the bundle that provides information about the residual material compositions and the final geometrical state of the bundle.

The experimental findings outlined in the following are restricted to those which can or should be calculated by the severe core damage analysis tools applied like SCDAP/RELAP5. The experimental information referred to in the following is essentially extracted from [2,17].

The Table 7.1 in the appendix summarizes bundle related course and key-events of the experiment in detail. Instead of that table here a short overview is given in Table 2.3.

Name	Time	Event
Plateau 1	0-3445 s	
Plateau 2	3445-6485 s	
Plateau 3	6485-10140 s	Cladding rupture at 6930 s
Control rod failure and oxidation phase	10140-13000 s	First significant H2 detected at 10000 s First indication of control rod failure at 10960 s Oxidation escalation at 12000-12470 s
Melt relocation	13000-15170 s	Second period of H2 generation First indication of relocated material towards the lower spacer grid at 15000 s
Molten pool formation	15170-18140 s	Molten pool formation at 18000 s

Table 2.3 Overview of FPT0 test conduct and key-events

2.2.1 Pre-transient Phase

The pre-transient phase is mainly dedicated to the calibration of the thermocouples and to the instrumentation check. There are three different plateaus of increasing fuel temperatures reached stepwise by mutual change of bundle power and steam mass flow rate (see Figure 2.5), with maximum bundle temperatures of 733 K, 873 K and 1173 K, respectively. As an example Figure 2.7 shows measured fuel rod and shroud temperatures at the axial level of 700 mm of the heated length of the fuel rod [2].

Figure 2.8 shows the axial profiles of bundle temperatures measured at the corresponding ends of the plateaus 2 and 3.

During the pre-transient phase, a sudden increase of radioactivity release measured in the test circuit downstream the bundle at 6930 s indicated cladding rupture.

2.2.2 Heat-up Phase

The start into the high-temperature phase of the experiment was initiated by an increase of power and an increase of the steam mass flow rate from 0.5 g/s to 3 g/s reached at about 11080 s (see Figure 2.5). We distinguish in the following (see Figure 2.7) the phases of

- control rod failure and Zircaloy oxidation escalation ... 13000 s
- melt relocation and begin of bundle collapse ... 15000 s
- bundle degradation with molten pool formation ... 18140 s.

The periods are approximate with some overlapping between the phases.

Signals from a gamma spectrometer at 10960 s and 11920 s indicated control rod failure and massive control rod degradation, respectively. Between 12000 s and 13000 s, temperature escalation due to rapid Zircaloy cladding oxidation was measured by the thermocouples, see Figure 2.9, with maximum fuel rod temperatures of about 2600 K. For the oxidation phase, Figure 2.10 shows the evolution of the axial temperature profile in the bundle. It is evident, that the Zircaloy oxidation begins in the upper part of the bundle resulting in a very skew temperature profile. During this oxidation period, about 70 % of the Zirconium inventory in the bundle is oxidized resulting in the production of hydrogen (Figure 2.11).

Up to now there is no clear experimental evidence whether fuel rod degradation due to molten Zircaloy-UO_2 chemical interaction and failure of oxidized cladding had begun already during the oxidation phase between 12000 s and 13000 s. Only the On-line aerosol monitor (OLAM) detected a significant amount of released radioactivity which may indicate some fuel relocations. However, PIE revealed attack of fuel in the uppermost part of the bundle and accumulation of resolidified fuel on the upper and lower spacer grids which probably happened during this period [2,18].

Between 13000 s and 15000 s thermocouple measurements show some abrupt changes at high temperature level in this period which must be argued to be related to consequences of melt relocation processes (Figure 2.12). Additionally, the observed temperature rises coincide with a second period of hydrogen production (Figure 2.11) which may indicate oxidation of relocating metallic Zircaloy. More details are, however, not known jet.

Bundle collapse and pool formation events are overlapping processes so that the definition of separate phases is somehow arbitrary. Anyway, both the continuous increase of temperatures

inside the bundle beyond 2500 K (Figure 2.9) and the significant rise in shroud temperatures in the lower part of the bundle after 15000 s (Figure 2.13, Figure 2.14) are a strong evidence of a severe bundle degradation ending up in the formation of a molten pool in the axial region between 200 mm and 300 mm above the lower spacer grid.

Figure 2.15 gives an overview of the test sequence by means of the temperature evolution in the bundle as measured by the thermocouples. Because of almost complete thermocouple failure inside the bundle prior to 15000 s, the high temperature level in the very late phase of the experiment has been extrapolated from the temperatures measured in the shroud.

At 18140 s the experiment was terminated by reactor scram. Post-test radiography and tomography gave insight into a severely damaged bundle (Figure 2.16): about 50 % of the fuel inventory had relocated into a molten pool (axial section 2 of the radiography), causing a voided region in the central part of the bundle where the inner fuel rods had completely disappeared whereas residual outer fuel rod stacks were still present (tomographies on the right side of Figure 2.16).

The PIE resulted in final axial profiles of non-relocated UO_2 masses for the inner fuel rods and for the complete bundle as given in Figure 2.17 [17].

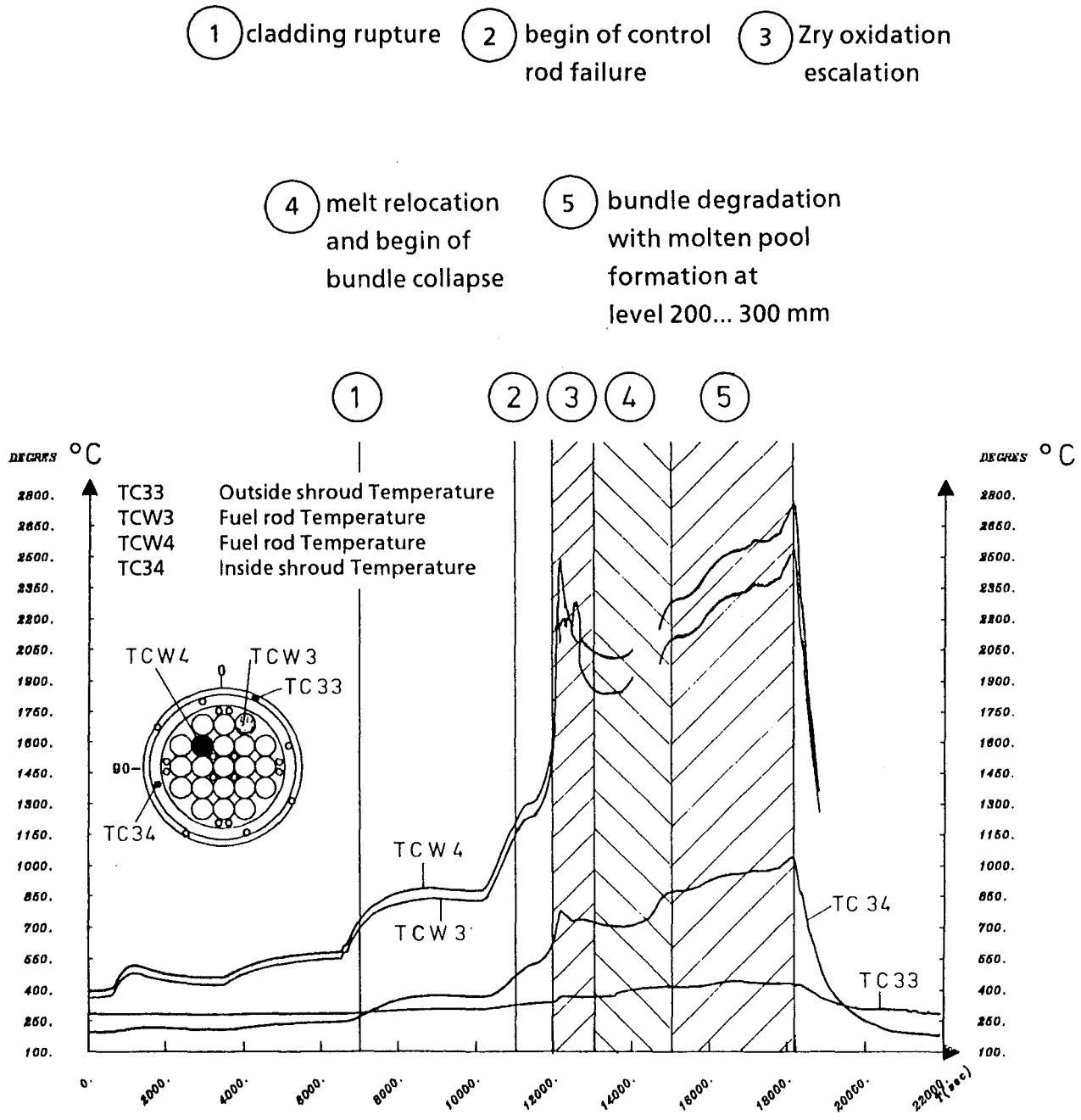

Figure 2.7 Phebus FPT0 test scenario with measured fuel rod temperatures at 700 mm and significant events of the bundle degradation [2]

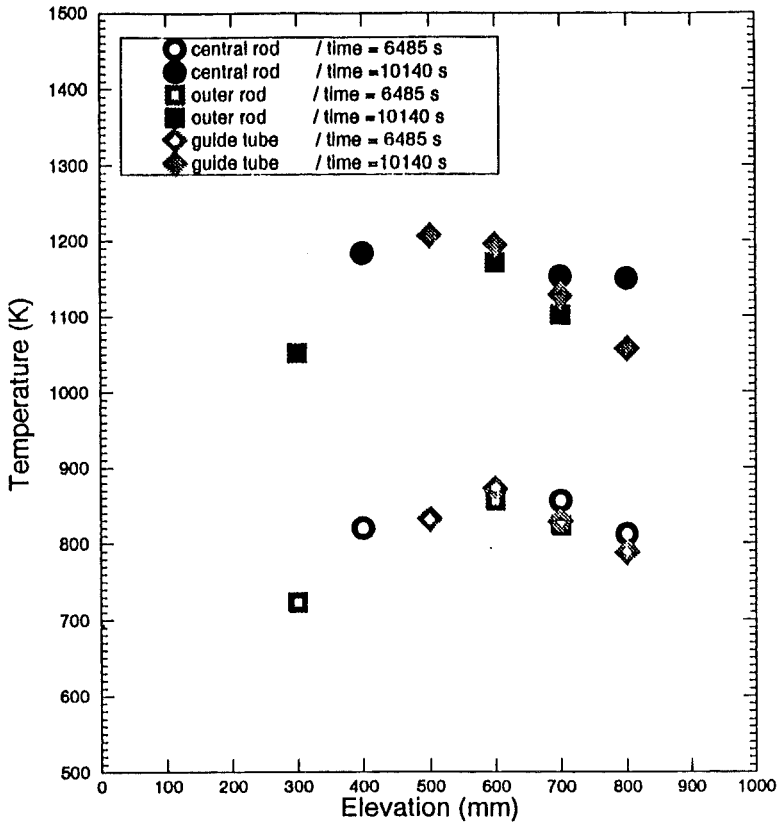

Figure 2.8 Axial temperature distributions measured during the calibration phase at 6485 s and 10140 s

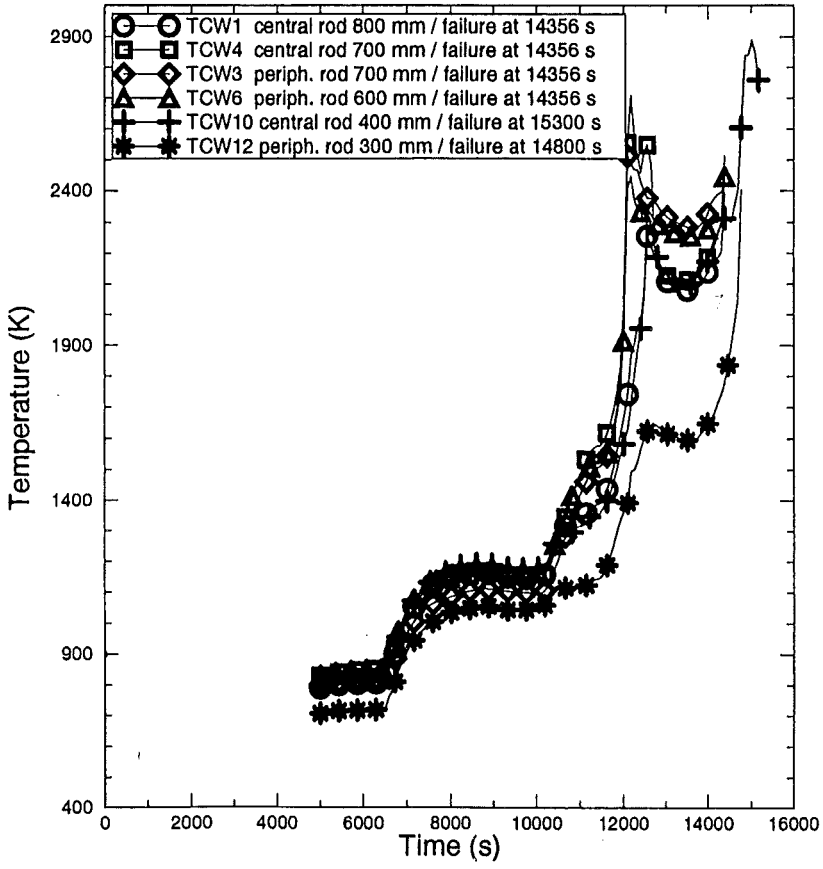

Figure 2.9 Evolution of fuel rod temperatures during the FPT0

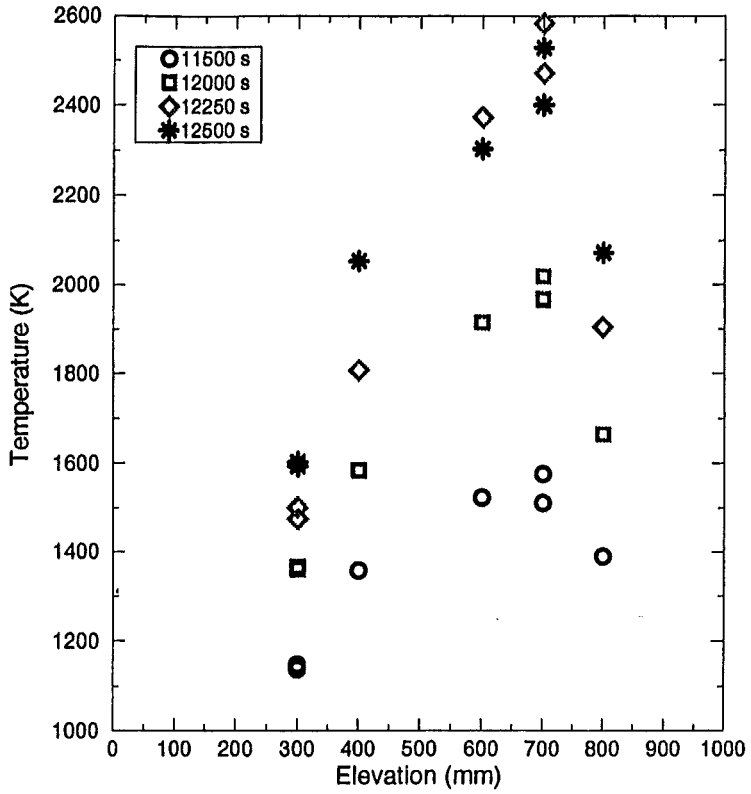

Figure 2.10 Evolution of axial temperature profiles during the oxidation phase

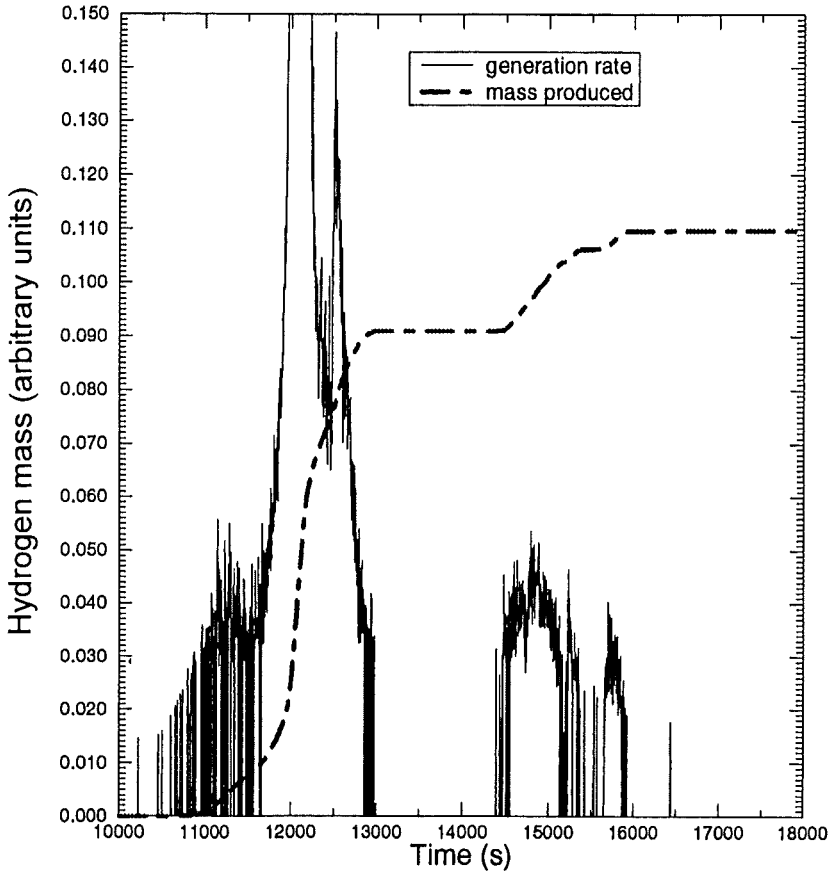

Figure 2.11 Hydrogen generation rate and cumulative hydrogen mass for Phebus FPT0 [11]

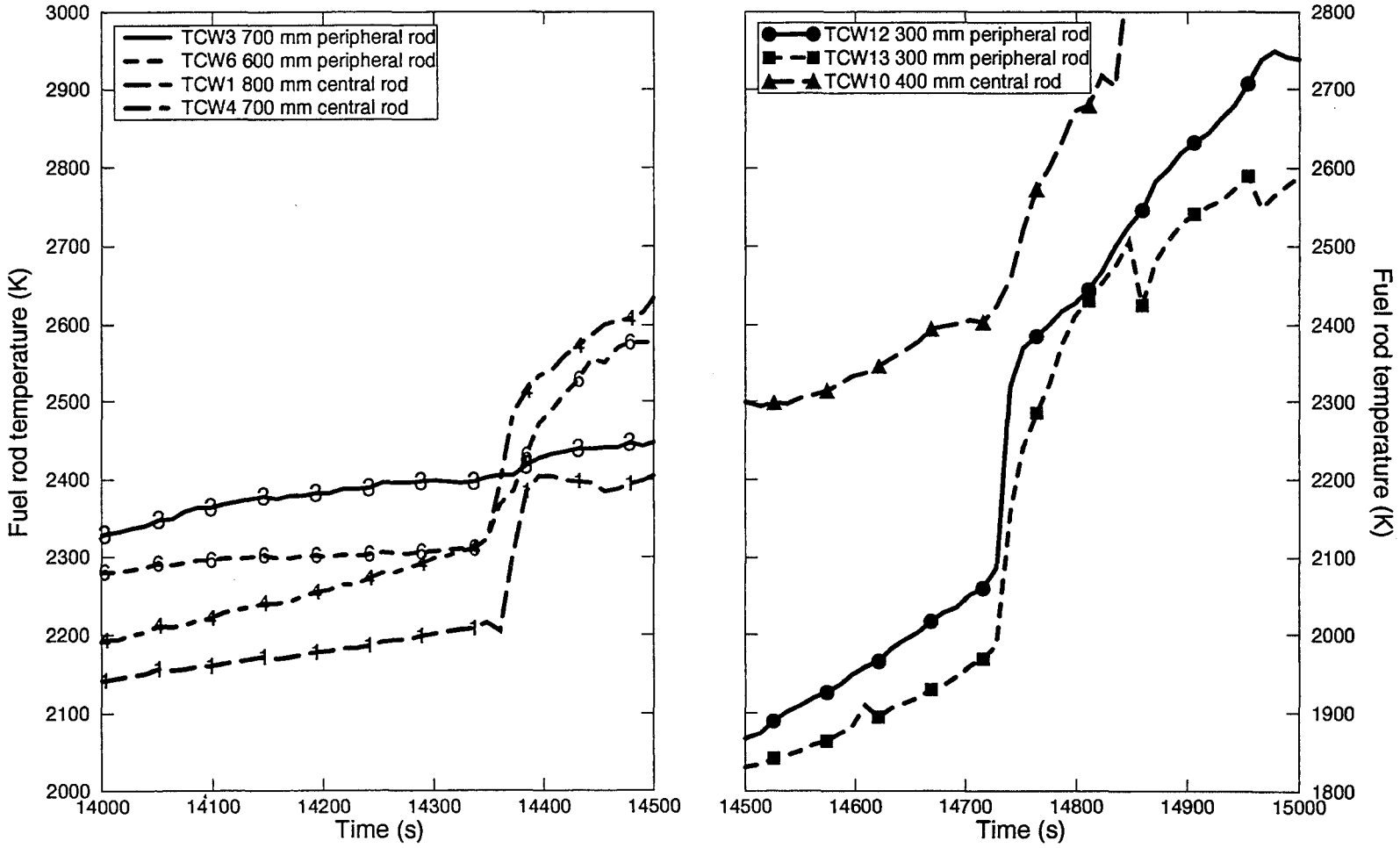

Figure 2.12 Fuel rod temperatures measured during the bundle degradation phase indicating melt relocation and bundle collapse

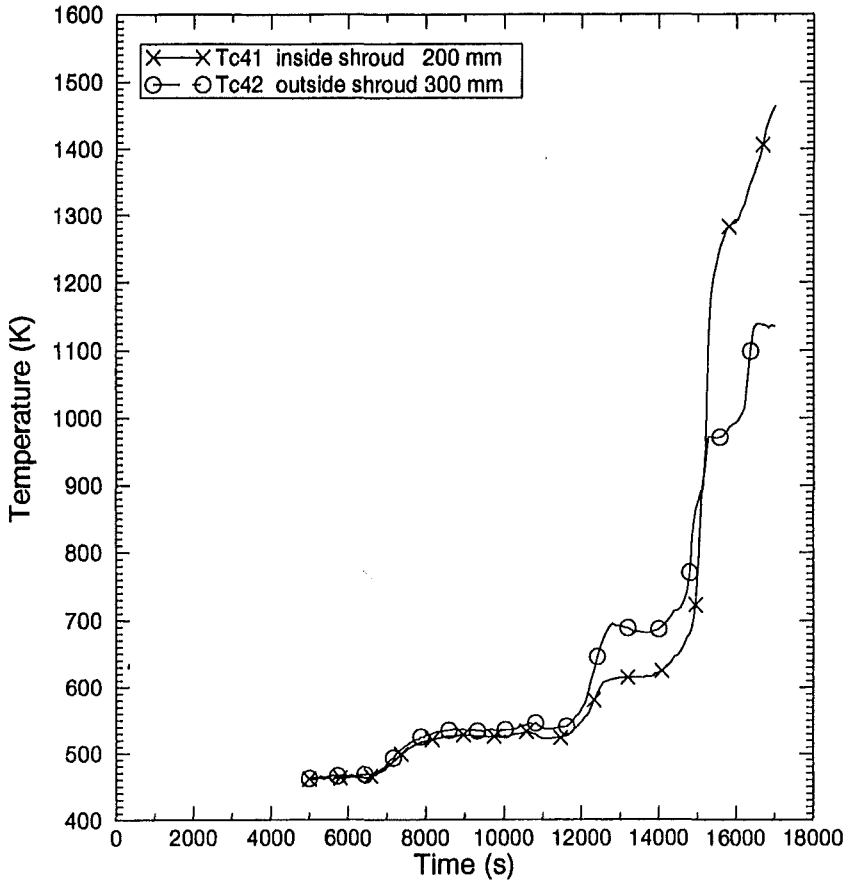

Figure 2.13 Shroud temperatures measured during the bundle degradation phase indicating pool formation

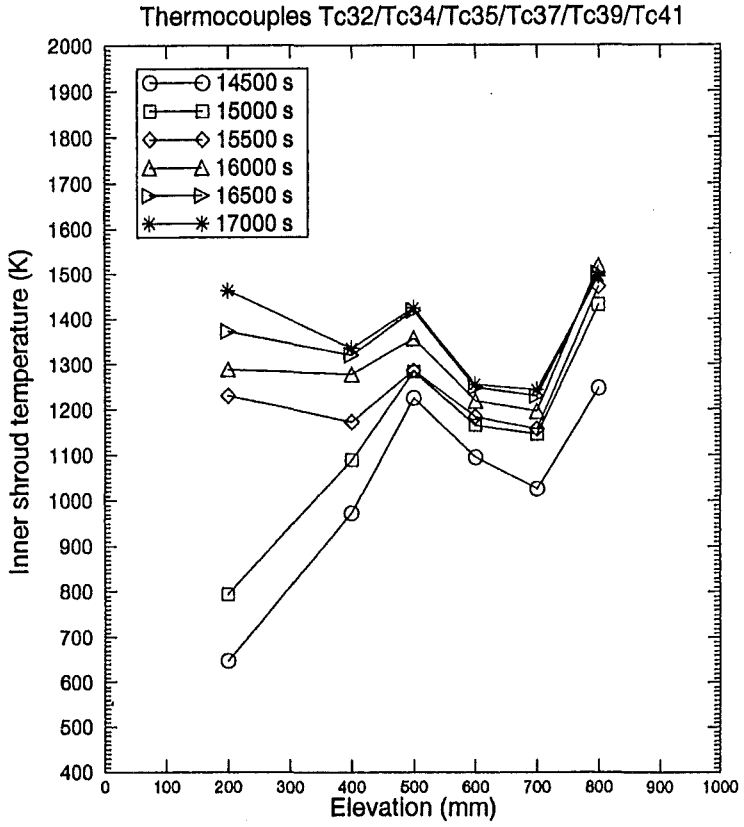

Figure 2.14 Evolution of axial temperature profiles in the shroud indicating strong heat-up in the lower bundle region during the pool formation phase

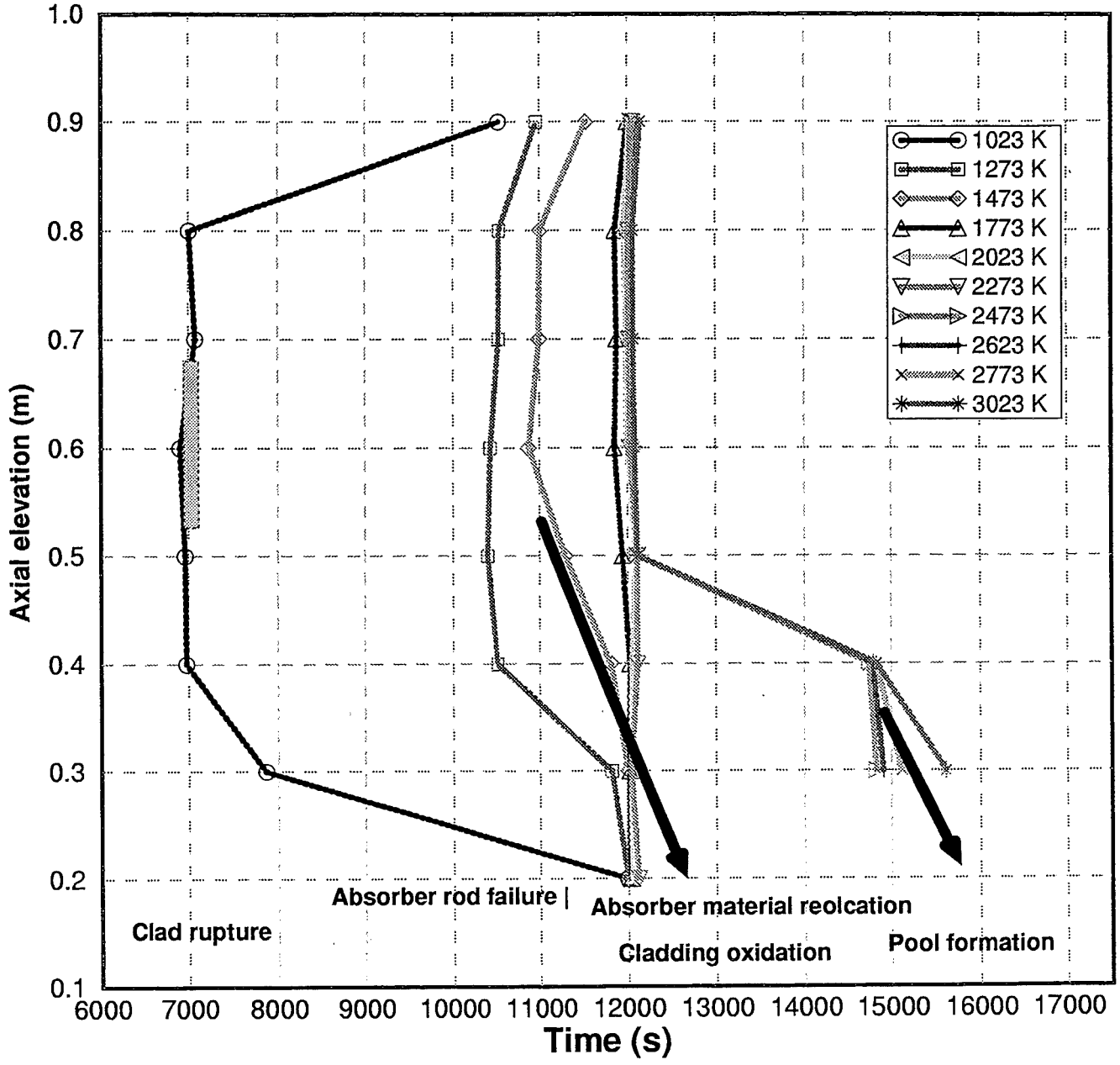

Figure 2.15 Scheme of evolution of the axial temperature profiles as measured in the bundle

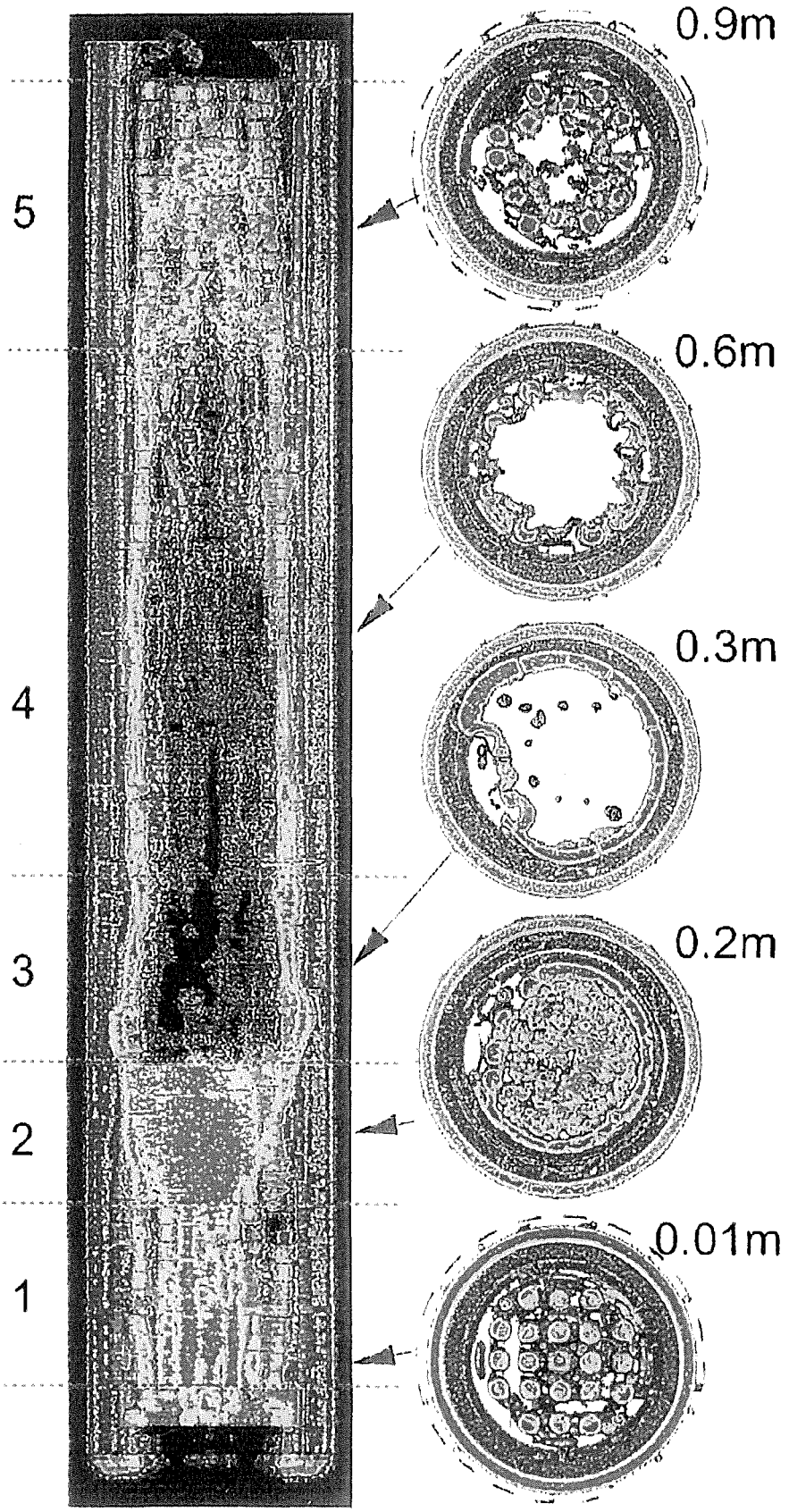

Figure 2.16 Final bundle state with mass distributions deduced from radiography and tomography [17]

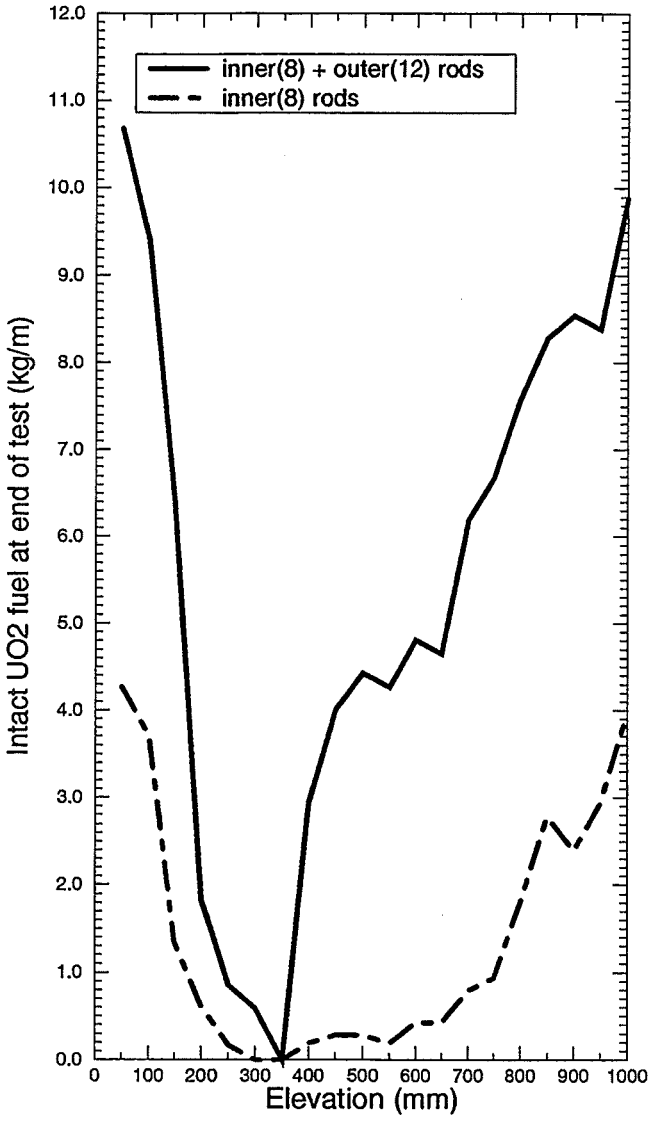

Figure 2.17 Final axial distribution of intact UO_2

3 SCDAP/RELAP5 CAPABILITIES ESSENTIAL FOR PHEBUS FP

3.1 Modeling of in-vessel phenomena

The intention of the Phebus FP test series is to simulate a prototypic severe core damage accident scenario, so that the most significant phenomena and processes occurring can be investigated and detailed mechanistic codes such as ICARE2 [19] or SCDAP/RELAP5 [12] can be validated. Except for the release and transportation of fission products most phenomena can be modeled sufficiently starting from core uncovery, although there are still improvements necessary.

3.1.1 Core heat-up

3.1.1.1 Power source and distribution

In Phebus the decay power is simulated by fission power due to the neutron flux supplied by the external driver core [1]. This neutron flux from the driver core defines the axial power profile by its chopped cosine shape in axial direction corresponding to the axial length of the driver core (see Figure 2.3). In SCDAP/RELAP5 the nuclear heat generation can be simulated quite well up to the point when uranium material relocation takes place using the pre-calculated coupling factors [3].

In case of „pure" decay heat the power source density is only dependent on the power history of the fuel, whereas in a fission powered in-pile test the internal power density of the fuel varies according to the axial neutron flux shape. This indicates that the heat-up of a molten pool at the lower end of the heated length may be overestimated in SCDAP/RELAP5 since the power factors are different from reactor and code situation:

1. The neutron flux becomes reduced inside the pool by self-shielding processes (absorption, reflection),
2. the power source diminishes when the pool relocates downwards since there is a rapid drop of the neutron flux density at the lower end.

In the SCDAP/RELAP5 calculations the nuclear power driving the bundle heat-up is realized as a power table for the axial power profile and radial power distribution. It is supplied by the Phebus staff as a result of the pre-test neutronic calculations.

Hand calculations using the total fission power history, the changes of the radial power distribution given in the Phebus-Databook [13,14], and the time interval of the absorber rod failure showed that a distortion of the axial power profile is possible assuming that the absorber rod did not fail completely at one time. The radial power distribution takes also into account the meltdown of the Ag-In-Cd absorber material. The concerning axial and radial power distributions within the Phebus FPT0 fuel rod bundle is shown in Figure 2.3 and Figure 2.4.

3.1.1.2 Radial heat losses

The heat sink is mainly due to radiative heat transfer to the shroud and heat conduction in the insulation materials of the shroud. This radial heat conduction is calculated by a 2-D-conduction model. Also possible gaps in the shroud are simulated by this model in the original code. However, just at this point code improvements were necessary (see section 3.2.3).

In SCDAP the viewfactors, describing the radiative coupling inside the bundle between adjacent component surfaces are computed only at the beginning so that geometry changes such as ballooning cannot be considered correctly. Since the radiation heat transfer becomes dominant only beyond 1000 K the viewfactors were calculated concerning the ballooned fuel rod geometry which occurs at around 7000 s (see Table 3.1).

a)

from ...↓ to ...→	Inner fuel rod	Control rod	Outer fuel rod	Stiffener	Shroud
Inner fuel rod	.4259e+00	.1328e+00	.3918e+00	.4956e-01	.0000e+00
Control rod	.8338e+00	.7556e-01	.9061e-01	.0000e+00	.0000e+00
Outer fuel rod	.2612e+00	.9617e-02	.2481e+00	.6601e-01	.4151e+00
Stiffener	.1256e+00	.0000e+00	.2508e+00	.0000e+00	.6236e+00
Shroud	.0000e+00	.0000e+00	.6464e+00	.2583e+00	.9526e-01

b)

from ...↓ to ...→	Inner fuel rod	Control rod	Outer fuel rod	Stiffener	Shroud
Inner fuel rod	.8576e-02	.9810e-02	.1141e-01	.1875e-01	.0000e+00
Control rod	.9810e-02	.7200e-02	.2277e-01	.0000e+00	.0000e+00
Outer fuel rod	.1141e-01	.2277e-01	.1039e-01	.5567e-02	.8675e-02
Stiffener	.1875e-01	.0000e+00	.5567e-02	.0000e+00	.8175e-02
Shroud	.0000e+00	.0000e+00	.8675e-02	.8175e-02	.9151e-02

Table 3.1 SCDAP viewfactors (a) and path lengths (b) used in Phebus FPT0 calculations

3.1.1.3 Convective heat losses

The primary fluid component of steam which is superheated at the lower end of the test section to increase the fluid temperature up to 873 K, is assumed to be constant during the course of the experiments. The convection heat losses are in a range of 20 to 30 % of the heat input (nuclear heat and oxidation heat generation since the system pressure is low (app. 0.2 MPa) and the fluid velocities are rather small (app. < 1 m/s). Radiation absorption in the fluid is also restricted due to rather small path lengths of app. 0.01 m and the low system pressure.

3.1.2 Zircaloy cladding rupture

In the temperature range between 1000 K and 1200 K the Zircaloy cladding material undergoes a 2nd order phase transition, the crystal lattice changes form hexagonal (α–phase) to the cubic (β–phase). With this phase change a remarkable drop in the rupture strain is coupled, so that the

fuel rod claddings, which have been ballooned due to the internal pressure may rupture due to the reduced strength of the metallic part of the cladding.

In SCDAP/RELAP5 mod.3.1 a strain based rupture model is available which can be controlled defining the engineering strain, the transition strain and the rupture strain of Zircaloy. Since above 1000 K the oxidation rates of Zircaloy have to be taken into account, the model also considers hardening or strengthening due to a growing oxide layer.

3.1.3 Oxidation

The oxidation model is based on rate equations derived from isothermal experiments. In both releases of SCDAP/RELAP5 the correlation of Urbanic and Heidrick [20] is used. In the code the Pawel/Cathcard [21] correlation is also available. The Urbanic/Heidrick correlation show a steady increase of the oxidation rate with temperature up to 1820 K (low temperature oxidation). Above 1820 K Urbanic/Heidrick observed a rate skip to higher values (high temperature oxidation).

Three mechanisms leading to a possible limitation of the maximum oxidation rate are realized:

1. Steam availability at the ZrO2-fluid interface;
2. Diffusion of steam through a layer of noncondensable gas (hydrogen, argon ...);
3. Diffusion of oxygen through the ZrO2 layer (rate equations).

In the second case an error has been found and corrected in SCDAP/RELAP5 mod.3.1 Rel.F leading to very small differences in case of steam diffusion limit or not.

In case of ballooning the surface area available for oxidation changes locally up to a factor of 250 %. And in case of subsequent clad bursting situations the steam has access to the inner surface of the fuel rod claddings, which are still metallic. The axial extent of the double-sided oxidation can be restricted concerning the relative strain of the cladding. However, the code does not start to compute inner side oxidation as a new item, it only doubles the outer oxide layer thickness. Due to this fact, typical limitation values are restricted to cladding strains of < 5 % (see section 4.4).

A discrepancy was found in the calculation of the hydrogen production which is realized based on the clad mass increase correlation. This value differs from the rate equations used to compute the growth rate of the ZrO_2 and the α-Zr(O) thickness [22]. A correction of this deviation is underway.

In case of reduced steam concentration at the outer surface the code only reduces the layer growth, a typical „steam starvation" situation, where the ZrO_2 layer is reduced by growing α-Zr(O) layer is not taken into account.

3.1.4 UO_2 Dissolution

The UO_2 dissolution starts with the melting of the metallic Zircaloy. The melting point of metallic Zircaloy depends on the oxide concentration and can vary from 2033 K up to 2330 K. Presently Hofmanns correlation [23] is used, but only applied for the precipitation phase. The saturation phase where molten Zircaloy dissolves quickly the UO_2 pellet is modeled as instantaneous offset of dissolved UO_2 (35.8 wt% UO_2 content in molten Zircaloy). Since here two competing processes reduce the available Zr mass in the liquid metal (oxidation and dissolution of UO_2), the onset of UO_2 dissolution indicates that the oxidation is stopped.

3.1.5 Oxide shell failure

The user defines the criteria (temperature and maximum oxide layer thickness) for clad failure. In the calculations presented in this report usually the failure temperature criterion was set to 2350 K. The stable oxide layer thickness amounts to 60% of the initial Zircaloy layer. To test the influence of a higher failure temperature, which is only realistic if a slow temperature rise occurred before, the failure temperature was set to 2500 K in one case (see section 2.1.4).

3.1.6 Melt release, relocation, and blockage formation

In SCDAP/RELAP5 mod.3.1 Rel.D and Rel.F two different materials are allowed to relocate during the early core melt phase:

Absorber material of the control rod:
Absorber materials composed of Ag-In-Cd relocate along the absorber rod guide tube and collect at an elevation where the surface temperature is below 800 K. No radial melt spreading is considered. All molten material above the breach participates in the relocation process. In Rel.D the absorber rod is modeled to fail only due to melting of the stainless steel cladding (1769 K). In Rel.F, however, the eutectic interactions between the stainless steel cladding and the Zircaloy guide tube can lead to earlier melt ejection. Radial melt spreading is not modeled, however, the interaction kinetics between Ag and Zircaloy are investigated [8].

Fuel rod materials:
Fuel rod materials composed of Zr-U-O relocate when the cladding fails. All liquefied material at failure location is assumed to relocate as a thin film on the cladding surface with a constant velocity in one single process. Heat is exchanged between cladding surface and molten material but not with the fluid surrounding the fuel rod. Moreover, in Rel.F the new droplet relocation model allows to simulate a quasi non-cylinder symmetrical material relocation by assuming individual droplet relocation. The main parameters of this model were assessed against CORA experiments [12]. Now, also the metallic debris is allowed to be oxidized concerning the Zr content in the ternary Zr-U-O mixture.

3.1.7 Behavior of a molten pool

3.1.7.1 Molten pool formation

A molten pool can be formed from two starting configurations:

1. starting from a debris bed which has been formed after previous melt relocation. Then an ideal mixture of all materials within the Zr-U-O debris is assumed and the liquidus temperature of this composition is the initial pool temperature.

2. starting from oxidized claddings surrounding a pellet stack. Then, exceeding the melting temperature of either ZrO_2 or UO_2 , melt contacts the other still solid components of the fuel rod leading to a rapid liquefaction since the temperature level is above the eutectic temperature of a Zr-U-O compound.

Once a molten pool has been formed, the program bypasses the normal calculations for fuel rod geometry. Unfortunately, the radiative heat transfer between the pool and surrounding structures is disabled and the crust of the molten pool only radiates to the surrounding fluid. Due to this insufficient model a correct heat transfer calculation is not possible futheron.

3.1.7.2 Pool spreading

The axial zone below the pool is filled with debris which heats up due to the reduced convective heat transfer. When the average debris temperature exceeds the pool formation criteria mentioned above, the debris is transferred to part of the molten pool. Then additional material from the pool situated above fills up the available space since the porosity is reduced to zero due to liquid materials. The pool also grows when still intact fuel rod columns above the pool reach the criteria for melting and slump into the molten pool.

In radial direction the pool can only grow when the adjacent zone reaches one of the criteria mentioned above. Since the crust temperature is always below liquefaction temperature this can occur only due to decay heating of the fuel rods.

3.1.7.3 Crust failure

In SCDAP/RELAP5 two types of crusts are calculated: an upper and a lower crust. The stability of the crusts are calculated by an energy balance. If the heat flux at the outside is larger than that on the inner surface (to the molten pool) the crust can grow and is stable. So far no mechanical failure is considered, since no physical data of a crust composed of a mixture of Zr-U-O is available.

There are two options to set a crust failure criterion — a lateral crust failure which occur early, and a bottom crust failure which may occur very late. Since the Phebus FPT0 test was terminated early the first criteria was selected. Nevertheless these models are very simple and not completely tested. As a consequence the crust is calculated to be rather stable if the fluid acts as an efficient heat sink as in Phebus or in reactor applications. An improved model taking into account the pressure history inside the pool as an additional force acting on the pool crust is foreseen for SCDAP/RELAP5 mod.3.2.

3.2 Code improvements

The most important improvements are the enhanced applicability of the code by adding a SCDAP restart capability and the error correction as well as the improvement of existing models.

3.2.1 Restart capability

The SCDAP input parameter set required for code validation calculations and reactor applications have been checked and a set of parameters was defined for the enhanced restart capability. This new SCDAP restart option is activated if a ***card 40000100*** is found in the restart input deck. At the moment following cards are allowed to be modified on restart:

40000100: allows to modify the power flag and shatter trip (however, this function is not yet tested).

40000300:

ZrO_2 Failure Temperature:	tmpfal
Stable oxide shell fraction:	frcoxf
Double-sided oxidation limit:	epsox2
Radiation heat transfer limit:	voidrd

Here the code checks the state of the simulated fuel rods whether or not the damage state has reached values so that a change of the parameters causes unpredictable and unreliable results. If

these conditions are not fulfilled the restart is not accepted and the user is prompted to use an earlier restart number. For each component the user may specify with the ***40cc4xxx cards*** the type of oxidation limitation factors:

40cc4xxx:	LIMIT ON:	steam diffusion through a non-condensable layer
	LIMIT OFF:	oxygen diffusion through ZrO_2 layer
(new)	LIMIT AUTO:	depending on the axial conditions at each rod surface and the fluid composition the limitation is set to ON or OFF.

In case of double-sided oxidation it is assumed that steam diffusion limitation is only valid for the inner surface of the cladding whereas at the outer surface the limitation is due to oxygen diffusion in the ZrO_2 layer (LIMIT AUTO).

After correcting a dimension error in the limitation formula in subroutine statep.F, the differences between unlimited and limited oxidation became negligible, so that this restart option can be removed.

3.2.2 Improvements for 2-D heat conduction heatc2

In our efforts to model FZK out-of-pile test facilities we found that the first and last axial nodes of the simulator have a fixed temperature indicated by the ***card 4ccc0250+1***. So these zones do not participate in the convective heat transfer to the fluid. Especially for the projected QUENCH facility, where a fluid inlet from the bottom is planned, this causes problems [24]. Therefore, we defined the boundary temperature mentioned above at the axial ends of the end-zones and calculated the nodal temperature as a function of 2-D heat conduction, convective heat transfer, and radiation. This allows to make assumptions about the temperature response of the copper electrodes and to compute a realistic energy balance. During this work the coding was improved with respect to vectorization increasing total code efficiency (app. 3 %).

3.2.3 Phebus specific shroud model

From the CORA experiments [4,5] it is known that the exact modeling of the shroud and its material properties is mandatory to correctly calculate the bundle behaviour because the thermal conductivities influences the temperature level in the bundle which in turn has a strong impact on the various processes of core degradation. Though the material property data in question are essentially known [13], there remains an open problem: to model the behaviour of the various gaps between the individual material layers.

The original program, SCDAP/RELAP5 mod.3.1, cannot handle variations of the gap width due to the fixed mesh used for heat conduction solution. Gap deformation or radiation heat transfer across a gap cannot be treated in a realistic manner. The only way is to adjust the thermal conductivity of the gap material (gas/steam) globally by modification of the static input table for SCDAP. Therefore, an improved shroud model has been developed and implemented into the FZK/IRS version of SCDAP/RELAP5 mod3.1 Rel.F. It takes into account both variation of gap widths due to thermal expansion of the shroud material layers and radiation heat transfer across gaps.

The improved shroud heat transfer model is based on the original heat conduction model using a fixed mesh and modeling purely heat conduction transfer. To calculate the material expansion leading finally to gap closure the original heat conduction coefficient $\lambda_{M,original}$ is corrected by the ratio of temperature dependent local gap width $s_{M,new}$ and fixed gap width $s_{M,original}$ of the original model:

$$\lambda_{M,new} = \lambda_{M,original} \cdot \frac{s_{M,original}}{s_{M,new}} \quad (1)$$

Radiation across the gap is written formally like conduction heat transfer. Thus, the overall heat conduction coefficient λ_{eff} results in:

$$\lambda_{eff} = \lambda_{M,original} \cdot \frac{s_{M,original}}{s_{M,new}} + s_{M,original} \cdot \sigma\varepsilon \cdot \left[T^2_{M,original,in} + T^2_{M,original,out}\right] \cdot \left[T_{M,original,in} + T_{M,original,out}\right] \quad (2)$$

where σ is the Stefan-Boltzmann constant, ε the radiation exchange coefficient and $T_{M,original,in}$ and $T_{M,original,out}$ are the calculated temperature at the inner and at the outer side of the gap, respectively.

The new model does not need any parameter to be prescribed by the user or to be calibrated by comparison with experimental results. Therefore, the code is now able to predict more accurately the heat transfer out of the bundle and capable to provide reliable pre-calculations. For more details about this model see the Appendix (section 7.2).

3.3 Test specific properties for FPT0

In a first approach a very detailed nodalization scheme was developed. The bundle is divided in radial direction into three rings (Figure 3.1). Two Zircaloy spacer grids are at elevations of 247 mm and 767 mm, respectively. The dimensions are extracted from the Phebus-Databook [13].

The two additional tungsten ultrasonic temperature sensors are taken into account as a net flow area reduction. The four stiffeners are modeled as hollow fuel rods, the pellets are not simulated. To maintain the Zircaloy surface area, Zircaloy mass, and the Zircaloy thickness eight „stiffener" components had to be used. Figure 3.1 shows the arrangement of the stiffener components within the fuel rod bundle.

The fuel rod bundle is surrounded by a cylindrical shroud composed essentially of two Zirconia layers enclosed by an Inconel pressure tube cooled by water on the outer side. Across the shroud the nodes for heat conduction are arranged to fit the radial temperature gradient in an appropriate way. Since the user defined materials are limited in SCDAP/RELAP5 mod3.1 Rel.D, the gap heat conduction values are modified so that they include the radiative heat transfer, too.

The inner ring as well as the absorber are linked to the inner pipe (21xx), the outer ring to the center pipe (31xx) and the stiffeners as well as the shroud inner surface are linked to the outermost pipe (41xx). At the outside of the Inconel pressure tube the water channel removes heat to the Phebus heat exchanger [1].

The central absorber rod as well as the inner and outer ring are normal SCDAP components whereas the stiffeners are modeled as hollow fuel rods without UO_2 pellets. This allows to scale the Zircaloy mass as well as the Zircaloy surface so that the hydrogen production as well as the total mass is not influenced by any scaling distortion.

The main disadvantage of this detailed input deck was the large computation time. To overcome this insufficient behaviour, the input deck was simplified to a 2-channel input deck (see Figure 3.2). In this report the results were compared with the experiment and with results gained by the 3-channel version.

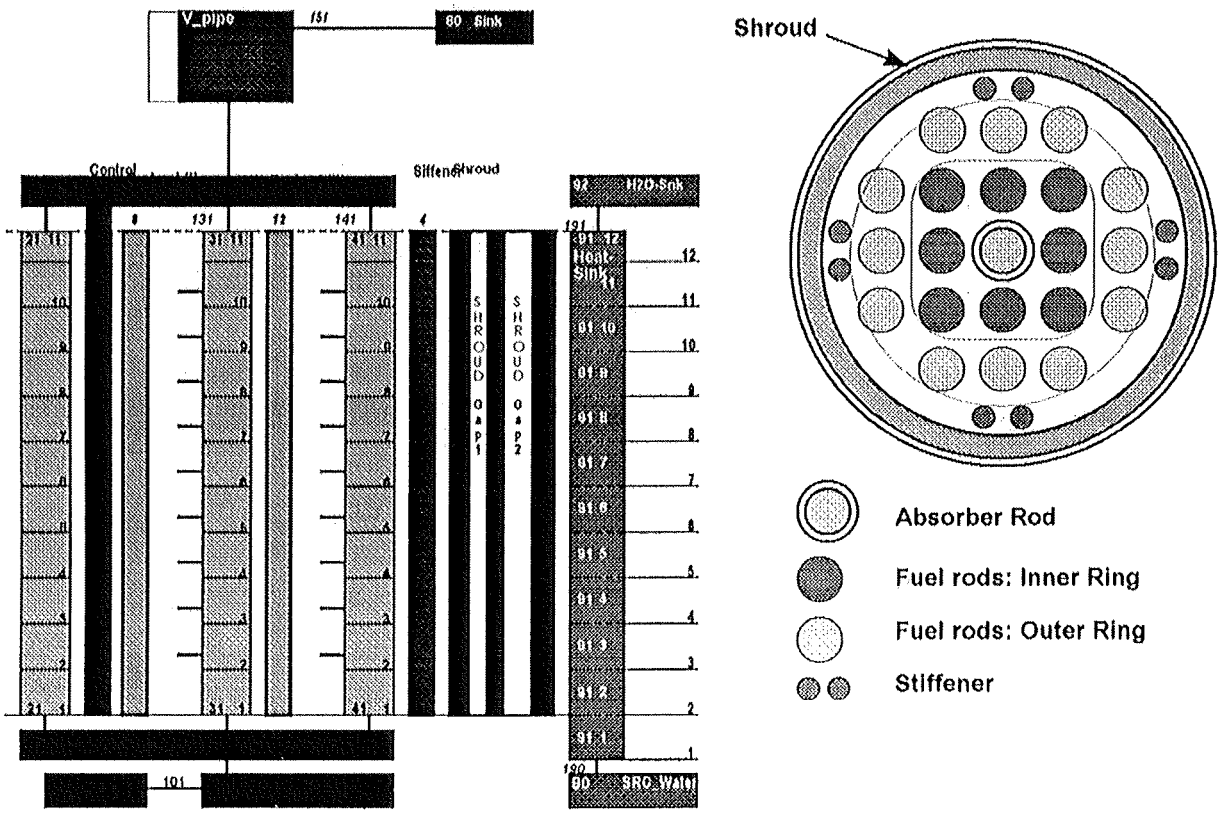

Figure 3.1 Axial and radial discretization of the Phebus test section including three parallel channels with cross flow junctions and a water channel around the shroud.

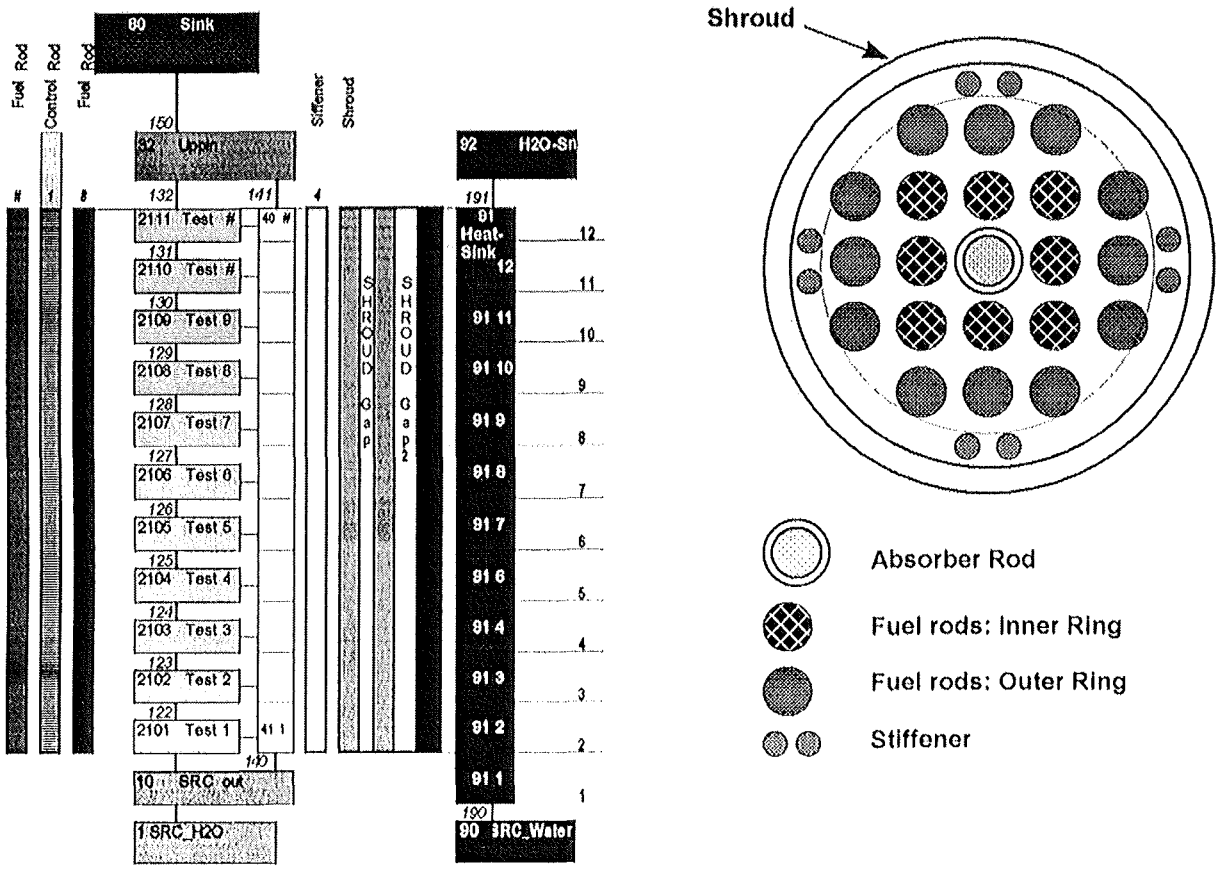

Figure 3.2 Simplified fast running SCDAP/RELAP5 model of the Phebus test section

4 COMPARISON OF EXPERIMENTAL AND CALCULATIONAL RESULTS

4.1 Goals of the study

Starting from a detailed 3-channel model, a 2-channel model (see Figure 3.2) has been derived, considered in the following as the standard (2-ch-root) input model (see section 3.3). This simplified input model, consuming considerably reduced CPU time, has been applied for parameter studies by varying both some physical model parameters and the axial discretization of the bundle components and the radial discretization of the fuel rods. This effort aimed at the identification of the influence of these model variations onto the results of the calculations measured in terms of:

a) evolution of fuel rod and shroud temperatures,

b) evolution of the hydrogen mass produced by Zircaloy oxidation,

c) correspondence in time scales of significant events such as:

- cladding ballooning and rupture,
- control rod failure and release of Ag-In-Cd melt,
- failure of oxidized cladding and release of Zr-U-O compound,
- begin of ZrO_2-UO_2 ceramic melting and subsequent molten pool formation.

These calculational data and events will be compared with the corresponding experimental findings.

Because of evident shortcomings in the SCDAP/RELAP5 models describing heat transfer across bundle components during the molten pool formation phase (see section 3.1.7.1), the calculations have been stopped during early pool formation much prior to the nominal end of the experiment. Thus, there will not be any comparison done for data characterizing this late bundle degradation phase.

At first, the parameter studies mentioned above have been performed with SCDAP/RELAP5 mod 3.1 Rel.D (cases (1) - (11)). This parameter study should provide firstly the range of possible influences of changing those parameters and secondly best-estimate parameters and nodalizations. Anticipating the result, the range of the influence of parameter variations is quite small and that was the reason why an improvement of the existing shroud model became necessary. Therefore, the results of this parameter study will not be discussed in detail in the following but mentioned as a more or less broad scatter band in comparison to the calculations with the improved shroud model.

From this parameter study we have obtained the following best-estimate parameters and nodalization which then were used for the subsequent calculations:

- axial nodalization: 20 nodes
- radial nodalization:
  - fuel rod: 4 nodes in pellet; 2 nodes in cladding
  - shroud: 14 nodes

- number of hydrodynamic channels: 2
- extend of double-sided oxidation: 2 % clad strain
- clad failure temperature: 2350 K

After SCDAP/RELAP5 mod 3.1 Rel.F had become available, these additional calculations have been performed with a SCDAP/RELAP5 Rel.F code version which includes the new shroud model mentioned in section 3.2.3 offering a more realistic simulation of the shroud heat transfer properties and thus of the temperature level inside the bundle (cases (12) - (15)).

The meaning of a here so called calculational route is a superposition of best-estimate parameters derived from the parameter study and best-estimate models. Since the knowledge of core degradation increases, more and more parameters can be substituted by models. Thus, since the beginning of this task the following parameters used in our calculational route were substituted:

- oxidation limit on/off due to error correction
- use of defined artificial heat conductivities and emissivities by the improved shroud model

The case (13) of this report includes all these best-estimate parameters and models except the axial nodalization of 20 axial nodes. Nevertheless, we now define this calculation as our best-estimate calculation.

4.2 Investigated parameters of the sensitivity study

The SCDAP input data of the three-channel and two-channel standard cases are identical and summarized in Table 4.2. The physical and numerical model parameters varied in the frame of the sensitivity study with SCDAP/RELAP5 rel.D refer to Table 4.3:

- axial nodalization (11, 12, and 20 elevations)
- radial nodalization in fuel rods and shroud
- cladding oxidation (limited, unlimited, in cases (12) to (15) error corrected)
- axial extension of doublesided oxidation (5 % and 10 % clad strain)
- cladding ballooning and rupture (yes, no)
- oxidized cladding failure criteria (temperature)
- shroud gap heat conductivities.

Table 4.4 lists the shroud inner and outer gap heat conductivities taken into account for the calculations, and Table 4.5 lists the material property data of the solid shroud material layers which were recommended by the Phebus staff and have not been varied in the frame of this study.

The nominal axial power profile as given in section 2.2 changes when the central control rod begins to fail and Ag-In-Cd melt relocates. In order to take into account the transition conditions from a bundle with intact control rod to a bundle with degraded control rod, the axial power factors have been changed for the time period between 11000 s and 11500 s as given in Table 4.1. The information about the degree of change of axial power profile during this time period has been deduced from the Phebus reactor power [2]. This evolution of the axial power profile is assumed for all cases (1) to (15) calculated with SCDAP/RELAP5.

Elevation [m]	t≤11000 s	11000 s≤t≤11500 s	t≥11500 s
0.05	0.28	0.27	0.28
0.15	0.77	0.73	0.77
0.25	1.25	1.18	1.25
0.35	1.53	1.46	1.53
0.45	1.59	1.52	1.59
0.55	1.48	1.41	1.48
0.65	1.30	1.44	1.30
0.75	0.99	1.09	0.99
0.85	0.60	0.66	0.60
0.95	0.21	0.22	0.21

Table 4.1: Axial power profile used in the Phebus FPT0 calculations

Number of axial nodes in the bundle components	11
Axial node lengths for all nodes	0.1 m
Component 1: inner fuel rods (8) Component 3: outer fuel rods (12)	
Number of radial nodes in fuel/cladding	4/2
Oxidized cladding failure criterion (T = cladding temperature; ds(ox) = oxide layer thickness)	$T \geq 2350$ K and $ds(ox) \leq 60\%$
Minimum cladding strain for double-sided oxidation	2%
Cladding rupture strain by ballooning	18%
Cladding strain for transition from sausage type deformation to localized deformation	15%
Strain limit for rod-to-rod contact	20%
Pressure drop caused by ballooning modelled	yes
Oxidation limitation for inner/outer rods	off/on
Component 2: control rod (1)	
Number of radial nodes in absorber+SS cladding in guide tube	4/2 2
Component 4: Stiffeners (8) modelled as pseudo fuel rods	
Number of radial nodes	4
Stiffener „fuel pellet radius“	2.0e-5 m
Stiffener „inner cladding radius“	2.8e-3 m
Stiffener „outer cladding radius“	3.1e-3 m
Oxidation limitation for stiffeners	on
Component 5: shroud	
Number of radial nodes	14

Table 4.2 SCDAP/RELAP5 input data for the standard three-channel and two-channel models

Run No	Identification	Axial nodalization	Radial nodalization fuel rods fuel/cladding	Oxid. limit. Inner/outer rods	ZrO_2 failure temperature (K)	Cladding strain limit double-sided oxidation (%)	Cladding ballooning on/off	rad. nodes in shroud	Shroud inner/outer gap heat conductivity	SCDAP/RELAP5 code version
1	3-ch-root	11	4/2	off/on	2350	2	on	14	Tab. 4.3	mod3.1 Rel.D(0*)
2	3-ch-limitoff	11	4/2	off/off	2350	2	on	14	Tab. 4.3	mod3.1 Rel.D(0*)
3	2-ch-root	11	4/2	off/on	2350	2	on	14	Tab. 4.3	mod3.1 Rel.D(0*)
4	2-ch-axnod	20	4/2	off/on	2350	2	on	14	Tab. 4.3	mod3.1 Rel.D(0*)
5	2-ch-radnod	11	5/5	off/on	2350	2	on	14	Tab. 4.3	mod3.1 Rel.D(0*)
6	2-ch-balloff	11	4/2	off/on	2350	2	off	14	Tab. 4.3	mod3.1 Rel.D(0*)
7	2-ch-10%strain	11	4/2	off/on	2350	10	on	14	Tab. 4.3	mod3.1 Rel.D(0*)
8	2-ch-5%strain	11	4/2	off/on	2350	5	on	14	Tab. 4.3	mod3.1 Rel.D(0*)
9	2-ch-ZRO2500K	11	4/2	off/on	2500	2	on	14	Tab. 4.3	mod3.1 Rel.D(0*)
10	2-ch-gpc1873	11	4/2	off/on	2350	2	on	14	Tab. 4.3	mod3.1 Rel.D(0*)
11	2-ch-gpc1873radnod	11	4/2	off/on	2350	2	on	20	Tab. 4.3	mod3.1 Rel.D(0*)
12	2-ch-root-rel.F	11	4/2	off/on	2350	2	on	14	Tab. 4.3	mod3.1 Rel.F(1*)
13	2-ch-root-tstgap5	11	4/2	off/on	2350	2	on	14	Tab. 4.3	mod3.1 Rel.F(2*)
14	2-ch-root-all.10c	11	4/2	off/on	2350	2	on	14	Tab. 4.3	mod3.1 Rel.F(2*)
15	2-ch-root-all.10cc	11	4/2	off/on	2350	2	on	14	Tab. 4.3	mod3.1 Rel.F(2*)

0*) original version as received from INEL with a scaling error in the oxidation limitation model
1*) original version as received from INEL with the scaling error in the oxidation limitation model removed
2*) IRS version with the scaling error in the oxidation limitation model removed and with the new shroud model including gap expansion and gap radiation heat transfer

Table 4.3 Model and parameter variations for the FPT0 sensitivity study with SCDAP/RELAP mod 3.1 rel.D and rel.F

Run No.		Shroud gap heat conductivities for temperatures (K)									
		300	550	700	873	1083	1173	1248	1700	2100	2500
1-9	inner gap	0.028	0.0535	0.076	0.109	0.154	0.308	0.60	0.99	1.66	2.38
	outer gap	0.028	0.0535	0.076	0.109	0.154	0.308	0.60	0.99	1.66	2.38
10-11	inner gap	0.028	0.0535	0.176	0.64	0.58	0.59	0.60	0.99	1.66	2.38
	outer gap	0.028	0.0535	0.176	0.64	0.58	0.59	0.60	0.99	1.66	2.38
12-13	inner gap	0.028	0.0535	0.076	0.109	0.175	0.308	0.60	0.99	1.66	2.38
	outer gap	0.028	0.0535	0.076	0.109	0.175	0.308	0.60	0.99	1.66	2.38
14/all.10c: Argon	inner	0.025	0.030	0.035	0.045	0.055	0.065	0.07	0.08	0.09	0.10
	outer	0.025	0.030	0.035	0.045	0.055	0.065	0.07	0.08	0.09	0.10
15/all.10cc: Vapor	inner	0.040	0.045	0.055	0.075	0.120	0.135	0.15	0.23	0.325	0.45
	outer	0.040	0.045	0.055	0.075	0.120	0.135	0.15	0.23	0.325	0.45

Table 4.4 FPT0 shroud inner and outer gap heat conductivities taken into account for the studies summarized in Table 4.3

	Temperature (K)									
Material layer		300	550	700	873	1083	1173	1248	1700	2100	2500
Zirconia inner protective layer	c_p (J/kg K)	419	591	619	637	646	655	659	546	568	637
	ρ (kg/m^3)	5600	5600	5600	5600	5600	5600	5600	5600	5600	5600
	λ (W/m K)	2.0	2.0	2.0	2.0	2.06	2.13	2.186	2.5	3.0	4.0
Zirconia inner and outer layer	c_p (J/kg K)	439	540	568	595	613	581	581	586	635	686
	ρ (kg/m^3)	5000	5000	5000	5000	5000	5000	5000	5000	5000	5000
	λ (W/m K)	0.69	0.75	0.71	0.64	0.58	0.59	0.60	0.99	1.66	2.38
Zirconia sleeve	c_p (J/kg K)	419	591	619	637	646	655	659	546	568	637
	ρ (kg/m3)	5600	5600	5600	5600	5600	5600	5600	5600	5600	5600
	λ (W/m K)	2.0	2.0	2.0	2.0	2.06	2.13	2.186	2.5	3.0	4.0
Inconel pressure tube	c_p (J/kg K)	453	556	523	565	635	622	626	653	678	678
	ρ (kg/m3)	8430	8430	8430	8430	8430	8430	8430	8430	8430	8430
	λ (W/m K)	9.73	13.5	15.8	18.4	21.6	23.0	24.1	31.0	37.1	43.2

Table 4.5 FPT0 shroud material properties used for SCDAP/RELAP5 calculations

4.3 Experimental phases of FPT0

Following the definitions of experimental phases as outlined in section 2.2, we distinguish

1. a pre-transient (calibration) phase up to about 10140s
2. a transient heat-up phase of the bundle with three sub-phases:
    - oxidation phase
    - melt relocation and bundle collapsing phase
    - molten pool formation phase

The principal parameters controlling the course of the experiment are the bundle power and the steam mass flow rate at bundle inlet, see Figure 2.5.

To give a first overview, Figure 4.1 shows the fuel rod temperatures calculated compared with the experimental data for the whole experimental period up to t=16000 s. The calculated temperatures refer to the inner ring of fuel rods. Because of the scarce data pool the experimental data shown are for the inner ring (int.fuel), the outer ring (per.fuel), and for the control rod guide tube (g.t.). The failure time of the thermocouples is specified in the legend. Figure 4.2 shows the corresponding shroud temperatures, related to the outer shroud measuring position at elevation 0.3 m, and to the inner one at positions 0.4 m to 0.8 m (see Figure 2.2).

In the following, we discuss the comparison of experimental versus calculational data in detail for the different phases of the experiment.

4.3.1 Pre-transient (calibration) phase

The initial pre-transient phase is characterized by a controlled heat-up under reduced steam flow conditions, (see bundle power and bundle inlet steam flow rate in Figure 2.5) resulting in distinct temperature plateaus with maximum temperatures of about 1200 K in the bundle. During this phase no steam starvation occurred due to rather low temperatures.

4.3.1.1 Starting conditions at 5000 s

Figure 4.3 shows the experimental and calculational fuel rod temperatures at different axial positions in the bundle for this phase. The first temperature plateau prior to 4000 s at a very low temperature level has been omitted here and in the following because it has not any significance for our considerations. The calculational results generally lie in the uncertainty band of the measured data (see section 2.1.4) with a tendency to over-predict the temperatures in the upper part of the bundle and to under-predict them in the lower part. Figure 4.4 reflects this behaviour showing the axial temperature profiles at 6485 s and 10140 s. Especially for higher temperatures in the bundle at 10140 s, the calculated results clearly show an influence of the variation of the heat conduction properties in the shroud gaps with large differences between the cases (1) to (9) and (12) on the one side without special gap closure modeling and (10), (11), (13) to (15) on the other.

Moreover, Figure 4.4(b) indicates a more accurate calculation of the heat transfer through the shroud by a better agreement of measured and calculated results in the upper part of the bundle (cases (13) to (15)), whereas case (12) performed with the original code version SCDAP/RELAP5 mod3.1 Rel.F without the new shroud heat transfer model shows qualitatively about the same behaviour as shown in Figure 4.4(a) for cases (1) to (9).

The influence of the new shroud heat transfer model becomes more evident in Figure 4.5 which shows measured and calculated shroud temperatures. Here the new shroud model clearly did improve the calculational results considerably (cases (13) to (15)). When we compare measured and calculated shroud temperatures, it must be kept in mind that due to the Cartesian shroud model in SCDAP/RELAP5 (contrary to the cylindrical shroud in the experiment) the calculated shroud temperatures at the radial measuring positions have been estimated to be over-predicted by 30 to 40 K.

4.3.1.2 Cladding ballooning and rupture

Fuel rod cladding rupture by overstrain was recorded during the experiment at 6930 s, see section 2.2. Figure 4.6 shows the cladding radii calculated in the bundle mid-plane which increase by ballooning up to failure by overstrain. The failure times for the different cases, indicated by stagnant radii, lie in a time interval of 100 s and agree rather well with the experimental observation; case (6) had been performed with the ballooning model switched off resulting in no cladding rupture.

Figure 4.7 shows the calculated axial profiles of the cladding strain at the end of the calibration phase with only minor scattering of the calculational results. This figure points out that, although the new shroud heat transfer model has a significant influence on temperature behaviour, the cladding rupture time isn't changed and deviations of the cladding strain between the calculations are very small over the whole axial length.

Table 4.1 summarizes the events of cladding failure by overstrain for the cases (1) to (15) together with characteristic events of bundle degradation during the transient heat-up phase which is discussed in the following.

	Cladding failure by ballooning (s)	Begin of control rod failure (s)	Begin of relocation of (U-Zr-O) (s)	Begin of molten pool formation by UO_2/ZrO_2 melting (s) / Temp. (K)
Experiment FPT0	6930	10778	12000	15000 / -
3-ch-root (1)	6963	11300	11917	14525 /2822.6
3-ch-limitoff (2)	6963	11300	11339	14435 / 2739.0
2-ch-root (3)	7074	11250	11815	14852 / 2822.9
2-ch-axnod (4)	7065	11250	11785	14492 / 2705.3
2-ch-radnod (5)	7073	11500	11350	14350 / -
2-ch-balloff (6)	no failure	11700	11890	15177 / 2822.6
2-ch-10%strain (7)	7074	11700	11826	14592 / 2975.0
2-ch-5strain (8)	7074	11500	11819	14673 / 2822.7
2-ch-ZrO2500 K (9)	7074.3	11300	11906	15056 / 2822.7
2-ch-gbc1873 (10)	7129	11545	11838	14445 / 2756.0
2-ch-gbc1873radnod (11)	7132	11500	11570	14685 / 2874.7
2-ch-root-rel.F (12)	7126	10520	11310	15080 / 2867.3
2-ch-root-tstgap5 (13)	7217	10862	11800	15770 / 2782.4
2-ch-all.10c (14)	7092	10606	11715	15533 / 2863.0
2-ch-all.10cc (15)	7181	10793	11765	15641 / 2863.6

Table 4.6 Sequence of events calculated with SCDAP/RELAP5

4.3.2 Transient heat-up phase

In the following, we subdivide the transient heat-up phase into oxidation phase, melt relocation phase, and begin of molten pool formation as outlined above. Since the bundle is composed of 20 fuel rods and one central absorber rod, a detailed treatment of both components seems necessary. At first we consider the fuel rod behaviour and after that the behaviour of the control rod. The section about fuel rod behaviour is subdivided into the three important phases of the transient heat-up phase mentioned above. This classification is rather arbitrary, and one should keep in mind that these sub-phases are particular overlapping in time, especially the oxidation phase and the melt relocation phase between 12000 s and 13000 s.

4.3.2.1 Oxidation

The oxidation phase starts in the calculations at nearly 10000 s when the temperature exceeds 1000 K. The increase of bundle power and the augmented supply of steam (see Figure 2.5) result in the oxidation temperature escalation with heat-up rates up to 10 K/s at about 12000 s and peak temperatures of 2500 K (Figure 4.8, 10000 - 13000 s).

Comparing experimental and calculational temperature data, we see a good qualitative agreement with some quantitative differences in details. Around the bundle-mid-plane (0.4 m ... 0.6 m), the begin of oxidation temperature escalation and the course of its escalation reflect the experimental findings rather well. Although there is a considerable scattering of the experimental data and some uncertainty concerning the temperature level (see section 2.1.4). Thus, the experimental peak temperatures at 12000 s tend to be higher than the calculated ones by 100 to 200 K.

In the upper part of the bundle at 0.7 m and 0.8 m, cases (1) to (12) (calculations without the new shroud model) show a too early (ca. 500 s) oxidation temperature escalation whereas cases (13) to (15) with the new shroud heat transfer model agree better with the experimental observations concerning the oxidation temperature escalation.

Figure 4.9(a)-(c) showing the axial temperature distribution during the oxidation phase illustrate the beginning of oxidation in the upper bundle part. It is also visible that the oxidation in cases (1) to (12) starts very early while the calculations with the new shroud heat transfer model are in good agreement with the experimental data.

The evolution of the shroud temperatures, at 0.3 m for the outer radial shroud measuring position, from 0.4 m to 0.8 m for the inner positions (Figure 4.10, 10000 - 13000 s) shows an increase corresponding to the bundle temperatures in Figure 4.8. The shroud temperatures follow the bundle temperatures closely. That points out that the heat capacity of the shroud has only a limited influence.

It is evident that only for cases (13) to (15) with the new shroud heat transfer model experimental and calculated temperatures are in a satisfactory agreement, whereas cases (1) to (12) with the original SCDAP shroud model over-predict the shroud peak temperatures during the oxidation phase by up to 300 K. Hence we consider the calculations (13) to (15) with the new shroud heat transfer model to give us the more reliable results in terms of data and events listed in section 4.1 from (a) to (c).

The rapid oxidation of the fuel rods together with the spacer grids, the control rod guide tube and the stiffeners leads to a strong hydrogen generation. Figure 4.11 shows the instantaneous hydrogen generation rates and the cumulative hydrogen mass produced by Zircaloy oxidation. The later onset of temperature escalation due to oxidation calculated for cases (13) to (15) results

in a more delayed hydrogen mass production (compared with cases (1) to (12)) and thus a better qualitative agreement with the measurement. However, the difference to the maximum hydrogen mass measured is about 20 % for cases (13) to (15). This is partly due to an error in the calculation of the contribution of the guide tube oxidation to the cumulative hydrogen mass (app. 5 %), which in SCDAP/RELAP5 mod.3.1 Rel.F is not calculated.

In Figure 4.12(a), the degree of oxidation in the bundle, calculated for all cases, is shown. A representative averaged value of 60 % has to be compared with about 70 % deduced from the measurements [12]. That means that the calculations in general result into a lower oxidation with less hydrogen production in comparison to the experimental measurements (see Figure 4.11(b)).

Figure 4.12(b) to (d) show axial profiles of the degree of oxidation of the inner and outer fuel rod claddings as well as of the stiffeners, respectively, as calculated for the 2-channel reference case (13) with the new shroud heat transfer model. One can see the less oxidation at lower elevations due to lower temperatures and the later begin of oxidation. In the upper bundle the claddings aren't oxidized completely because the oxidation was stopped by exceeding one of the stop-criteria mentioned in section 3.1.3.

4.3.2.2 Melt relocation

After reaching peak temperatures of around 2500 K a subsequent temperature decrease occurs due to the end of rapid cladding oxidation. Hence quasi stationary temperature plateaus are observed at the different bundle elevations with a constant bundle power (Figure 2.5) with fuel rod temperatures from about 1600 K at the lower end of the bundle to about 2200 K in the upper part (Figure 4.8, 12000-14000 s). In this phase UO_2 dissolution by molten Zircaloy, Zr-U-O melt relocation takes place as well as partial formation of coolant channel blockages when melt resolidifies in lower bundle regions.

A comparison of experimental bundle temperatures with calculational results demonstrates a rather nice agreement of the temperature levels during the post-oxidation plateau. At that time the last bundle wide temperature comparison reveals that the conditions in the test section can be represented quite well with the optimized SCDAP/RELAP5 code system.

Unfortunately, most of the thermocouples failed in this phase additionally to the thermocouple uncertainties mentioned in section 2.1.4. This leads to some problems in comparing the experimental with the calculational results and hence in qualifying the calculational results.

Despite of lacking experimental data, a sufficient agreement of experimental and calculational results is confirmed as can be seen in the axial fuel rod temperature profiles during the relocation phase in Figure 4.9(d)-(l). Although the calculational data tends to lower temperatures (the peak temperatures were not attained), the calculations match the measured data, especially the axial temperature gradient, qualitatively well along the whole bundle over the whole time period.

Since melt relocation is initiated by clad failure criteria (see section 3.1.5 and 3.1.6),. this most important temperature criterion was, based on former CORA calculations, fixed to 2350 K except in case (9) using 2500 K. At the end of the oxidation phase and during the relocation phase temperatures between 2200 K and 2500 K were calculated in the upper bundle part. That means whether Zr-U-O melt relocation may happen or not, depends on the fact whether the temperature exceeds 2350 K or not. In some cases the calculated temperature only reaches 2300 K and no relocation happens. This problem points out the importance of a correct temperature calculation and the influence of a few uncertainties in the code (non-linear effects) which can cause even worse results.

In the lower part of the bundle at 0.3 m, Figure 4.8 shows temperature peaks calculated at the beginning of the degradation phase which are not recorded experimentally. This is the consequence of relocated Zr-U-O melt released at higher axial elevations and resolidified above the lower grid spacer.

The shroud temperatures also show in this phase a temperature plateau similar to the bundle temperatures. However, the overestimation of the shroud temperatures in the cases (1) to (12) (calculations without the new shroud model) by nearly 300 K is maintained (Figure 4.10, 12000-14000 s). From the comparison to the results of the cases (13) to (15) with the new shroud model one can derive the significance of a correct modeling of heat transfer through the shroud, especially at high shroud temperatures when radiation heat transfer becomes important and gap closure could be expected.

Figure 4.13(a) and (b) give some information about the sequences of fuel and Zr relocation as the consequence of the release of Zr-U-O melts, respectively, and about the corresponding masses involved in this degradation process originating from chemical interaction of molten Zircaloy with UO_2 and resulting UO_2 liquefaction (UO_2 dissolution by molten Zircaloy) prior to UO_2-ZrO_2 ceramic melting. The initial UO_2 mass in the bundle, as taken into account in the calculations, is 11.75 kg. Cases (1) to (3) show the release of considerable quantities of liquefied UO_2 as the consequence of large amounts of molten Zircaloy enclosed by oxidized cladding and thus liquefying UO_2 until late cladding failure beyond 14000 s, though early partial release is calculated to occur in the range of 11300 s to 11900 s. Most cases indicate the onset of fuel rod degradation in the range of 11800 s and 12000 s, thus reflecting the experimental observation rather well, see Table 4.1.

4.3.2.3 Molten pool formation

Finally, a steep power ramp beginning at about 14000 s (Figure 2.5) results in an increase of the temperature level in the bundle beyond 2800 K and the onset of UO_2-ZrO_2 ceramic melting. This molten pool formation is indicated in the calculations by a steep temperature increase up to 3000 K (Figure 4.8, 14000-16000 s); corresponding thermocouple data are not available because the thermocouples have failed in this high-temperature phase before 14800 s.

As mentioned in section 3.1.7 the molten pool formation inhibits the radiation heat transfer from the crust to the shroud. Since the convective heat losses are rather small and the radiation to the steam leads to a sharp increase of fluid the temperature (Figure 4.8, t>14000 s), the pool becomes nearly adibatic.

This is supported by a steep decrease in shroud temperatures (Figure 4.10, beyond 14000 s). The main reason for this behaviour is the difficulty to describe the surface conditions of a ceramic crust with respect to radiation heat transfer. Due to this shortcomings in SCDAP/RELAP5 the calculations were stopped here unless an improved radiation heat transfer model will become available.

As for the onset of molten pool formation, the calculated results show a broad scattering with the tendency of late onset of pool formation after 15000 s for cases (13) to (15) (Figure 4.14). On-line aerosol measuring devices indeed provide information of the onset of pool formation in the experiment at about 15000 s (see section 2.2).

Figure 4.14 shows the onset of molten pool formation calculated in terms of the evolution of an equivalent pool radius (radius of an equivalent hemisphere containing the liquid pool); the scatter band lies in the range of 14400 s to 15800 s (see Table 4.1), whereas experimental data indicate

onset of molten pool formation at around 15000 s. The calculations have been terminated after onset of molten pool formation due to the model shortcomings mentioned above.

4.3.2.4 Control rod behaviour

Within the heat-up of the whole bundle due to power increase and heavy oxidation also the temperature of the control rod rises correspondingly to the fuel rod temperatures (see Figure 4.8). Finally, the temperature of the control rod exceeds the melting temperature of the absorber material Ag-In-Cd. After the melting temperature of the stainless steel cladding has been reached, release of absorber material occurs as soon as the Zircaloy guide tube fails (see section 3.1.6).

The onset of control rod failure by release of Ag-In-Cd absorber material had been recorded at 10778 s (see section 2.2). In Table 4.1 the onset of control rod failure as calculated by SCDAP/RELAP5 is given, and Figure 4.15 presents the corresponding calculated results in terms of the residual (i.e. not yet relocated) Ag-In-Cd mass of the absorber rod versus time. Here, the onset of absorber rod failure is calculated to be in the range from 10500 s to 11700 s, with cases (13) to (15) representing best the experimental observation. Interesting to see that the absorber rod degradation covers a period of about one hour in the calculations. This outcome reflects a steep temperature gradient towards the lower end of the bundle maintained during the oxidation and melt relocation phases.

The axial temperature distribution during the steep heat-up (Figure 4.9) makes clear that the control rod relocation covers such a long time. One can see here an always steep temperature gradient towards the lower end of the bundle where obviously the melting temperatures (1700 K) were exceeded some times later while already in the upper bundle part material is relocated. Due to a later start of the oxidation escalation in cases (13) to (15) the control rod meltdown is delayed, too.

Although the consequences of control rod meltdown are considered (e.g. changes in the axial power profile by input tables or liquefaction of Zircaloy cladding of adjacent fuel rods by silver or steel), the time of control rod failure practically does not influence the subsequent bundle behaviour.

4.4 FZK/IRS calculational route

Case (13) of this report has been identified to be the FZK/IRS best-estimate calculation and as mentioned before our prefered calculational route. In the following the main advantages of this calculation will be discussed and some additional viewpoints will be given.

Due to the error correction of the oxidation limitation and the introduction of the new shroud model the temperatures of the whole bundle as well as in the shroud can be modeled quite well. Although the temperatures are from time to time quantitatively calculated too low, the qualitative evolution is predicted very good, especially the onset of the oxidation escalation phase.

For case (13) with our new standard (best-estimate) FPT0 input model and application of the improved shroud model, Figure 4.16 shows the evolution of the calculated fuel rod temperatures together with the corresponding experimental temperature histories. Due to the lack of experimental data, Figure 4.16(a) covers only the axial region between 0.3 m and 0.8 m. Moreover, one should be aware of different time scales: the regions of interest are enclosed by black frames.

In principle, Figure 4.16(a) and (b) reflect the satisfactory qualitative agreement, which has already been pointed out by means in section 4.3: The sequences of temperature plateaus indicated by different colour are quite close to the experimental data. However, the differences in detail may be considerable. In general, the measured axial temperature profiles seem to be flatter than calculated, this is already true for the calibration phase. Moreover, the measured data after the oxidation phase indicate a temporally more pronounced and axially extended high-temperature plateau at about 2400 K. A finer axial nodalization (e.g. 20 nodes) will further improve the calculation because also local effects can be considered out in a more satisfactory way. This will of course lead to a more time consuming calculation, however, this is made up by the reduction from a 3-channel to a 2-channel model.

The temperature range from 2800 K to 2850 K in Figure 4.16(a) reflects the molten pool at about 15000 s, whereas the calculation shows the begin of molten pool formation at 15770 s with a pool temperature of 2782 K (see Table 4.1). The deviating contour plot at the right side and the bottom corner of Figure 4.16(a) is due to the failure of the thermocouple measurements.

Figure 4.17 shows for case (13) a comparison of the evolution of radial temperature profiles across the bundle and the shroud at different axial elevations with corresponding experimental data; the terms „g.t.“, „c.r.“, „p.r.“ and „st.“ mark the radial positions of the guide tube, central fuel rods, peripheral fuel rods and stiffeners, respectively. Missing symbols indicate the lack of experimental data due to thermocouple failure.

Although the experimental data are scarce, it is obvious that in a more macroscopic sense both the radial temperature shapes and the temperature development in time as calculated reflect satisfactorily the experimental findings. For $t > 13000$ s, the calculated temperature levels are mostly lower than the experimental data, and bearing in mind possible underestimation of measured temperatures by thermocouple „shunting“ errors at high temperatures (see section 2.1.4), this tendency may become even more pronounced.

It is evident that especially the shroud temperatures calculated with the new shroud model are in good agreement with the experimental data. This means a rather correct temperature profile across the shroud and therefore a correspondingly correct heat transfer through the shroud.

Figure 4.18 compares the sequence of bundle degradation events with the corresponding experimental observations, see Table 4.1. The experimental findings refer to OLAM signals (On-Line Aerosol Monitor) with voltage drops in cases of significant release of radioactivity from the bundle as consequences of a bundle degradation process. The sequence of characteristic events is well reflected by the results of the calculation, case (13). This indicates a correct modeling of cladding failure. That again means a good estimation of the clad failure criteria, especially the failure temperature of 2350 K.

Event 5 was observed very close to the end of the experiment, probably due to the relocation of the molten pool towards the lower end of the bundle with vaporisation of residual Ag resulting in an increase of the pool volume and aerosol release [11].

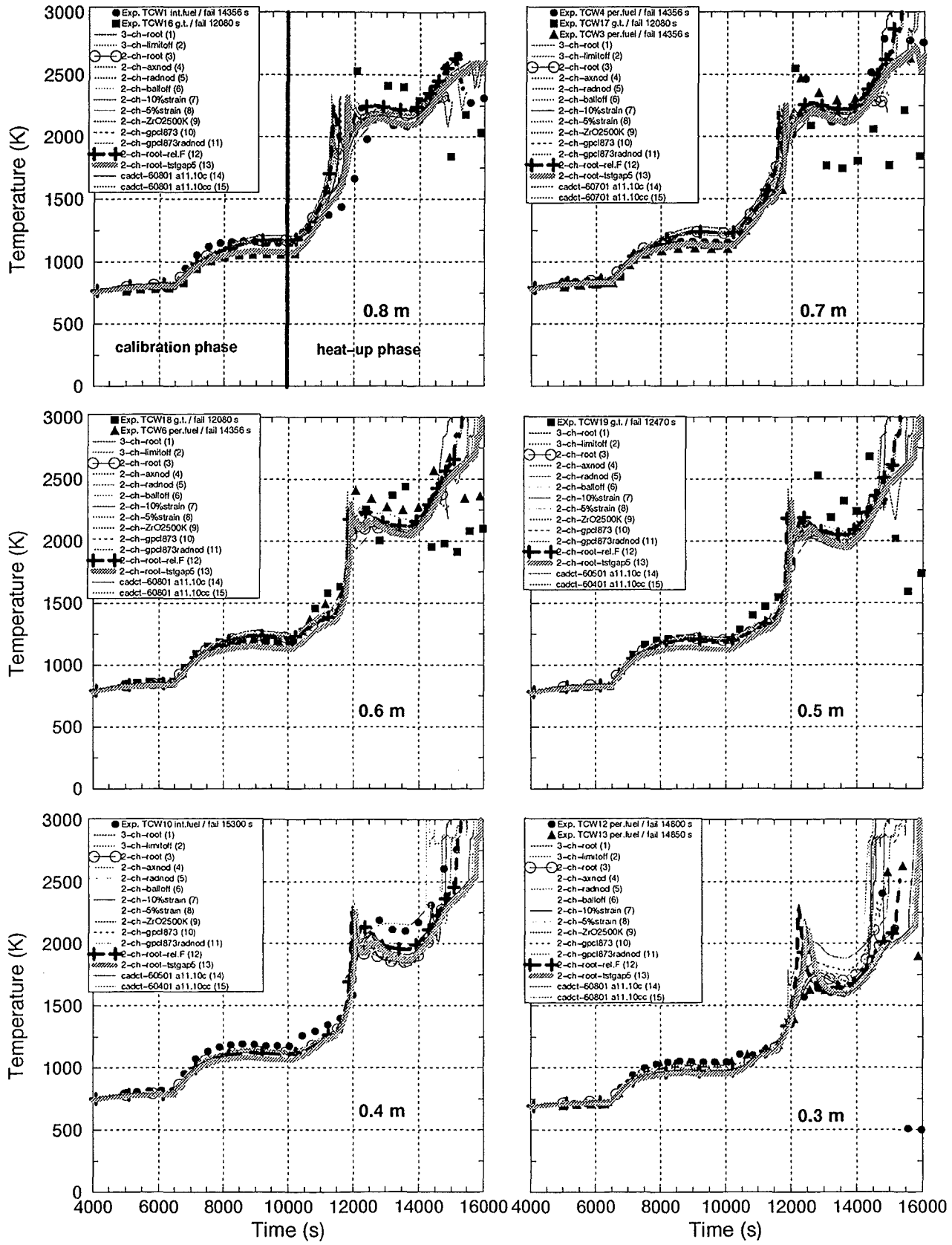

Figure 4.1 Fuel rod temperatures calculated at different elevations compared with corresponding experimental data

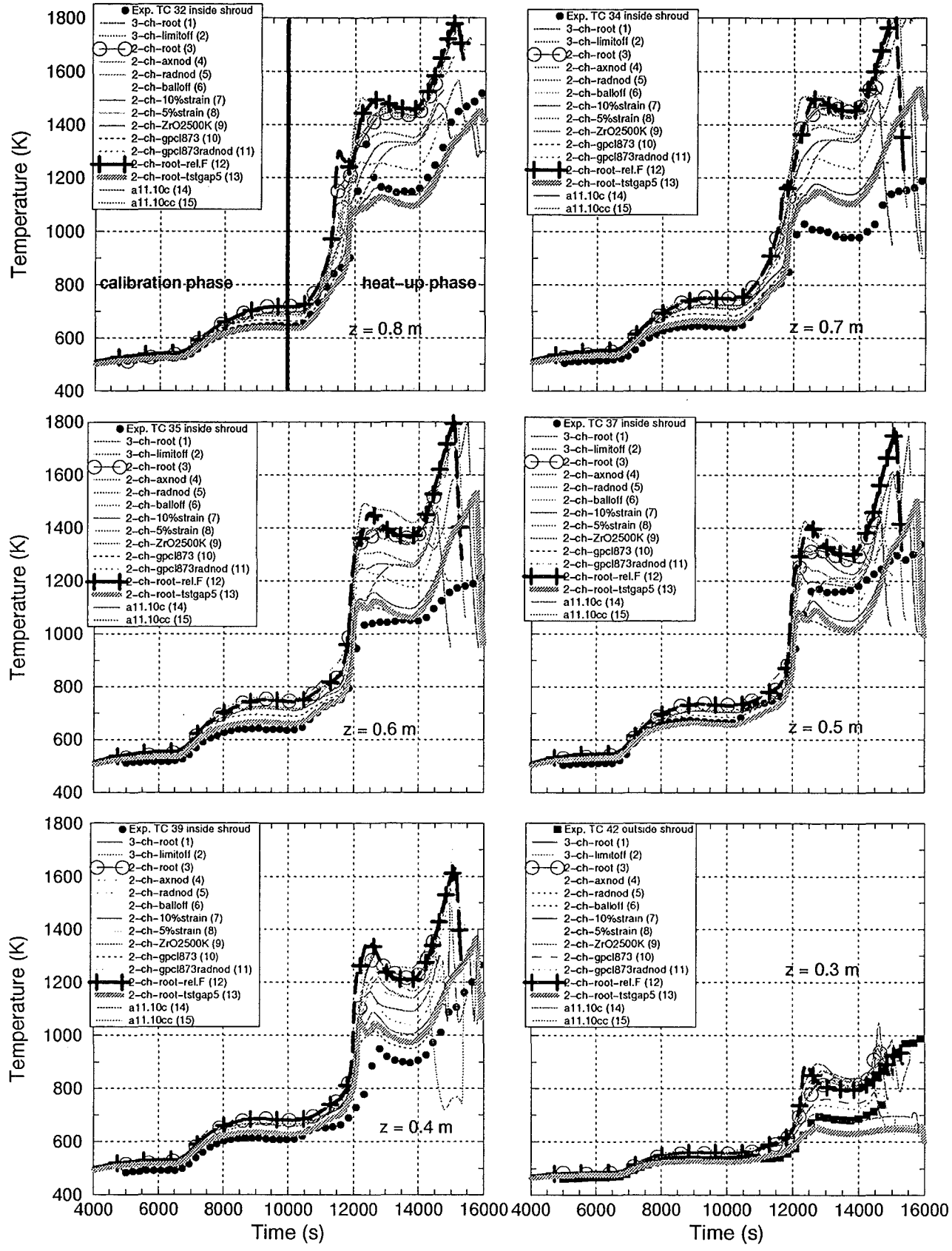

Figure 4.2 Shroud temperatures calculated at different elevations compared with the corresponding experimental data at the inner (0.4m to 0.8 m) and outer (0.3 m) shroud measuring positions

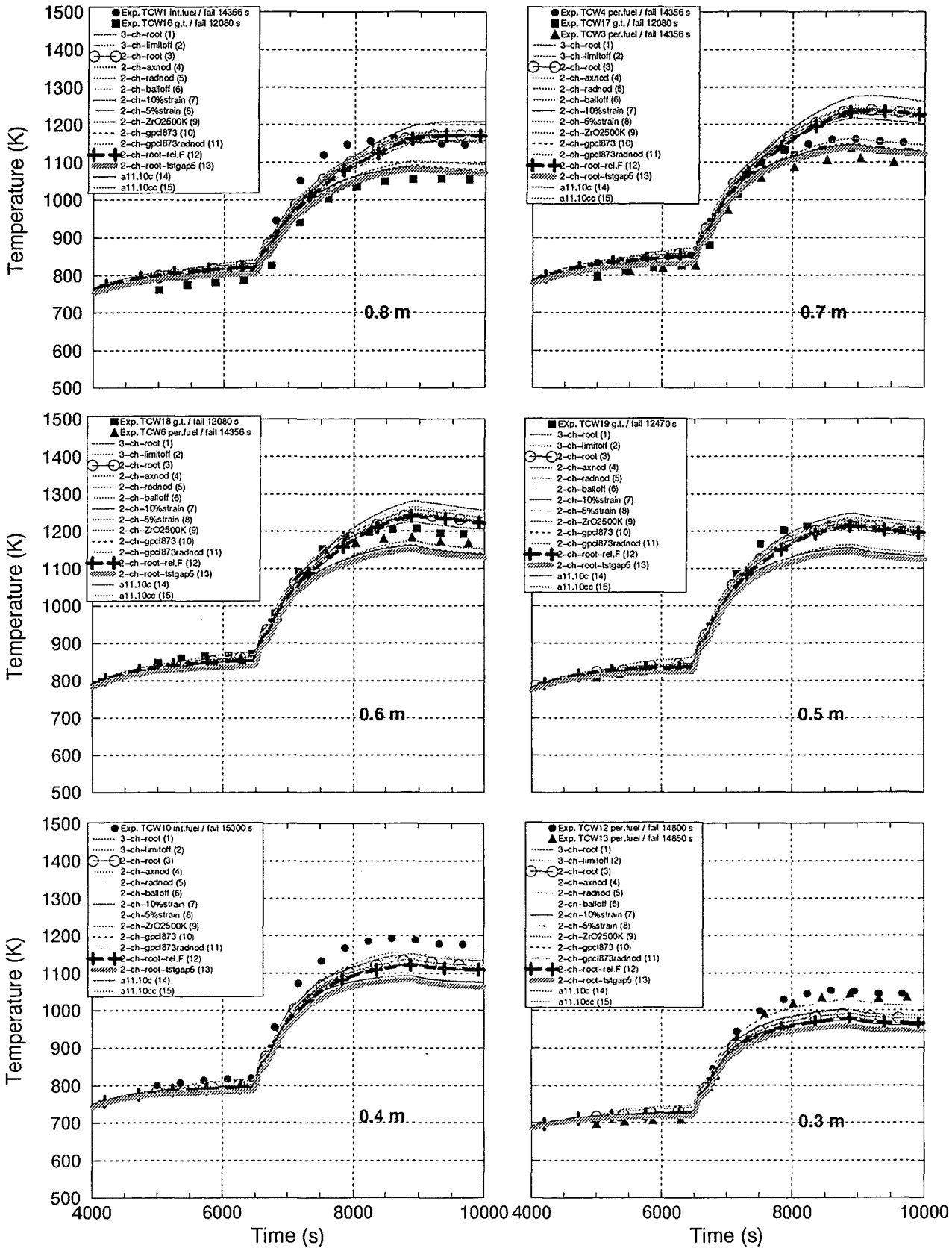

Figure 4.3 Comparison of measured and calculated fuel rod temperatures in the calibration phase of the experiment up to 10000 s

a

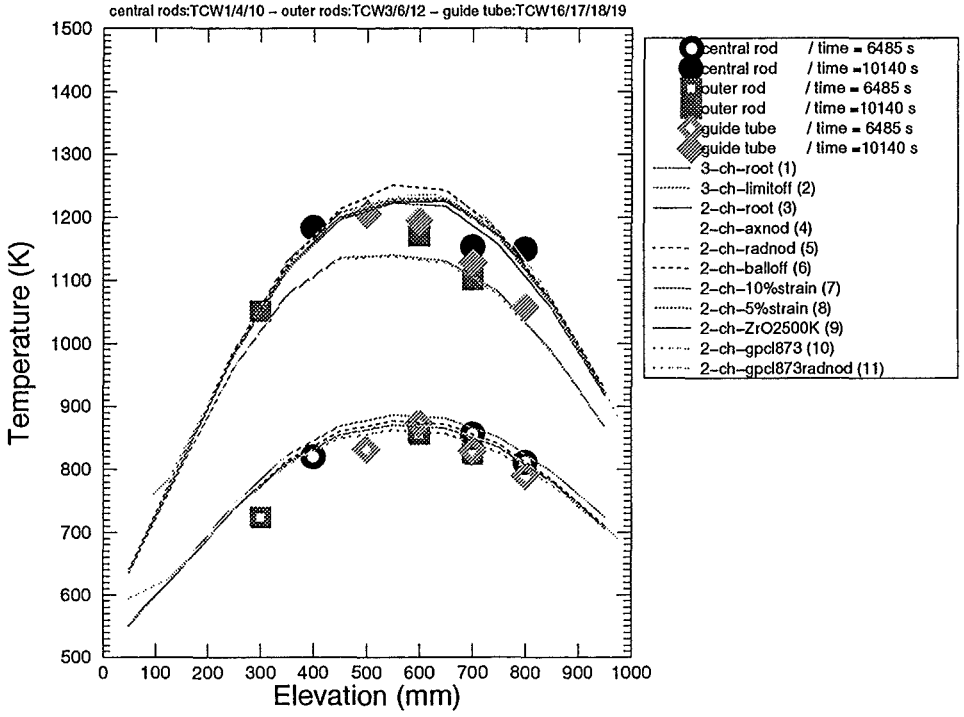

b

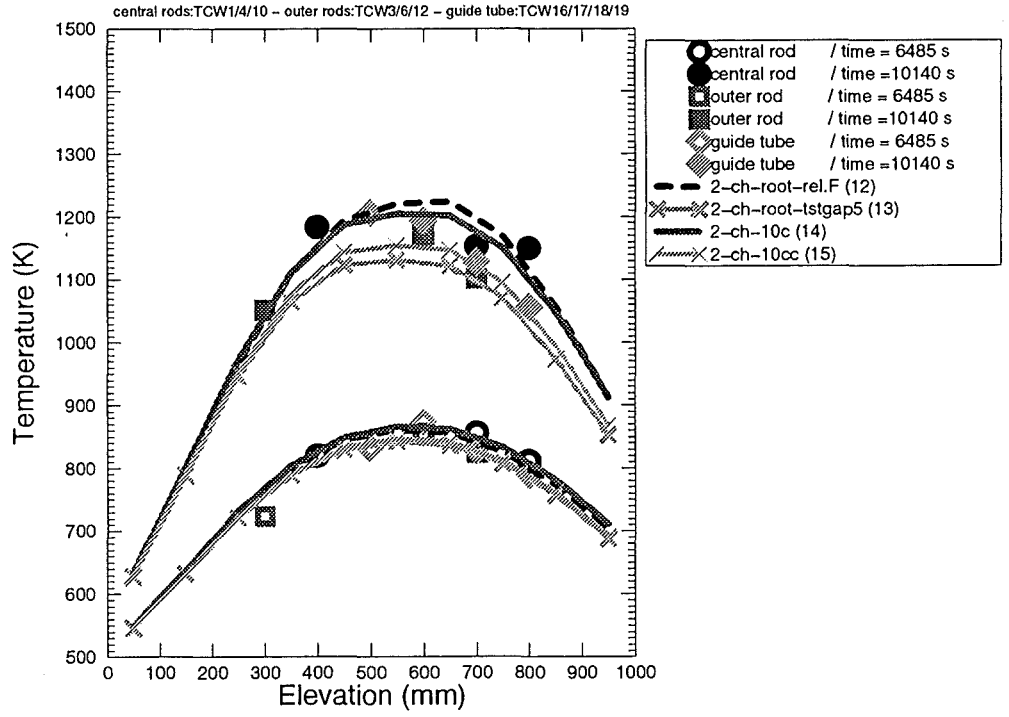

Figure 4.4 Axial temperature profiles in the bundle at 6485 s and 10140 s for cases (1) to (11) (4.4a) and cases (12) to (15) (4.4b)

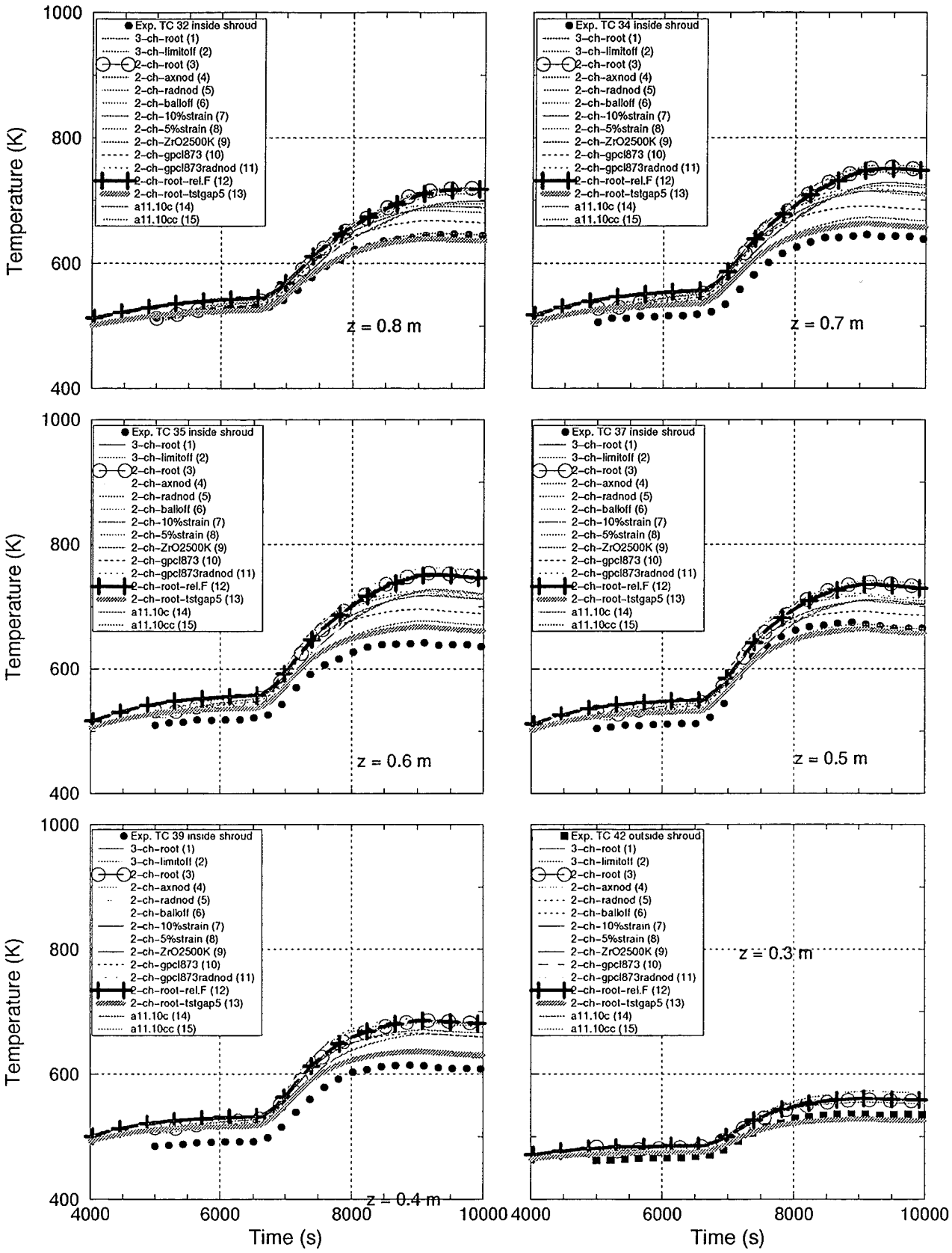

Figure 4.5 Comparison of measured and calculated shroud temperatures in the calibration phase up to 10000 s

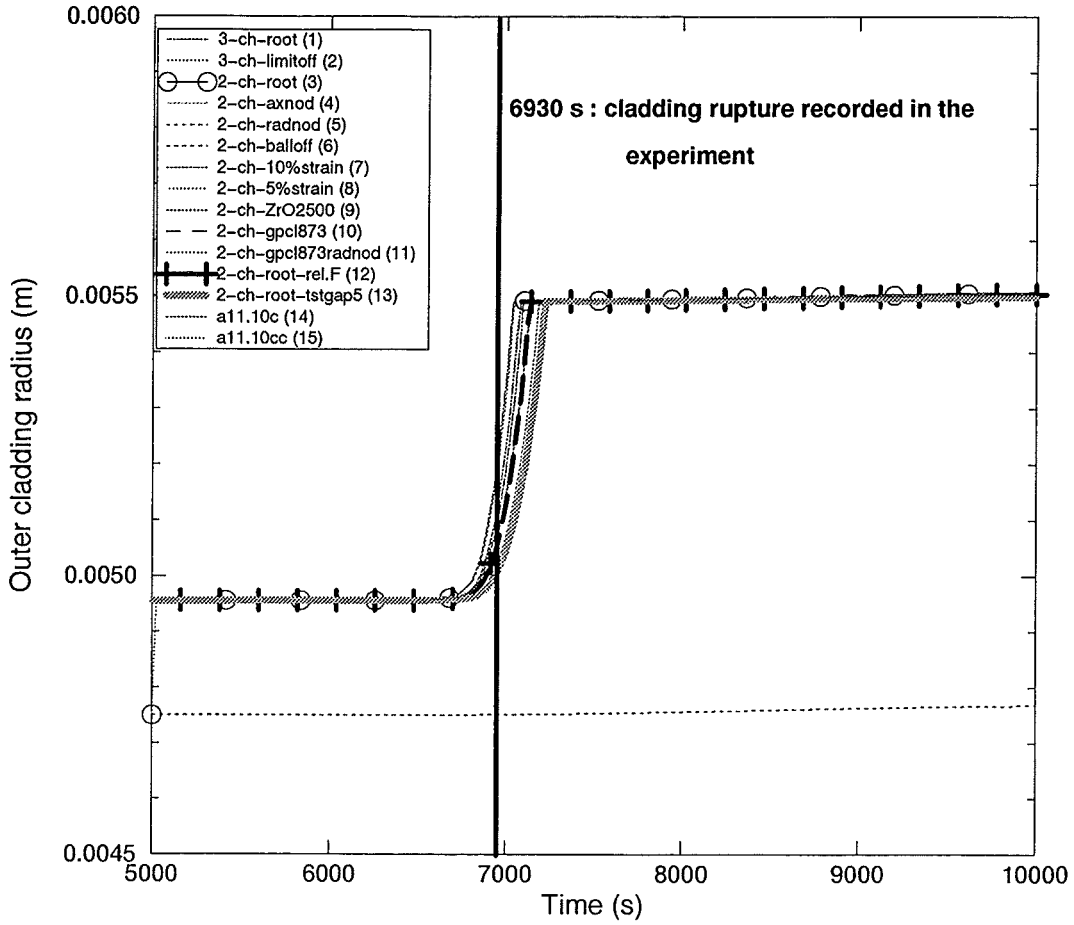

Figure 4.6 Change of cladding radii calculated in the bundle mid-plane up to cladding failure by overstrain

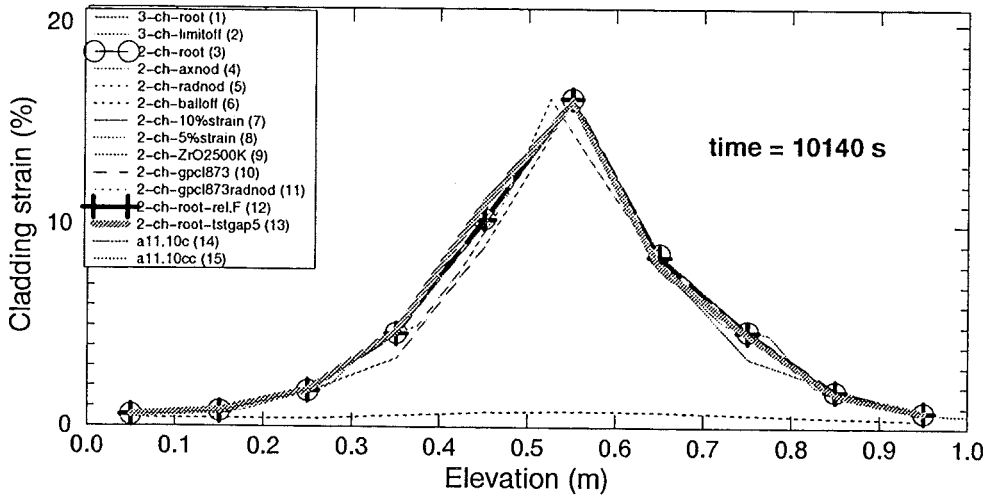

Figure 4.7 Axial profiles of cladding deformations calculated at the end of the calibration phase

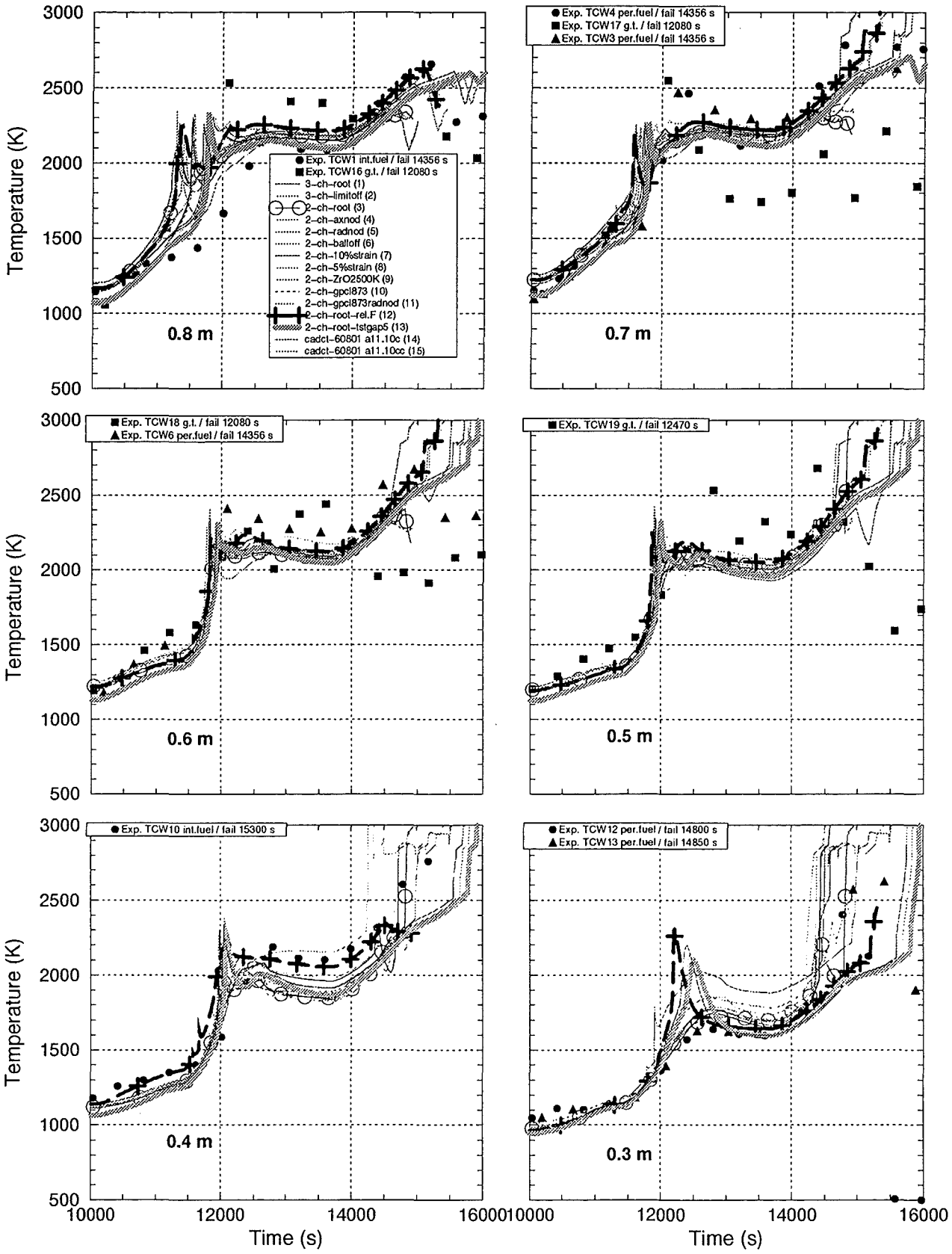

Figure 4.8 Comparison of measured and calculated fuel rod temperatures in the transient heat-up phase

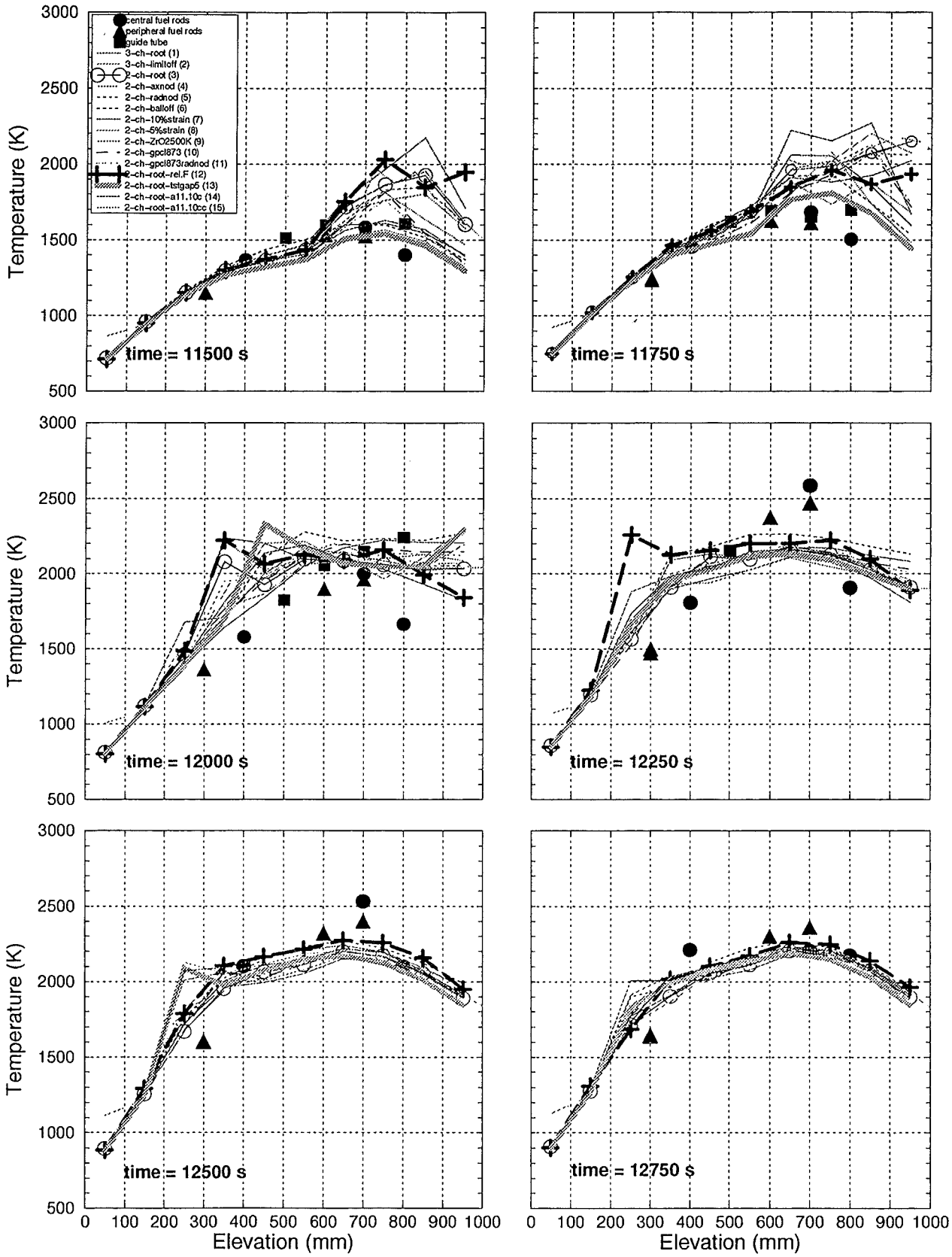

Figure 4.9 Comparison of measured and calculated axial temperature profiles of the fuel rods in the heat-up phase (experimental data are extended by guide tube temperatures)

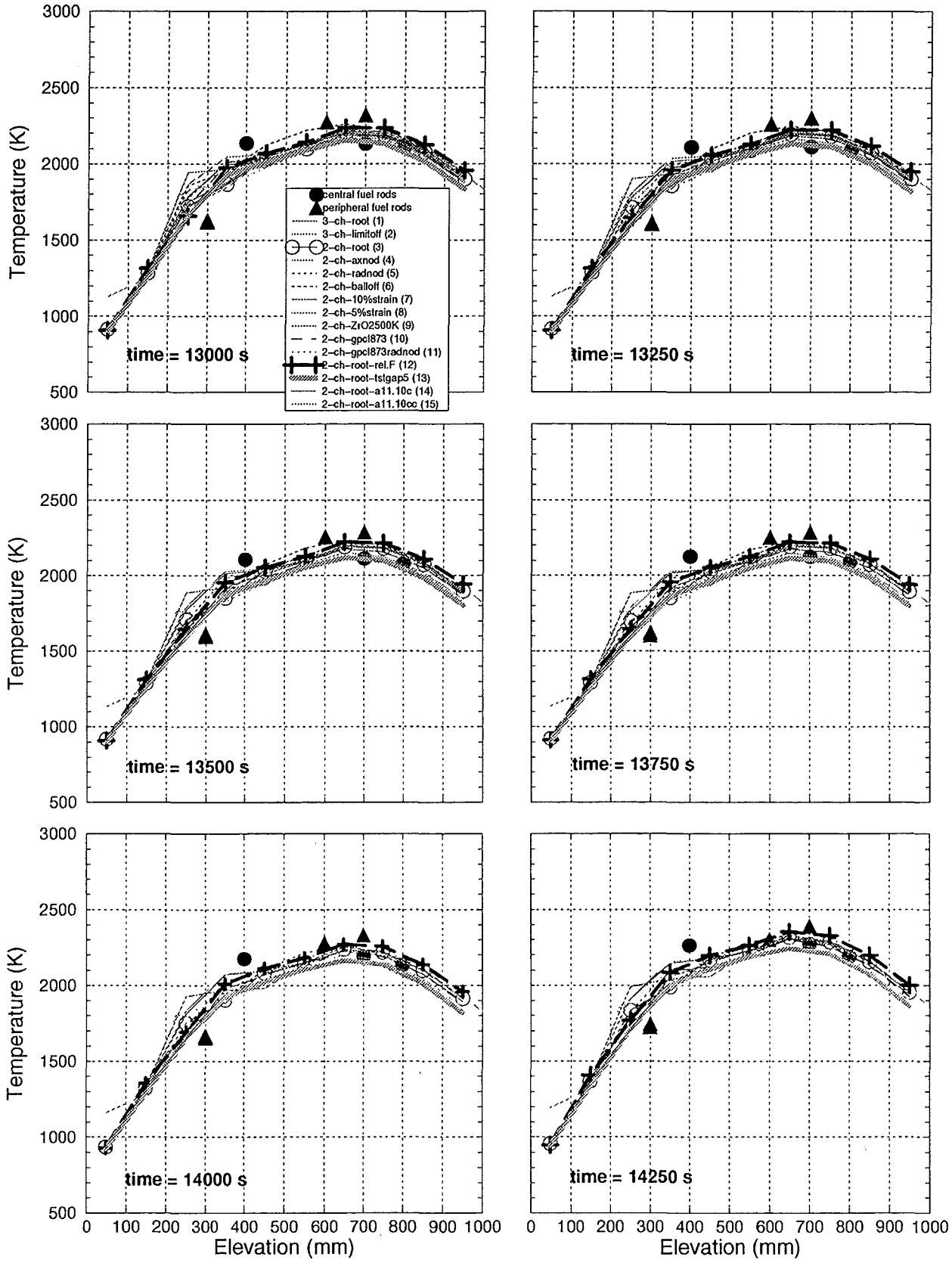

Figure 4.9 continued

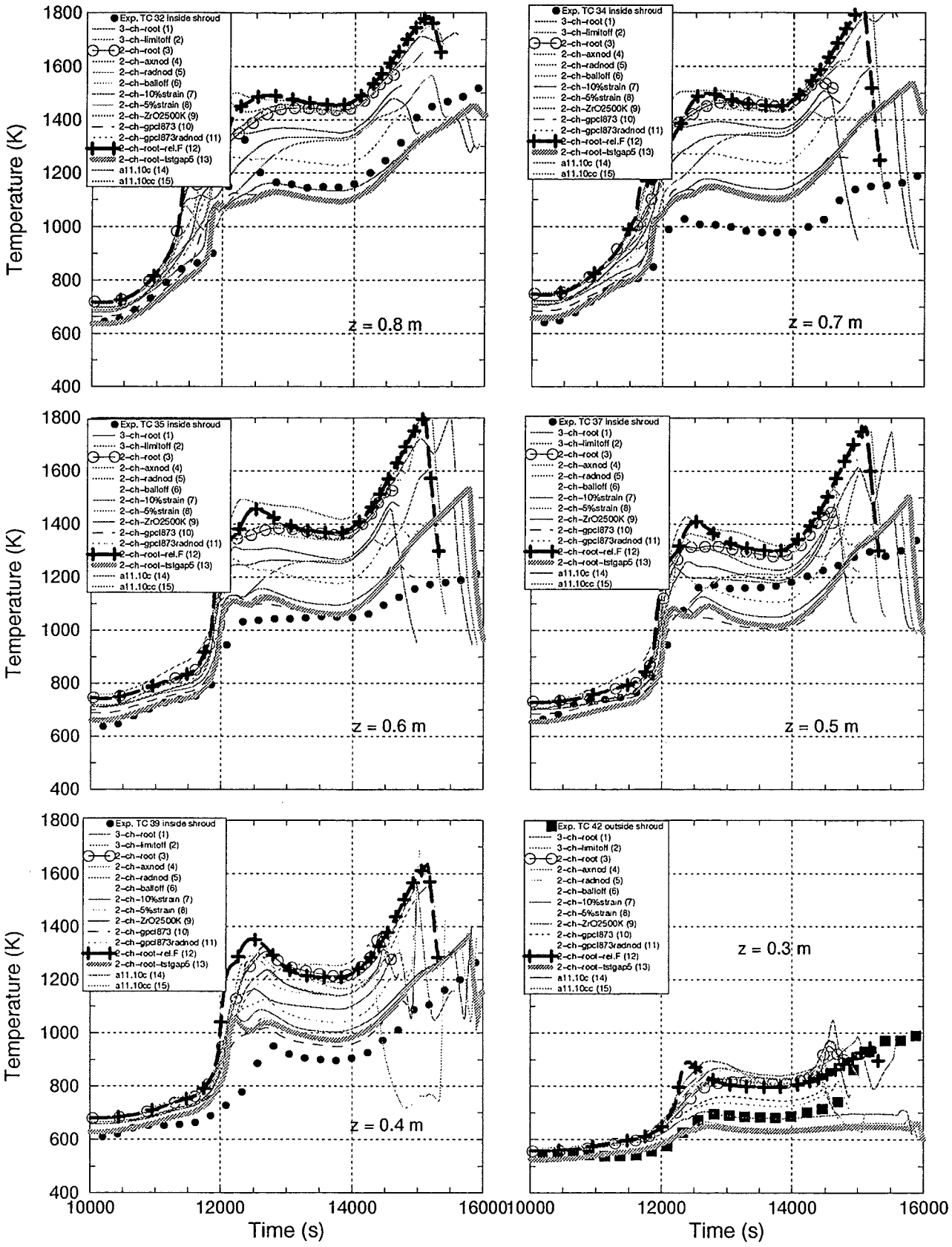

Figure 4.10 Comparison of measured and calculated shroud temperatures in the transient heat-up phase

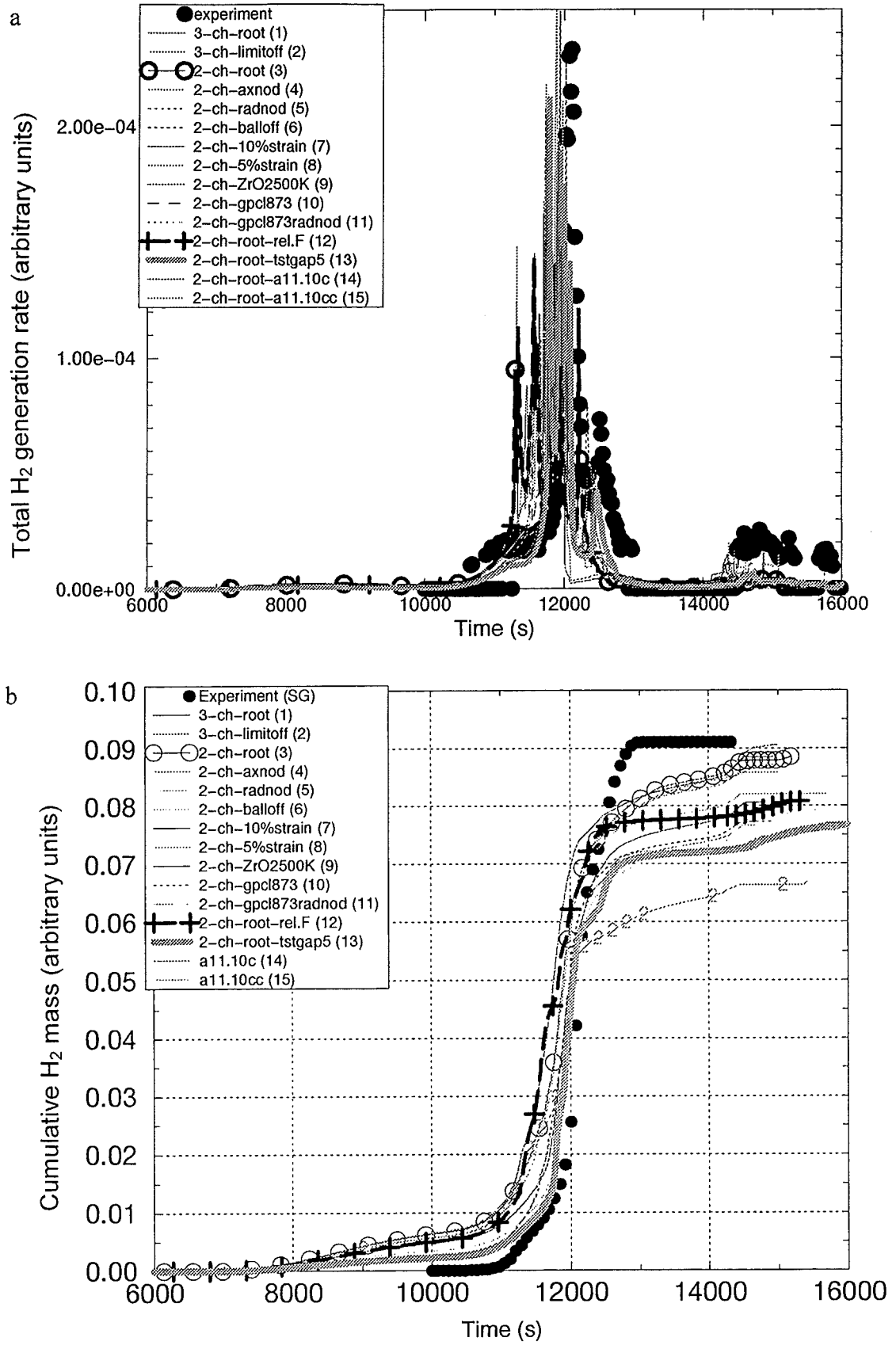

Figure 4.11 Hydrogen production rate (a) and cumulative hydrogen mass generated by Zircaloy oxidation (b)

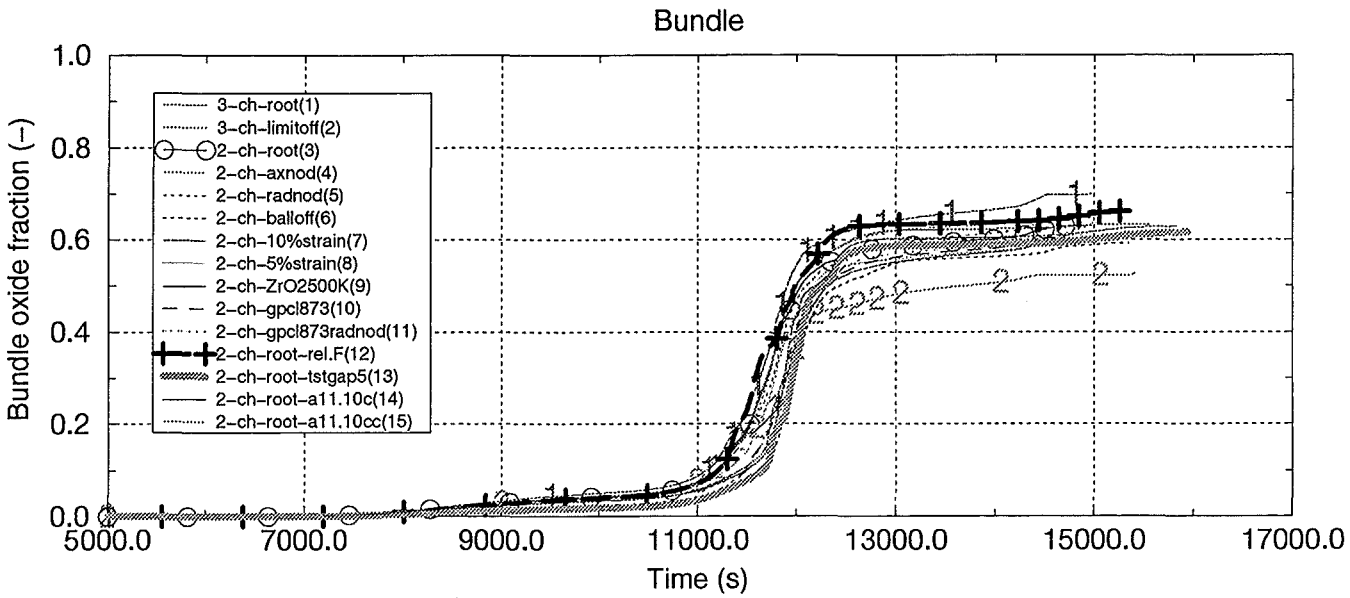

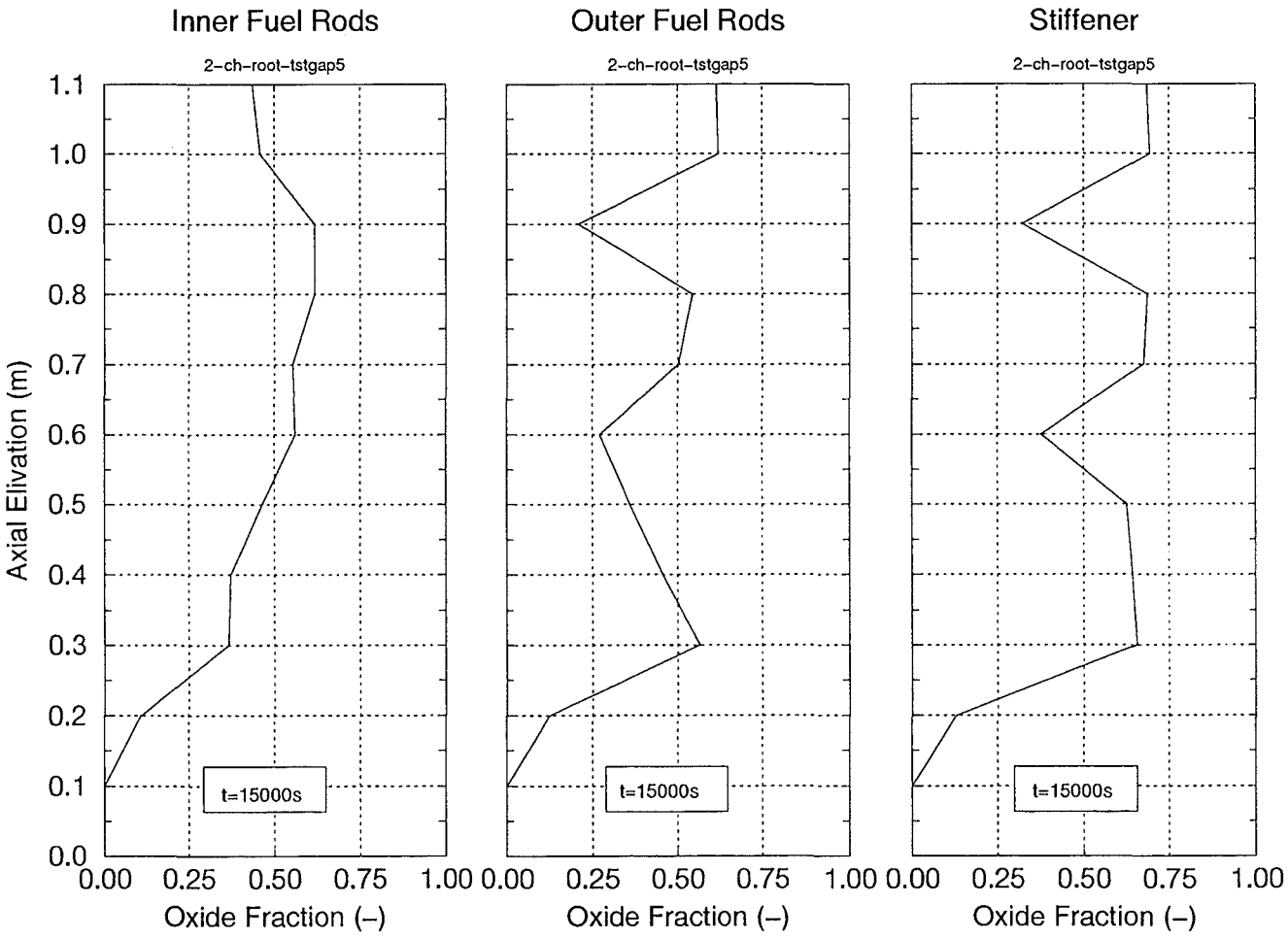

Figure 4.12 Fraction of the Zircaloy oxidized in the course of the experiment (a) and axial profiles of the Zircaloy oxidation status in the bundle at 15000s calculated for the case (13)

a

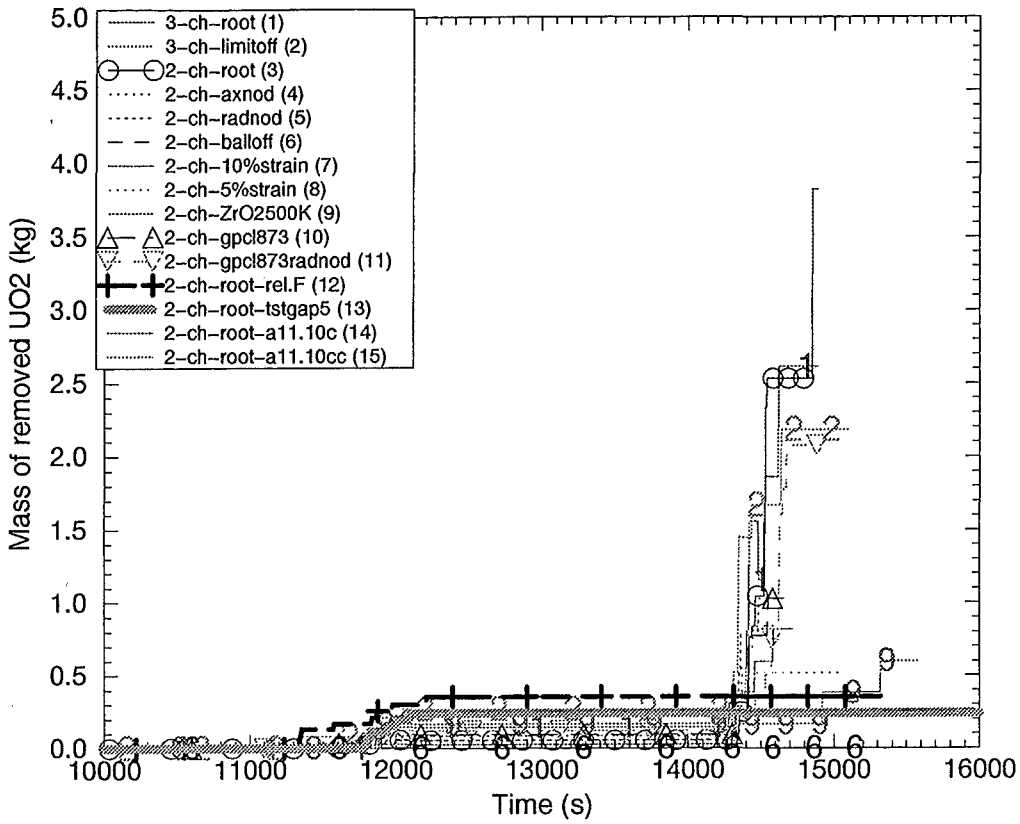

b

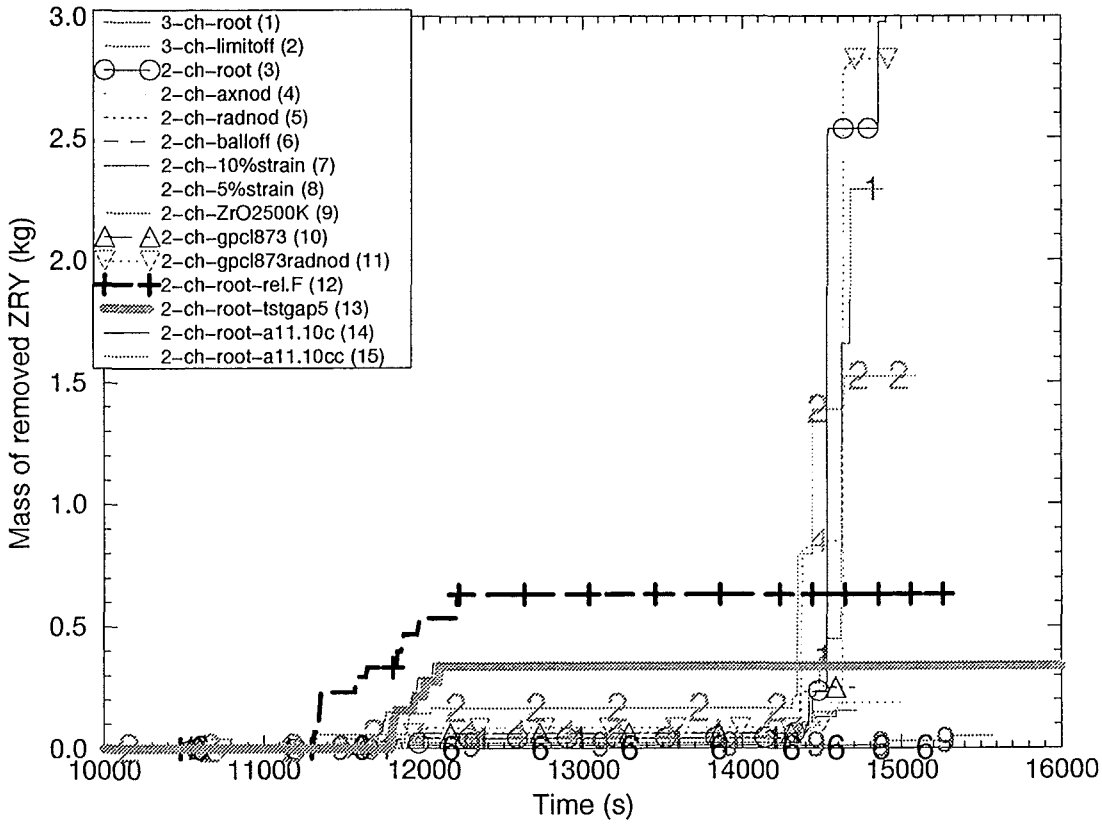

Figure 4.13 Evolution of fuel rod degradation process in terms of masses of liquefied and removed UO2 as the result of Zircaloy-UO2 chemical interaction (a) and in terms of liquid Zircaloy masses (b)

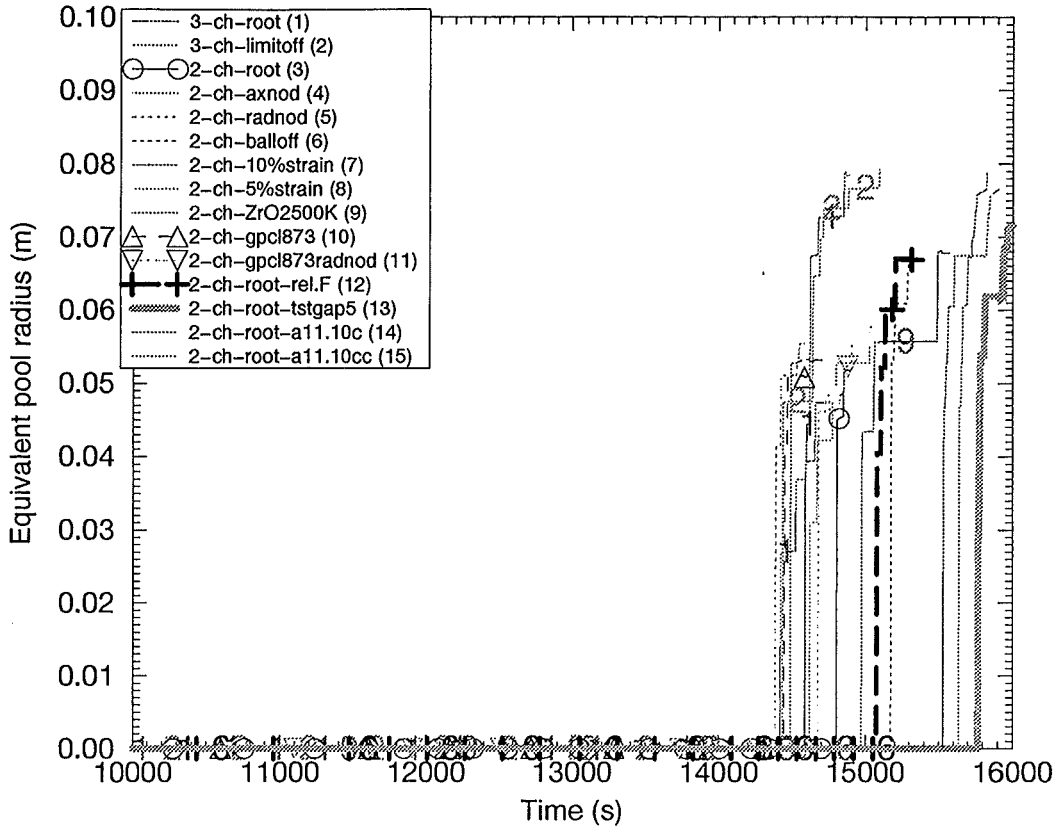

Figure 4.14 Calculated begin of molten pool formation in terms of the evolution of the equivalent molten pool radius (radius of an equivalent hemisphere containing the melt mass)

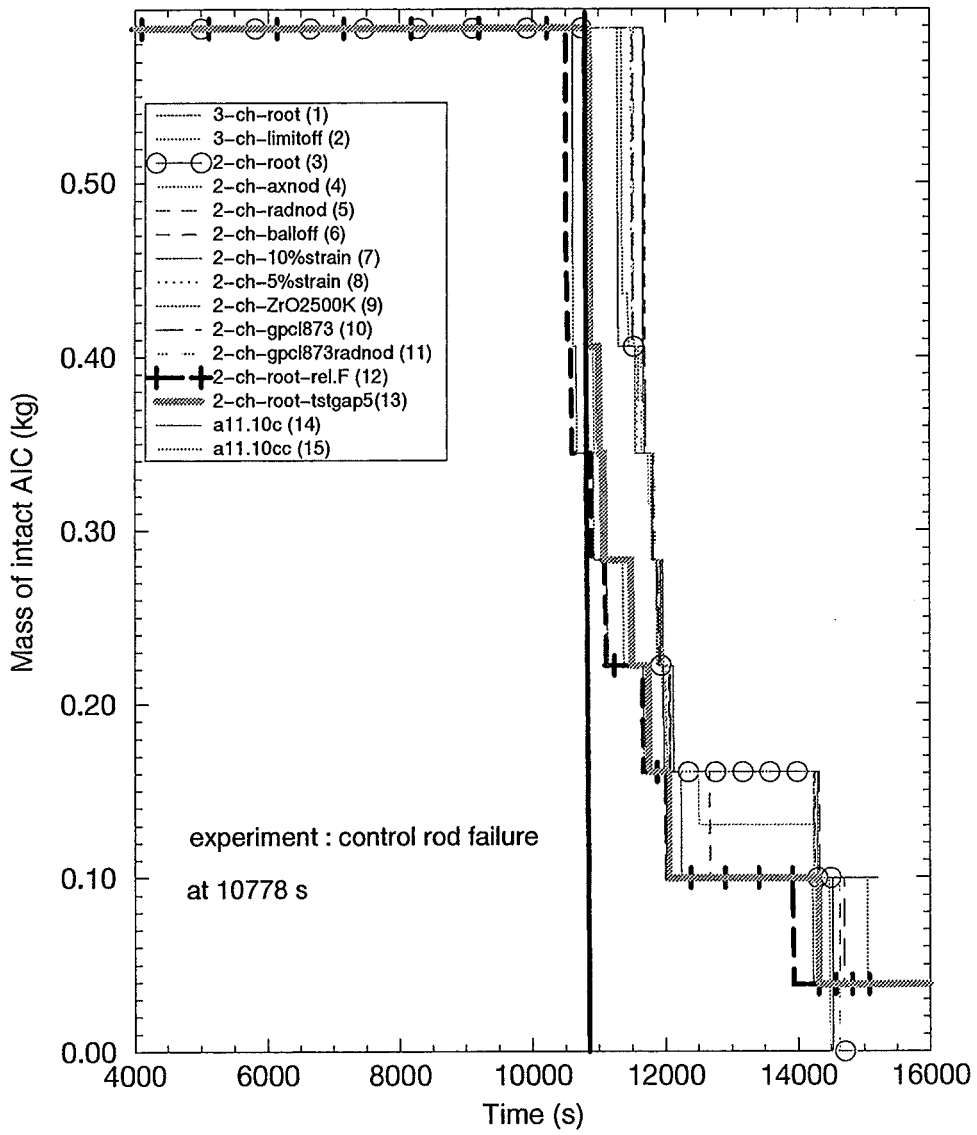

Figure 4.15 Evolution of the absorber rod degradation in terms of the residual (not yet removed) Ag-In-Cd mass

a

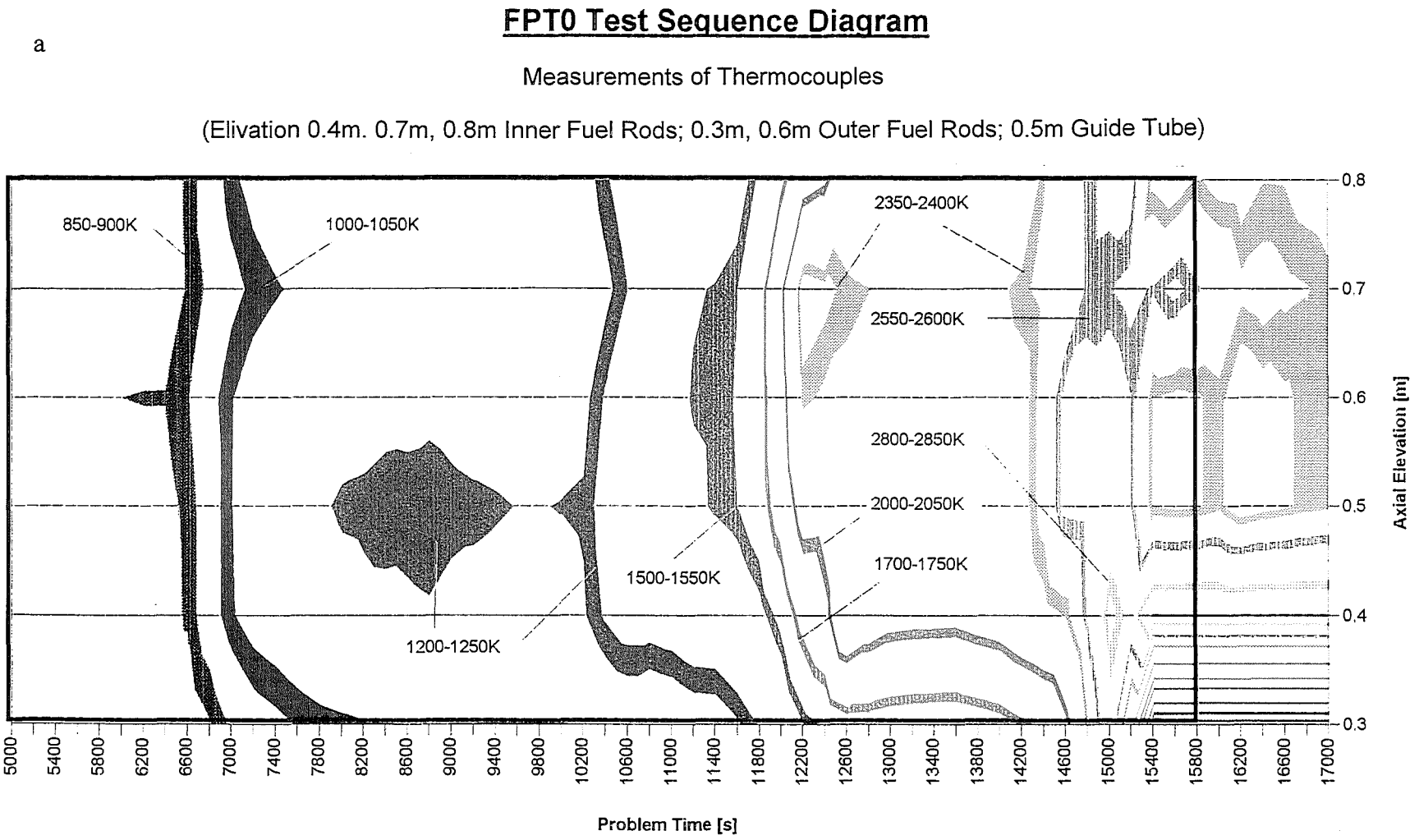

Figure 4.16 Evolution of the axial fuel rod temperatures vs. time for the experiment (a) and for case (13) (b)

b

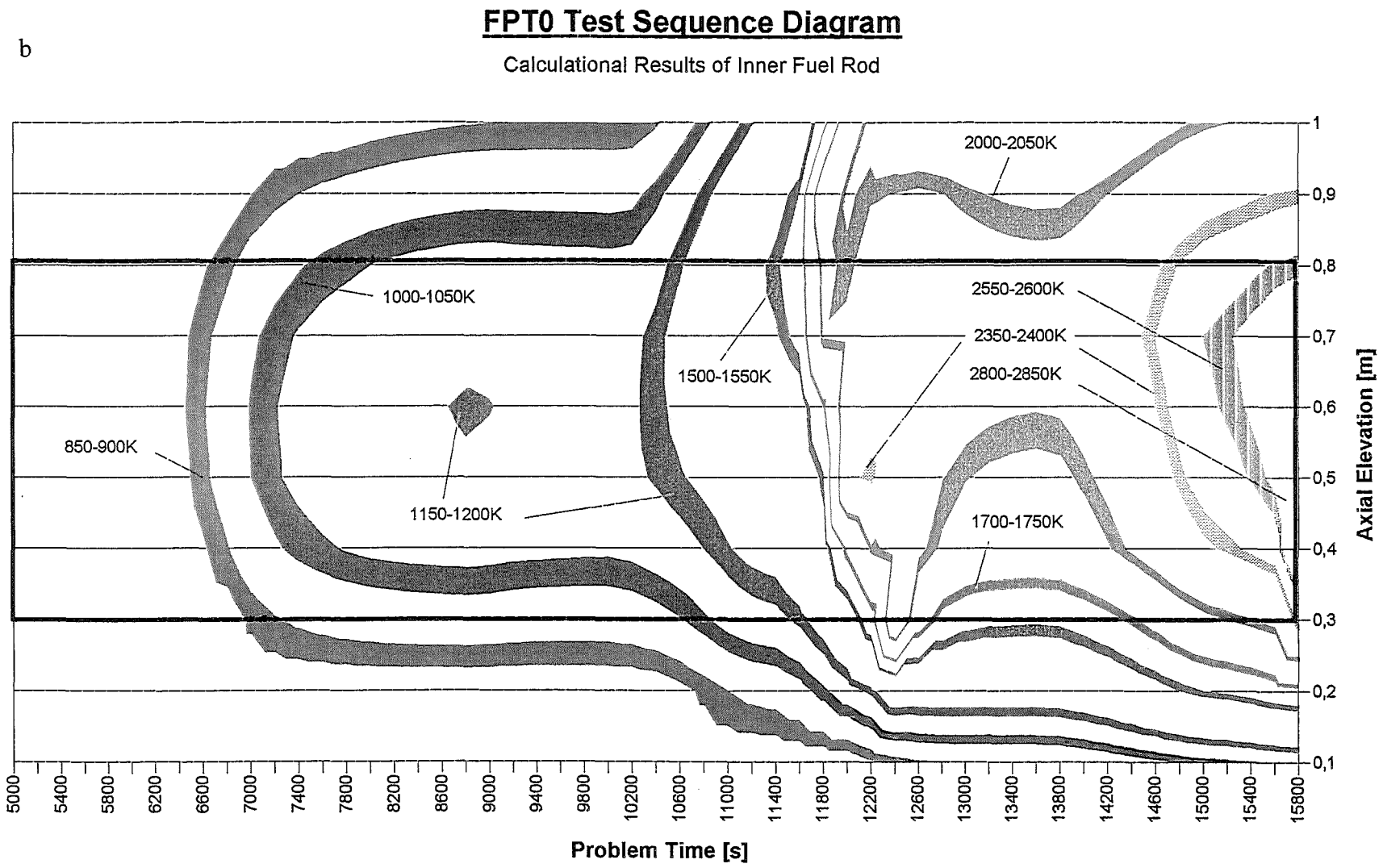

Figure 4.16 continued

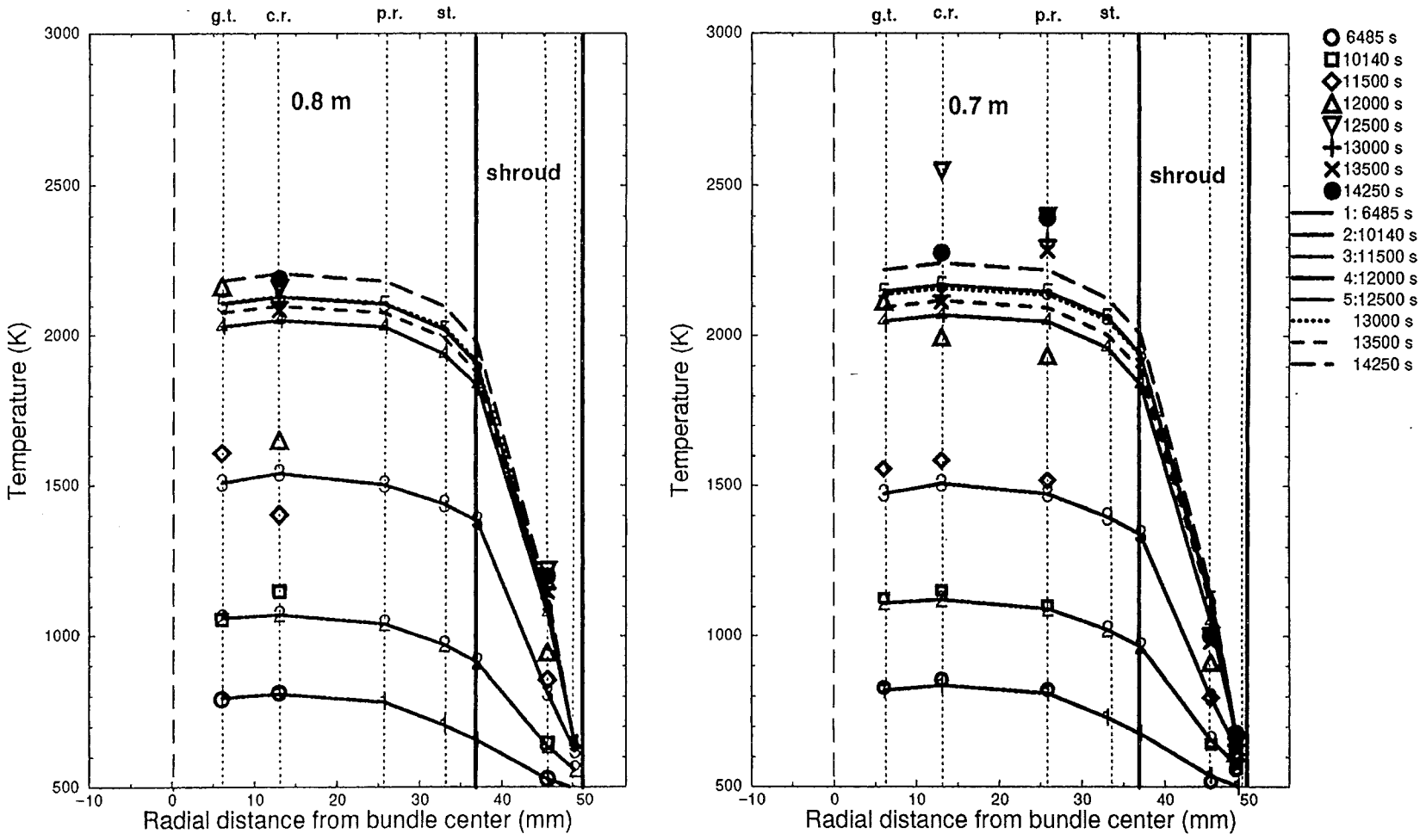

Figure 4.17 Evolution of radial temperature distribution across the FPT0 bundle and shroud for case (13)

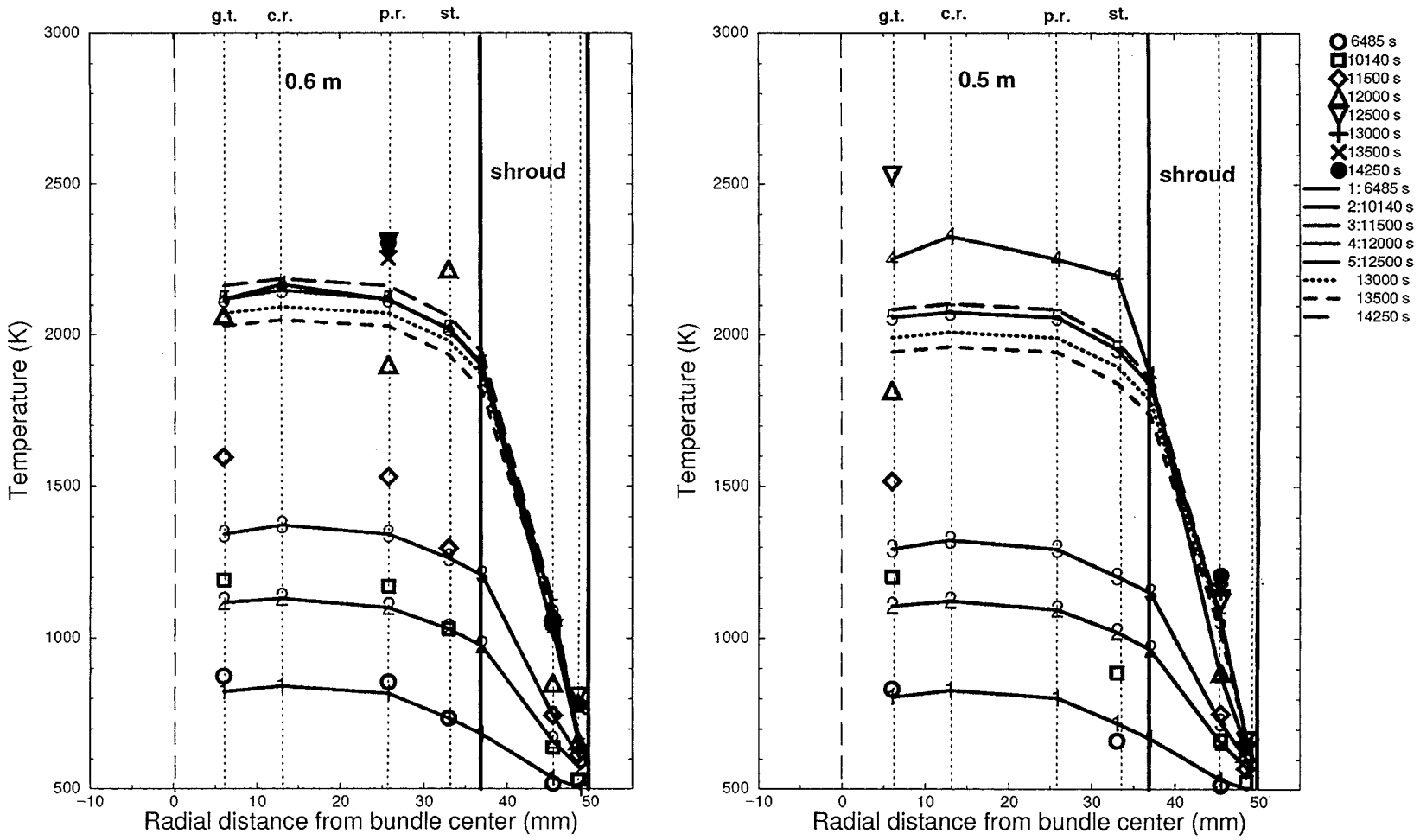

Figure 4.17 continued

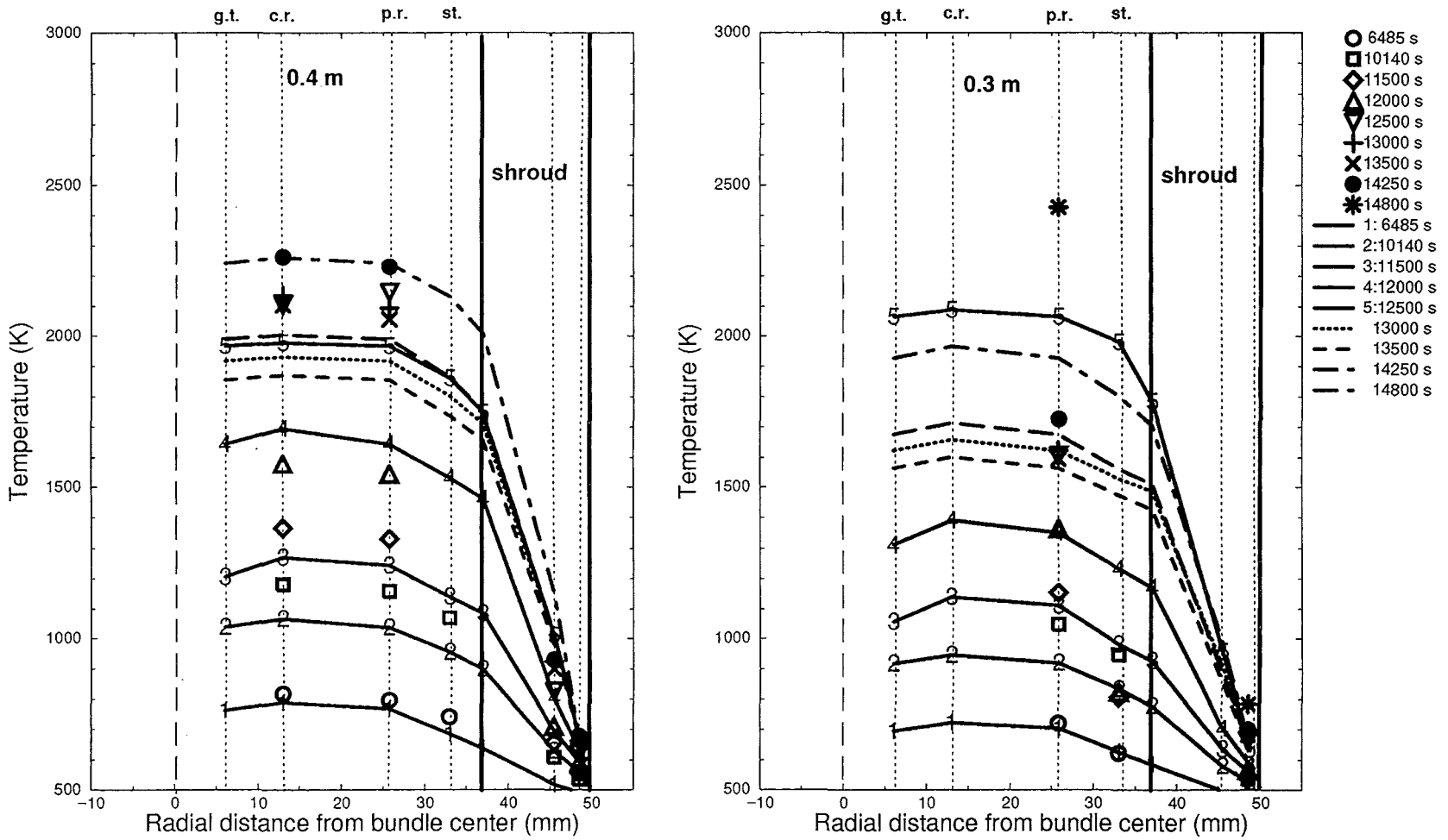

Figure 4.17 continued

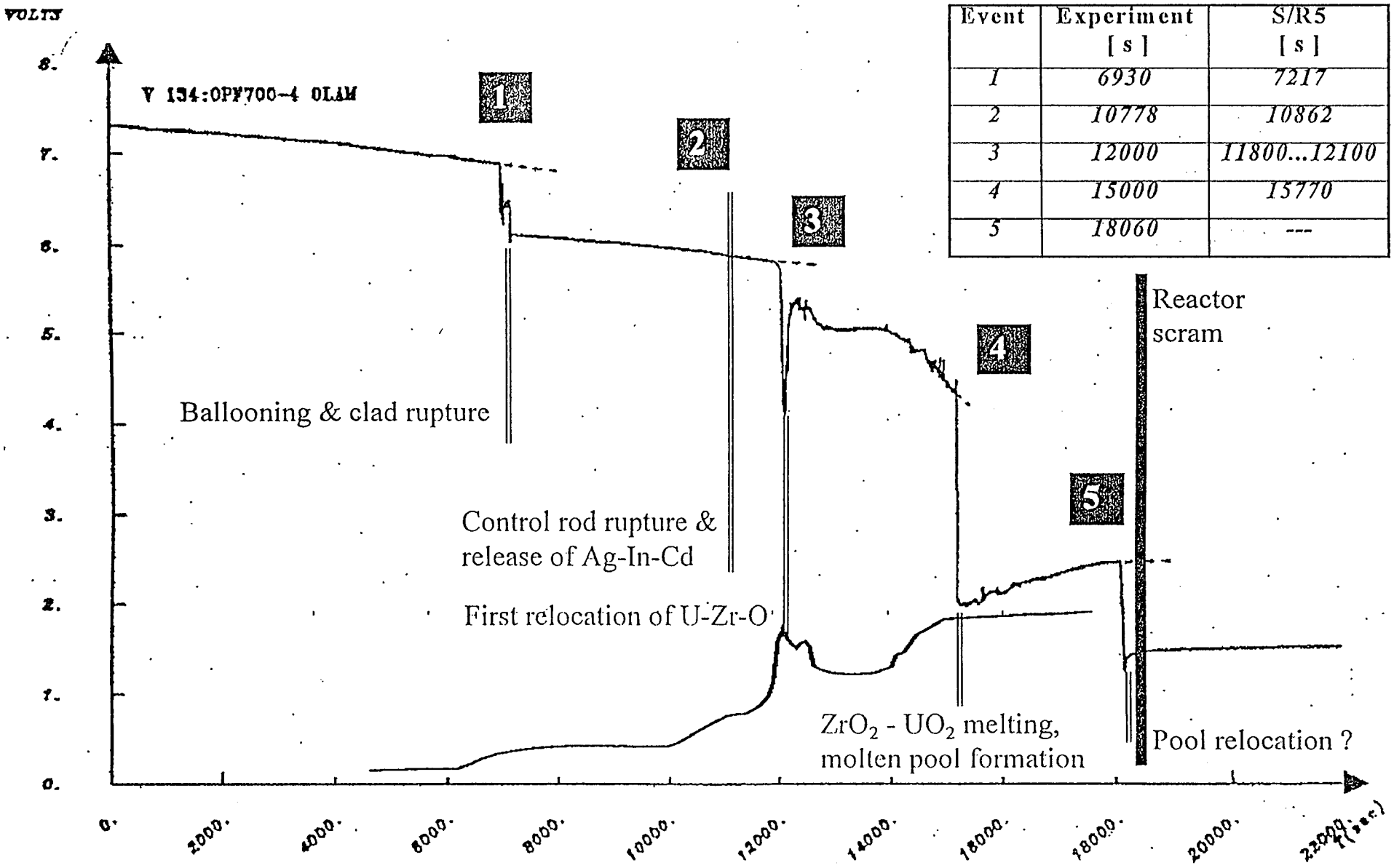

Event	Experiment [s]	S/R5 [s]
1	*6930*	*7217*
2	*10778*	*10862*
3	*12000*	*11800...12100*
4	*15000*	*15770*
5	*18060*	---

Figure 4.18 Sequence of bundle degradation events as measured compared with the corresponding events calculated for case (13)

5 SUMMARY AND CONCLUSION

Starting from a detailed FPT0 input model for the analysis with SCDAP/RELAP5 which includes three independent fluid channels interconnected with cross-flow junctions, we developed a simplified two-channel model for the realization of parameter studies with a fast-running computer model for FPT0. In total 12 calculations cover this first part of our investigation.

The variation of several parameters showed a qualitatively small scatter band of temperature evolution up to the beginning of the oxidation escalation. Only after the onset of oxidation effects of the parameters were relevant but only in details (for example the onset of molten pool formation is earlier or some times later). This indicates that new models or improvements of existing models are necessary to improve accurately calculated results considerably.

Investigations have shown that heat transport properties of the shroud (i.e. heat losses through the shroud) have a significant impact on the temperature history inside the bundle and thus on the sequence of individual bundle degradation processes. Since the standard shroud model in SCDAP/RELAP5 takes into account neither the changing gap widths due to thermal expansion of the shroud material layers nor radiation heat transfer through open gaps, a new shroud model has been developed which considers these effects. Further calculations (13) to (15) as a second part of this study cover the effects of this new shroud model.

With the new shroud model, the calculated bundle temperatures agree satisfactorily with the corresponding experimental data. Generally, the temperature levels both inside the bundle and in the shroud are higher in the calibration and early oxidation phase than observed in the experiment resulting in a significantly earlier begin of Zircaloy oxidation and thus in an earlier begin of hydrogen production than in the experiment.

Though the scatter band of calculated temperatures up to the early degradation phase is small, these temperature differences, due to the nonlinearities involved in the modeled physical processes, may lead to larger differences in the generated hydrogen and the amount of relocated material. Temperature level, Zircaloy oxidation, failure of oxidized cladding and release of liquefied Zr-U-O influence each other and thus lead to a broader scatter band in the calculated results for the later phases (after onset of oxidation) of the bundle degradation processes.

The uncertainties can be reduced by two means:

1. a more accurate temperature calculation in the bundle starting in the calibration phase
2. by a more physical model of the failure of oxidized cladding than offered by SCDAP/RELAP5

With this work part 1 has been successfully done, though there are still some improvements necessary. Part 2 of the necessary improvements needs still to be done.

Essential improvements of the calculational results (cases (13) to (15)) concerning the evolution of shroud temperatures and thus fuel rod temperatures result in a much better qualitative agreement with the experimental cumulative hydrogen mass, although there is still a quantitative difference between experiment and calculation of about 20 %. This indicates the necessity for a demand of further code assessment and improvement, especially for the oxidation model.

Nevertheless, the sequence of characteristic events in the course of the bundle degradation — cladding failure by overstrain, begin of control rod failure, begin of release of liquefied Zr-U-O masses, and molten pool formation onset — agrees well with the experimental observations. All calculations have been terminated with the begin of molten pool formation due to significant shortcomings in SCDAP/RELAP5 models for the subsequently following late phase. Therefore, no statements could be made about the subsequent events of the experiment.

In a next step the Phebus test FPT1 will be analyzed in a similar manner based on the experience presented here. In this work it is planned to go on with additional code improvements concerning the following items:

- hydrogen generation
- relocation of central fuel rods
- influence of irradiated fuel

6 REFERENCES

[1] P. von der Hardt, A. V. Jones, C. Lecomte, A. Tattegrain:
"Nuclear Safety Research: The Phebus FP Severe Accident Experimental Program",
Nucl. Safety 35(2), 1994

[2] N. Hanniet, S. Gaillot, B. Barthet, G. Repetto, G. Garnier:
"Phebus PF-FPT0-Preliminary Report",
IPSN Technical Note NT 9/94 (restricted distribution)

[3] P. von der Hardt, A. Tattegrain:
"Phebus Probes Core Meltdown Behviour: The First Results",
Nuclear Europe Worldscan 9-10, 1995

[4] P. Hofmann, S. Hagen, V. Noack, G. Schanz, L. Sepold:
"Chemical-Physical Behaviour of Light Water Reactor Core Components tested under Severe Reactor Accident Conditions in the CORA Facility",
Nuclear Technology 118, June 1997

[5] S. Hagen, P. Hofmann, V. Noack, G. Schanz, G. Schumacher, L. Sepold:
"Comparison of the Quench Experiments CORA-12, CORA-13, CORA-15",
FZKA 5679, 1996

[6] D.A. Petti et al.:
"Power Burst Facility (PBF) Severe Fuel Damage Test 1-4 Test Results Report",
NUREG/CR-5163, EGG-2542, 1989

[7] M.L. Carboneau, V.T. Berta, M.S. Modro:
"Experiment Analysis and Summary Report for OECD LOFT Project Fission Product Experiment LP-FP-2"
OECD LOFT-T-3806, 1989

[8] W. Hering, P. Hofmann:
"Material Interactions during Severe LWR Accidents. Summary of Separate-Effects Test Results",
KfK 5125, 1994

[9] G. Schanz, S. Hagen, P. Hofmann, G. Schumacher, L. Sepold:
"Information on the Evolution of Severe LWR Fuel Element Damage obtained in the CORA Program",
J. Nucl. Materials 188, 1992

[10] R.R. Hobbins, D.A. Petti, D.J. Osetek, D.L. Hagrman:
"Review of Expeirmental Results on Light Water Reactor Core Melt Progression",
Nucl. Technology 95, 1991

[11] I. Shephard (editor):
"The Ability of Codes to Predict Core Behaviour in FPT0", (unpublished note)

[12] C.M. Allison et.al.:
"SCDAP/RELAP5 mod 3.1 Code Manual, Vol. I-IV",
NUREG/CR-6150, EGG-2720, 1993

[13] H. Scheurer:
"Data Book Phebus FPT0",
Phebus FP Document IS 92.48 (restricted distribution)

[14] W. Krischer:
"Minutes of the second meeting of the bundle degradation interpretation circle",
JRC European Commission Safety Technology Institute, Phebus FP-SAWG95-018/1, May 1995
(restricted distribution)

[15] M. Vandegehuchte, I. Shepherd:
"Post-test calculations for core degradation behaviour in Phebus Test FPT0 using ICARE2 V1",
JRC technical note to be issued 1996 (restricted distribution)

[16] S. Hagen, HIT/FZK:
private communication

[17] G. Repetto:
"Analyses quantitatives des tomographies du dispositif FPT0",
Note Technique LERES No. 36/95, 1995 (restricted distribution)

[18] R. Hobbins, D. Osetek, L. Louie:
"Phebus FPT-0 Synthesis Report",
PH-PF RC/96/08, 1996 (restricted distribution)

[19] A. Porracchia, R. Gonzales, P. Chatelard:
"ICARE: A Computer Code for Severe Fuel Damage Analysis - Models and Validation",
CSARP Meeting, Bethseda (MD), USA, May 1991

[20] V.F. Urbanic, T.R. Heidrick:
"High temperature oxidation of Zircaloy-2 and Zircaloy-4 in steam",
Journal of Nuclear Materials 75 (1978), pp 251-261

[21] R.E. Pawel, R.A. Perkins, R.A. McKee, J.V. Cathcard, G.J. Yurek, R.E. Druschel:
"Diffusion of oxygen in beta -Zircaloy and the high temperature Zircaloy-steam reaction",
Zirconium in the Nuclear Industry, ASTM STP 663 (1977)

[22] G. Bandini, ENEA Bologna:
private communication

[23] P.Hofmann, S. Hagen:
"Physical and chemical behaviour of LWR fuel elements up to very high temperatures",
KfK report No. 4104 (June 1987)

[24] W. Hering, C. Messainguiral:
"Ĭmprovement of the SCDAP/RELAP5 with respect to the FZK QUENCH facility",
FZK report to be published 1998

7 APPENDIX

7.1 FPT0 test conduct and characteristic events

Calibration Phase			
	bundle power	steam mass flow rate	events observed
Plateau 1	0 - 600 s: 0.75 - 0.85 kW 600 - 745 s: 0.85 - 2.05 kW 745 - 1275 s 2.05 - 1.44 kW 1275 - 3445 s: 1.44 kW const.	0 - 560 s: 0.0 g/s 560 - 600 s: 0.0 - 2.0 g/s 600 – 3445 s: 2.0 g/s const.	max. fuel rod temp. 733 K
Plateau 2	3445 - 6485 s: 1.44 kW const.	3445 – 3500 s: 2.0 - 0.5 g/s 3500 – 6485 s: 0.5 g/s const.	max. fuel rod temperature 873 K
Plateau 3	6485 - 6800 s: 1.44 - 3.70 kW 6800 - 8850 s: 3.70 kW const. 8850 - 9000 s: 3.70 - 3.42 kW 9000 - 10140 s: 3.42 - 3.50 kW	6485 – 10140 s: 0.5 g/s const.	6930 s: cladding rupture max. fuel rod temperature 1173 K
Transient heat-up phase			
	bundle power	steam mass flow rate	events observed
Control rod failure and Zircaloy oxidation phase	- 11090 s: increase to 11.23 kW -11400 s: 11.23 kW const. - 12020 s: increase to 20.60 kW - 12410 s: increase to 24.22 kW - 13000 s: 24.22 kW const.	- 11080 s: increase to 3 g/s - 13000 s: 3 g/s const.	10960 s: first indication of control rod failure 11920 S: second strong indication of control rod degradation 12000 - 12470 s: oxidation escalation 400 mm T_{max} = 2342 K 600 mm T_{max} = 2546 K 700 mm T_{max} = 2521 K 70% of Zircaloy inventory oxidized, about 90 g H2 produced

Table 7.1 Summary of the FPT0 test conduct and characteristic events of bundle degradation observed

Transient heat-up phase			
	bundle power	steam mass flow rate	events observed
Control rod failure and Zircaloy oxidation phase			Post irradiation examination of bundle materials microstructures indicates liquefaction of fuel in the upper part of the bundle relocation of Zr-U-O melt uncertain
Melt relocation and bundle collapsing phase	- 13680 s: 24.22 kW const.	- 14180 s: 3 g/s const.	second period of hydrogen production
	- 14830 s: increase to 35.25 kW	- 14720 s: decrease to 2.5 g/s	thermocouples inside the bundle fail at temperatures of 2200 - 2500 K
	- 15170 s: 32.25 kW const.	- 15 170 s: decrease to 2.3 g/s	significant temperature rise at 200 and 300 mm inside shroud. On-Line Aerosol Monitor indicates material relocation towards lower spacer grid beginning at about 15000 s (collapse of inner ring of fuel rods?)
Bundle degradation and molten pool formation phase	- 15850 s: increase to 39.50 kW - 17925 s: increase to 45.90 kW - 18100 s: increase to 47.85 kW - 18140 s: increase to 50.40 kW reactor scram	- 15350 s: decrease to 2.2 g/s - 16120 s: decrease to 1.5 g/s - 18140 s: 1.5 g/s const.	up to the end of the experiment a molten pool forms at the 200-300 mm elevation at about 18000 s power increase in the driver core probably due to axial pool expansion as a consequence of vaporisation of control rod material in the lowest part of the bundle. OLAM measures aerosol release PIE and PIA show uniform ceramic melt pool: 60 wt%U, 20 wt% Zr, 20 wt% O

Table 7.1 continued

7.2 A new shroud gap model for SCDAP/RELAP5

The Phebus-Databook [13] provides most of the data for ZrO_2 and Thoria with considerable margins of uncertainty. However there is an additional problem left: the modeling of the shroud gaps (radiation heat transport through open gaps and changing gap widths due to thermal expansion). These phenomena had to be included artificially into an effective thermal conductivity of the gap material (gas/steam) by modification of the input table for SCDAP/RELAP5. With the new shroud gap model the precision of effective thermal conductivities for the gap materials by user input (adding the effects of radiation heat transfer and gap closure) is not necessary any longer because it provides an integrated radiation heat transfer and a gap closure simulation.

7.2.1 Theory

At the moment SCDAP/RELAP5 uses only transparent and non-absorbing gases as gap material. SCDAP/RELAP5 also neglects the radiation heat transfer through shroud gaps. Now the radiation heat transfer is modeled by the code using an additive correction factor for the thermal conductivity of the gap material. Here the radiation heat transfer is calculated from the boundary temperatures of the gap and then transformed into a factor that increases the thermal conductivity of the gap.

Up to now in SCDAP/RELAP5 the shroud is modeled by a fixed axial and radial mesh. To handle a variable gap size using a moving mesh would be very difficult and time consuming. Thus, we decided to simulate the gap deformation by adjusting the thermal conductivity of the gap using a correction factor. This correction factor is derived from the relation of actual gap width and initial gap width retaining the original mesh.

Thus, the task is to model the real heat transfer $\dot{q}_R$ considering radiative heat transport and heat conduction through changing gap widths without change of the computational mesh in the shroud. As a first approximation, the effect of changing gap widths onto the effective heat capacity has not been considered because of its negligible influence on the overall heat capacity of the shroud (i.e. assuming very small gaps in comparison to the shroud thickness and very low heat capacities of the gap gases). Furtheron we assume that the shroud is modeled in rectilinear (Cartesian) geometry as done in SCDAP/RELAP5.

Figure 7.1 shows a scheme of a shroud consisting of two gaps as modeled in SCDAP/RELAP5 with fixed geometry compared with the more real shroud behaviour indicated by axially varying radii of the individual shroud material layers due to thermal expansion. In Figure 7.2, a decreased gap width s_0 is compared with the corresponding standard SCDAP/RELAP5 shroud model considering a fixed gap width s_M.

We assume a linear temperature profile across the whole gap where the boundary temperatures T_{in} and T_{out} are equal to those of the experiment due to equal heat transfer. That means that this derivation is valid only for slab geometry. This again leads to an averaged thermal conductivity across the gap dependent only on an averaged temperature across the gap.

The transformation of thermal expansion effects and radiation heat transfer into thermal conductivity leads to the introduction of an additive thermal conductivity correction factor $\lambda_{cor,i}$ which has to be added to all other thermal conductivity coefficients $\lambda_{M,i}$. The comparison of reality and model provides the following equations:

For the experiment:

$$\dot{q}_R = \left(\frac{1}{\sum_{i=1}^{n} \frac{s_{R,i}}{\lambda_{R,i}}} + \varepsilon\sigma \cdot \left[T_{R,in}^2 + T_{R,out}^2 \right] \left[T_{R,in} + T_{R,out} \right] \right) \cdot \left(T_{R,in} - T_{R,out} \right) \tag{1}$$

and for the model:

$$\dot{q}_M = \left(\frac{\lambda_{eff}}{s_M} \right) \cdot \left(T_{M,in} - T_{M,out} \right) = \dot{q}_{M,i} = \left(\frac{\lambda_{M,i}}{s_{M,i}} + \frac{\lambda_{cor,i}}{s_{M,i}} \right) \cdot \left(T_{M,i} - T_{M,i+1} \right) \tag{2}$$

Because of equal heat flux of reality and model one gets from equation (1) and (2) the following equation for $\lambda_{cor,i}$:

$$\lambda_{cor,i} = \left(\frac{1}{\sum_{i=1}^{n} \frac{s_{R,i}}{\lambda_{R,i}}} + \varepsilon\sigma \cdot \left[T_{R,in}^2 + T_{R,out}^2 \right] \left[T_{R,in} + T_{R,out} \right] \right) \cdot \frac{T_{R,in} - T_{R,out}}{T_{M,i} - T_{M,i+1}} \cdot s_{M,i} - \lambda_{M,i} \tag{3}$$

Because of the assumption of a linear temperature profile across the gap, the summation factor in equation (3) can be simplified to:

$$\sum_{i=1}^{n} \frac{s_{R,i}}{\lambda_{R,i}} = \frac{s_R}{\lambda_{R,i}} \tag{4}$$

The thermal conductivity of model $\lambda_{M,i}$ and reality $\lambda_{R,i}$ are equal to each other because they simulate only the pure thermal conductivity λ_i excluding thermal expansion effects or radiation heat transfer.

Also, the linear temperature profile and the same temperatures assumed at the gap boundaries ($T_{R,in} = T_{M,in}$ and $T_{R,out} = T_{M,out}$) results in an equal temperature gradient, whereby from equation (3) under consideration of equation (4) follows:

$$\lambda_{cor,i} = \lambda_i \left(\frac{s_M}{s_R} - 1 \right) + s_M \cdot \varepsilon\sigma \cdot \left[T_{M,in}^2 + T_{M,out}^2 \right] \left[T_{M,in} + T_{M,out} \right] \tag{5}$$

The gap width of the experiment s_R has to be calculated in SCDAP/RELAP5 by using a thermal expansion coefficient β and the bulk radii referred to the averaged bulk temperature of the material next to the gap, whereas the radiation is based on the surface temperatures of the gap:

$$s_R = s_M + r_{mat,out} \cdot \beta_{mat,out} \cdot \left(T_{mat,out} - T_{mat,cold} \right) - r_{mat,in} \cdot \beta_{mat,in} \cdot \left(T_{mat,in} - T_{mat,cold} \right) \tag{6}$$

With help of this correction one gets the new thermal conductivity coefficient $\lambda_{eff,i}$ for each node of the modeled gap. They are equal to each other and to the conductivity λ_{eff} of the whole gap due to the assumption of a linear temperature profile:

$$\lambda_{eff} = \lambda_{eff,i} = \lambda_i\left(\frac{s_M}{s_R}\right) + s_M \cdot \varepsilon\sigma \cdot \left[T_{M,in}^2 + T_{M,out}^2\right]\left[T_{M,in} + T_{M,out}\right] \qquad (7)$$

The relation of the real gap thickness to the initial gap thickness represents the correction factor due to gap closure and the second term is the transformed radiation heat transfer coefficient.

Due to the added radiation term the conductivity increases by nearly 10 % at gap temperatures of about 1000 K in comparison to the old value. In the case of gap closure the thermal conductivity will reach values of metallic substances.

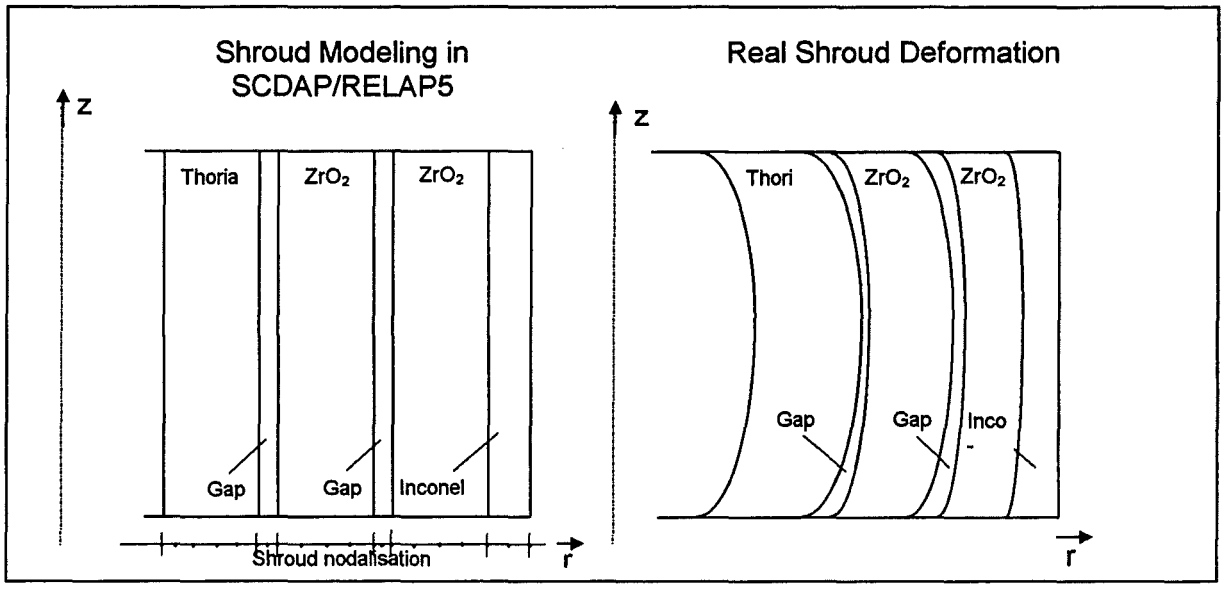

Figure 7.1 Modeling of a shroud consisting of two gaps and nodalization points used in SCDAP/RELAP5

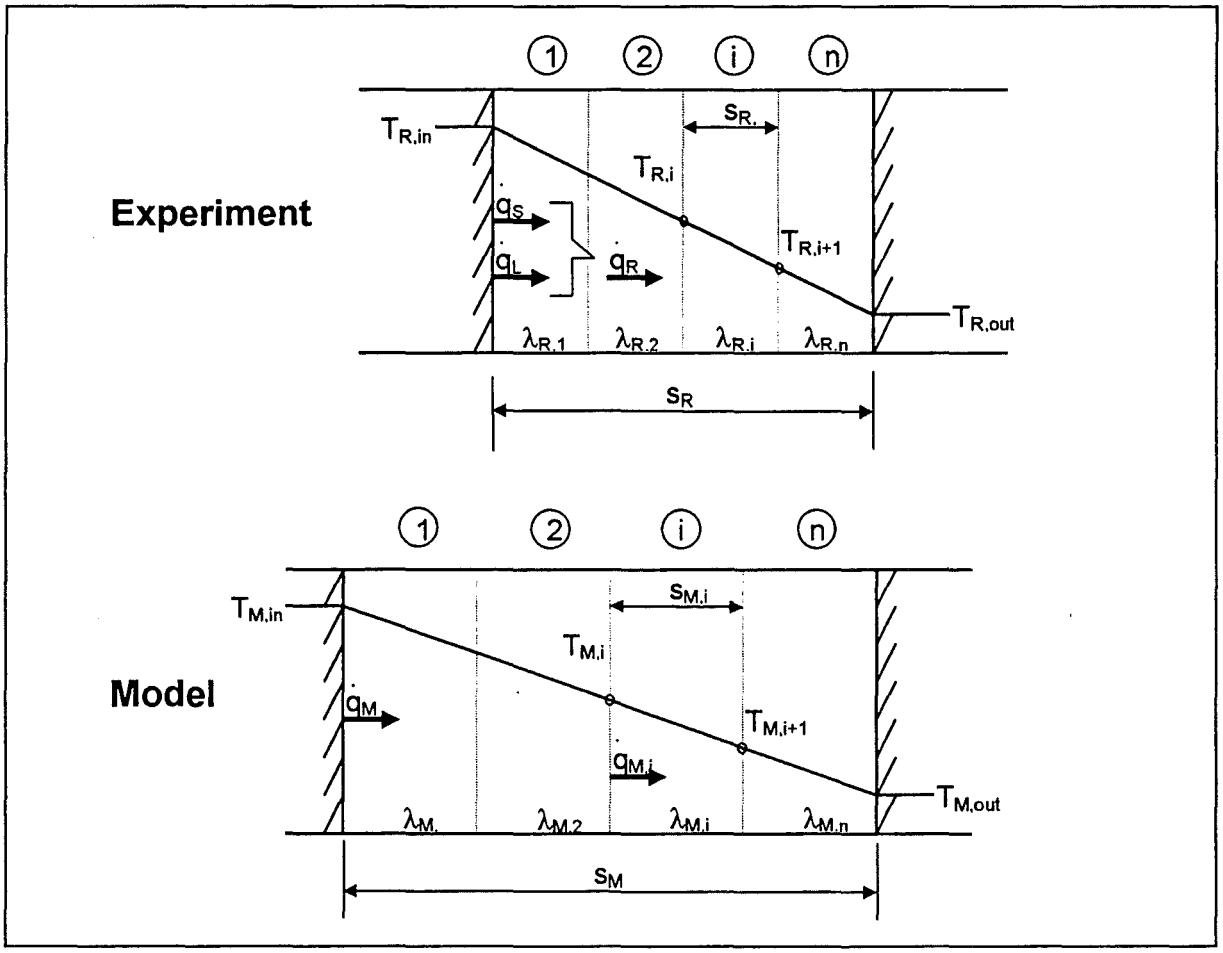

Figure 7.2 Comparison of reality and model of a shroud gap

7.2.2 Symbols

$\dot{q}_R$ heat flux across the whole gap of the experiment [W/m^2]

$\dot{q}_M$ heat flux across the whole gap of the model [W/m^2]

$\dot{q}_{M,i}$ heat flux across a node of the gap [W/m^2]

$\dot{q}_L$ heat flux due to heat conduction [W/m^2]

$\dot{q}_S$ heat flux due to heat radiation [W/m^2]

$r_{mat,in}$ averaged radius of the next inner material of the gap in the model [m]

$r_{mat,out}$ averaged radius of the next outer material of the gap in the model [m]

s_M whole gap width in the model [m]

$s_{M,i}$ node distance in the gap in the model [m]

s_R gap width in the experiment [m]

$s_{R,i}$ node distance, corrected with the experimental gap width [m]

$T_{R,in}$ temperature of inner side of shroud of the experiment [K]

$T_{M,in}$ temperature of inner side of shroud of the model [K]

$T_{R,out}$ temperature of outer side of shroud of the experiment [K]

$T_{M,out}$ temperature of outer side of shroud of the model [K]

$T_{M,i}$ temperature of inner side of node i of the model [K]

$T_{M,i+1}$ temperature of outer side of node i of the model [K]

$T_{mat,in}$ averaged bulk temperature of the next inner gap material of the model [K]

$T_{mat,out}$ averaged bulk temperature of the next outer gap material of the model [K]

$T_{mat,cold}$ temperature of cold material (usually 300K)

λ_i pur thermal conductivity of a node of the gap [W/mK]

$\lambda_{R,i}$ pur thermal conductivity of a node of the gap in the experiment [W/mK]

$\lambda_{M,i}$ pur thermal conductivity of a node of the gap in the model[W/mK]

λ_{eff} effective thermal conductivity of the whole gap in the model [W/mK]

$\lambda_{eff,i}$ effective thermal conductivity of a node of the gap in the model [W/mK]

λ_{cor} thermal conductivity correction factor due to radiation and gap deformation [W/mK]

$\lambda_{cor,i}$ thermal conductivity correction factor of a node [W/mK]

$\beta_{mat,in}$ thermal expansion coefficient of the next inner gap material [1/K]

$\beta_{mat,out}$ thermal expansion coefficient of the next outer gap material [1/K]

σ Stefan-Boltzmann constant ($5.67\ 10^{-8}$ W/(m^2K^2))

ε emissivity of shroud material [-]